

Data processing, 3D grain boundary modelling and analysis of *in-situ* deformation experiments using an automated fabric analyser microscope

Dissertation zur Erlangung des akademischen Grades „Doktor der Naturwissenschaften“ im Promotionsfach Geowissenschaften

am Fachbereich Chemie, Pharmazie und Geowissenschaften der
Johannes Gutenberg-Universität Mainz

Daniel Markus Hammes
geb. in Koblenz

Mainz, September 2017

Erklärung

Hiermit versichere ich, die vorgelegte Arbeit selbstständig und unter Verwendung der angegebenen Quellen und Hilfsmittel verfasst zu haben.

Mainz, September 2017

Datum der Prüfung: 12.12.2017

Abstract

The microstructure and fabric of a material influence critically the mechanical properties, such as the tensile strength and ductility. This holds for metals and ceramics, as well as for rocks and ice. Furthermore, microstructure and fabric provide vital information about the deformation and annealing history of polycrystalline solids.

Rock and ice thin sections can be scanned in high resolution and the orientation of the crystallographic c -axis determined using an automatic fabric analyser microscope (“Fabric Analyser”). The FAME (*Fabric Analyser based Microstructure Evaluation*) software, based on the original FAME scripts by Peternell et al. (2014), was developed in MATLAB® to analyse the data recorded data. In addition to an improved grain labelling, FAME incorporates a new “testing” gadget to simplify the determination of appropriate grain labelling parameters. FAME introduced a couple of new statistic and plotting tools, including c -axis misorientation maps and a toolbox to export FAME data to the elle (modelling software)-supported file format.

The data processed by FAME also provided the basis for FAGO (*Fabric Analyser Grain boundary recOnstruction*), a new and innovative approach for reconstructing grain boundaries in 3D from geological thin sections. Grain boundaries are an important aspect of the microstructure and play a significant role during recrystallization. However, there used to be a lack of non-destructive and easy-to-use computer supported methods to determine grain boundary geometries in 3D. The newly developed method basically uses the highest birefringence colour (retardation) at each pixel in the field of view acquired by the 9 different oriented light sources of the Fabric Analyser. Retardation profiles across grain boundaries enable the calculation of grain boundary angle and direction. In combination with the lateral position of the grain boundary, acquired using FAME, the data is used to reconstruct a 3D grain boundary model. The data processing is almost fully automatic by using MATLAB®.

An important application of FAME is the analysis of *in-situ* pure shear ice deformation experiments which allow a continuous observation of the microstructure during the progress of deformation using the Fabric Analyser. The experimental modelling of ice provide vital information about the rheological behavior of ice which is necessary to understand the movement of glacier. Three ice samples from the Sørødal Glacier were deformed

at -10°C ; two at relative fast strain rate ($2 \cdot 10^{-6}$ 1/s) and one at relative slow rate ($1 \cdot 10^{-6}$ 1/s) by M. Peternell and C.J.L. Wilson. It was revealed that no steady state was reached in the slow strain experiment, even at 57.6% strain. The concentration of dislocations on large grains in hard glide position seems to lead to cyclic changes in the population of grains in easy glide position and impedes the approach to the steady state in this experiment. In contrast to the well-established literature a stabilised mean grain size proved not to be a reliable indicator for the steady state. Instead two new microstructure-based indicators for the steady state were introduced, the “seeding rate” and the “microstructure activity”.

Zusammenfassung

Die Mikrostruktur eines Materials beeinflusst die mechanischen Eigenschaften substantiell, wie z.B. die Zerreifestigkeit und die Dehnbarkeit. Dies gilt sowohl fr Metalle und keramische Werkstoffe, als auch fr Gestein und Eis. Die Mikrostruktur liefert auch entscheidende Informationen ber vorangegangene Materialbeeinflussung wie Deformationen und Tempern von polykristallinen Feststoffen.

Gesteins- und Eisdnnschliffe knnen mit einem automatischen Gefgemikroskop („Fabric Analyser“) mit hoher Auflsung gescannt und die Orientierung der kristallographischen *c*-Achse bestimmt werden. Fr die Analyse der aufgenommenen Daten wurde die „FAME“ (*Fabric Analyser based Microstructure Evaluation*) Software, basierend auf den Vorarbeiten von Peternell et al. (2014), entwickelt. Zustzlich zu einer verbesserten Kornsegmentierung bietet FAME z.B. auch eine „Testing“-Funktion die die Bestimmung der passenden Analyseparameter vereinfacht. FAME fhrt zustzlich auch eine Anzahl neuer Statistiken und graphischer Darstellungen ein, wie z.B. „*c*-axis misorientation maps“ und die Mglichkeit vom Export ins Dateiformat der Modellierplattform „elle“.

Die von FAME generierten Daten sind auch die Grundlage von FAGO (*Fabric Analyser Grain boundary recOnstruction*), einer neuen und innovativen Methode fr die Rekonstruktion von Korngrenzen in 3D. Korngrenzen sind ein wichtiger Aspekt der Mikrostruktur und sie spielen eine entscheidende Rolle bei der Rekristallisation. Es mangelt jedoch an zerstrungsfreien und einfach zu benutzenden computerbasierten Methoden fr die Bestimmung der Kornstruktur in 3D. Die neuentwickelte Methode verwendet die hchste Farbe der Doppelbrechung („retardation“, Gangunterschied) in jedem betrachteten Pixel und aus den 9 verschiedenen angeordneten Lichttrichtquellen des Fabric Analysers. Profile der retardation quer ber die Korngrenze dienen zur Bestimmung des Einfallswinkels und der Einfallsrichtung der Korngrenze. Zusammen mit der von FAME bestimmten lateralen Position der Korngrenze lsst sich ein 3D Modell erstellen. Durch die Implementierung in MATLAB® ist FAGO fast vollautomatisch.

Eine weitere wichtige Anwendung von FAME ist die Analyse von *in-situ* Eisdeformationsexperimenten welche die kontinuierliche Betrachtung der Entwicklung der Mikrostruktur mit Hilfe des Fabric Analysers whrend der Deformationen erlauben. Das experimentelle Modellieren von Eis liefert wichtige Informationen fr das Verstndnis der

rheologischen Eigenschaften welche notwendig sind um das Fließverhalten und Gletschern besser verstehen zu können. Drei Eisproben vom Sørtdal-Gletscher wurden von M. Peternell und C.J.L. Wilson bei -10°C deformiert, zwei mit relativ hoher ($2 \cdot 10^{-6} \text{ 1/s}$) und eines mit vergleichsweise niedriger Verformungsrate ($1 \cdot 10^{-6} \text{ 1/s}$). Sogar bei einer Verformung von 57,6% wurde bei letzterem Experiment kein Gleichgewichtszustand („steady state“) erreicht. Die Konzentration von Fehlstellen im Kristall wird konzentriert in großen Körnern, welche in Bezug auf die basale Gleitfläche ungünstig orientiert sind. Dies führt zu einer periodischen Änderung der Population der Körner in günstiger Orientierung, welche die Einstellung eines Gleichgewichtszustands verhindert. Die stabilisierte mittlere Korngröße zeigte sich als nicht zuverlässiger Indikator für ein Erreichen des Gleichgewichtszustands, im Gegensatz zu vorangegangenen Studien. Stattdessen wurden zwei neue, auf der Mikrostruktur basierende, Indikatoren eingeführt, die „Nukleationsrate“ und die „Mikrostrukturaktivität“.

Table of Contents

Abstract	2
Zusammenfassung	4
Table of Contents.....	6
1. Introduction	8
1.1 Aims of this study and motivation	14
1.2 Methods and instrumentation	16
1.3 Structure of thesis.....	18
1.4 Contributions.....	19
References	19
2. FAME: Software for analysing rock microstructures	26
Abstract	26
2.1 Introduction.....	26
2.2 FAME Software	28
2.2.1 Data processing (overview)	28
2.2.2 Data preview and cropping tools	30
2.2.3 Testing.....	31
2.2.4 Step growth	35
2.2.5 Crystallographic orientation (texture) analysis.....	38
2.2.6 Application of FAME to the elle modelling software	39
2.3. Conclusion	41
References	42
3. Reconstruction of 3D grain boundaries from rock thin sections, using an advanced polarised-light microscopy method	45
Abstract	45
3.1 Introduction.....	46
3.2. Grain boundary principles.....	47
3.3. Instrumentation	48
3.3.1 Fabric Analyser Instrument.....	48
3.3.2 Polarising microscope and universal stage	49
3.4. FAGO grain boundary analysis.....	51
3.4.1. Retardation.....	51
3.4.2. Fabric Analyser retardation profiles	52
3.4.3. Defining the width of the transition region.....	53
3.4.4. Transition region width and grain boundary orientation	55
3.4.5. FAGO grain boundary segmentation	56
3.5. Verification of grain boundary segment orientation	59
3.6. 3D grain boundary reconstruction.....	62

3.7. Application on other materials	64
3.8. Discussion	65
3.9. Conclusion	66
References	66
4. A new insight into the steady state in constant strain rate pure shear experiments	70
Abstract	70
4.1 Introduction	71
4.2 Methods	73
4.3 Results	75
4.3.1. Slow deformation (Ex1)	76
4.3.2. Fast deformation (Ex2 and Ex3)	76
4.4. Discussion	78
4.5. Conclusions	80
Supplementary Material	80
Supplementary A: Smoothing of data	80
Supplementary B: “Softness of grains and influence of glass plates	83
References	87
5. Final conclusions and future work	90
5.1 FAME Software	90
5.2 FAGO grain boundary reconstruction	91
5.3 <i>In-situ</i> ice deformations	92
5.4 Suggestions for future work	93
References	95
Acknowledgements	97
Curriculum Vitae	98

1. Introduction

A comprehension of microstructure, the spatial arrangement of atoms, is essential to better understand the properties of polycrystalline solids such as metals, ceramics, rocks and ice (Mittermijer, 2010, preface). In particular, by considering the microstructure and fabric of rocks its structural and metamorphic history can be revealed and the underlying processes interpreted (Passchier and Trouw, 2005, p. 1).

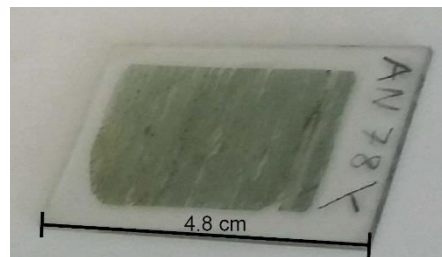


Figure 1.1. Photograph of a geological rock thin section, as commonly used in the analysis of microstructures.

Practical crystallographic observations on the microscale were made possible for the first time by the invention of the polarising microscope by G.B. Amici (Dippel, 1866; p. 213f), which are commonly done on rock samples in thin section (Fig. 1.1) The universal stage (u-stage; Fedorow, 1891) enables the rotation of a sample under a microscope and therefore the determination of the orientation of the crystallographic c -axis of birefringent materials using polarised light.

Based on u-stage measurements B. Sander published his ground breaking work (Sander, 1948) on “Gefügekunde” (structural analysis; Turner and Weiss, 1963). With the development of X-ray diffraction (Bragg and Bragg, 1913; Laue and Tank, 1913) the atomic structure of crystals, e.g. ice (Pauling, 1935), could be determined for the first time. The invention of the transmission electron microscope (TEM) by E. Ruska (Knoll and Ruska, 1932) enabled the direct observations of materials on the nm-scale, but the application on rocks was overshadowed by the scanning electron microscope (SEM; von Ardenne, 1938). In combination with an EBSD detector (electron backscatter diffraction; Venables and Harland, 1973; Dingley and Randle, 1992; Adams et al., 1993; Humphreys, 2001) the full crystallography of crystalline materials, such as geological minerals can be

measured (Prior et al., 1999, 2015). Despite the advances in electron optics the development of new instruments using visible light for resolving the crystallography was not in stagnation. The classical universal stage is still used for some specialised tasks, but is nowadays overshadowed by devices enabling the automatic measurement of crystallographic preferred orientations from rock and ice thin sections (e.g. Panozzo Heilbronner and Pauli, 1993; Fueten, 1997; Wilen, 2000; Hansen and Wilen, 2002; Wilson et al., 2003 and 2007). The Fabric Analyser (Fig. 1.2; Russel-Head and Wilson, 2001; Wilson et al., 2003, 2007) enables the determination of the *c*-axis orientation of uniaxial minerals (sample data shown in figure 1.3). For collecting grain-based microstructural information such as the grain size, the determination of the outline of the grains from a non-connected pixel-based data set, such as the data recorded by the Fabric Analyser, is essential. Different approaches are possible to accomplish this task (e.g. Goodchild and Fueten, 1998, Heilbronner, 2001; Barraud, 2006; Fueten and Masion, 2007; Hassanpour, 2011). One established method for grain labelling is the decomposition into Voronoi cells, as used in the MTEX toolbox (Bachmann et al., 2011).



Figure 1.2. Photograph of Fabric Analyser G60.

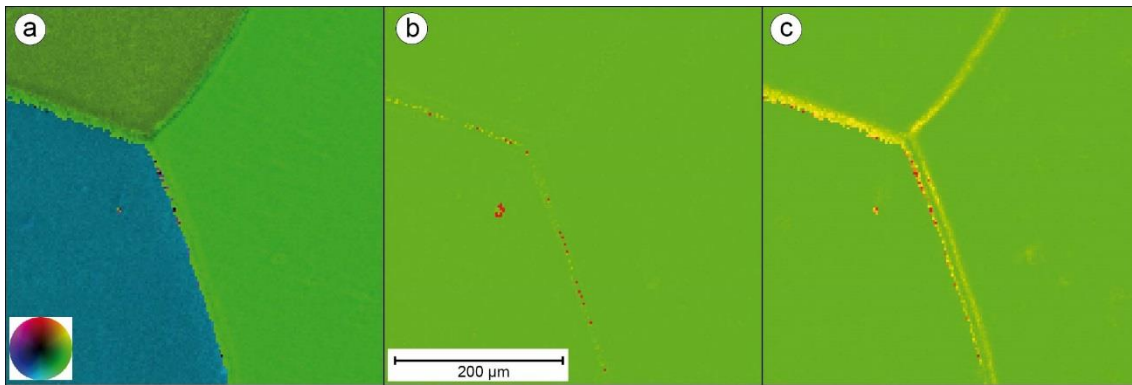


Figure 1.3. Cut from data acquired using the Fabric Analyser G50 from a quartzite sample. a) *c*-axis orientation image. b) Retardation quality map. c) Geometric quality map. This small data set was used during the development of the FAME software. Colour wheel indicates *c*-axis orientation.

3D Grain boundary reconstruction

One important facet of microstructure is the boundaries between grains. These are planar defects in the lattice that separate regions of different crystallographic orientation. (Vernon 1976, p. 163f, Humphreys and Hatherly 2004, p. 91f). Based on the higher misorientation angle of $\sim 10^\circ$ - 20° in the crystallographic orientation, high-angle grain boundaries may be distinguished from low-angle grain boundaries (McLaren, 1986; Humphreys and Hatherly, 2004). A low-angle grain boundary is considered a defect in a single crystal rather than an interface between separate grains (Poirier, 1989; p. 63). Due to the difference in misorientation angle, grains connected by high angle grain boundaries are more easily detected in an automatic grain labelling process than grains separated by a low-angle grain boundary.

Grain boundaries in general are favoured sites for the nucleation of new grains and therefore play an essential role in recrystallization (Doherty et al., 1997). Thus, they are an important factor for microstructural evolution during high temperature deformations. In general, they affect the physical and chemical properties significantly by initiating reactions and collecting impurities and are therefore a critical factor in material failure (Birchenall, 1959, p. 40). Grain boundaries also affect the movement of dislocations in crystals (Swygenhoven, 2002). The vital importance of grain boundaries holds for all crystalline solids, including ceramics (Kingery, 1984) and rocks (White, 1981). In particular, the shape and crystallographic orientation of grain boundaries indicate the deformation and annealing history of rocks and can also be applied as a geothermometer (Kruhl and Peternell 2002, Kruhl 2001).

Grain boundaries have been mostly researched in metals, and to a lesser extent in ceramics (Clarke 1987; Wolf and Yip 1992; Sutton and Ballu 2006). Pioneering work on grain boundaries in deformed quartz was undertaken by S.H. and J.C. White (White 1977, White and White 1981). Further studies by Jessel (1987). Voll (1960), Kruhl and Peternell (2002), Kuntcheva et al. (2006) and Liebl et al. (2007) have investigated the role of high-angle grain boundaries on the recrystallization of quartz.

White and White (1981) used transmission electron microscopy for their research on grain boundaries. Techniques such as regular transmission or scanning electron microscopy are restricted on 2D planes cut through the sample (Zaefferer et al., 2008). Therefore the polarising microscope with attached universal stage is still used for investigating the geometry of grain boundaries, e.g. by Kruhl and Peternell (2002). By rotating the thin section sample under the view of the microscope the measurement of the grain boundary dip is possible.

In the last decades several new instruments have been developed to investigate the 3D microstructure of crystals and grain boundaries, mostly with emphasis on metals. Possibly due to the focus on metals, none of these methods use optical light. One of the most common is 3D EBSD (electron back-scatter diffraction; Rowenhorst et al. 2006, Rollet et al. 2007). To acquire the data needed to reconstruct the 3D structure, the sample is analysed section-by-section, using a focused ion beam (FIB) together with an EBSD unit. A high resolution is possible ($\sim 100 \times 100 \times 100 \text{ nm}^3$), but the sample is destroyed during the process (Zaefferer et al. 2008). Mandal et al. (2014) developed a non-destructive 3D method, combining two sets of 2D EBSD measurements on specially prepared specimen to acquire the crystallographic properties of grain boundaries. In contrast to the electron beam-based EBSD, a synchrotron X-ray microbeam (DAXM: differential-aperture X-ray microscopy) can be applied to analyse the crystal structure to get the grain-boundary normal direction (Larson et al. 2002, Wenge Yang et al. 2004). Furthermore, x-ray diffraction contrast tomography can also be used to resolve the 3D grain structure (Rolland du Roscoat et al., 2011). A digital segmentation algorithm applied on x-ray tomography can be used for reconstructing the 3D structure of snow grains (Hagemuller et al. 2013; Xi Wang et al. 2013).

Ice deformations

Snow and ice are of significant importance for our climate and the prediction of sea-level changes. For instance, the complete melting of the ice stored within Greenland and the Antarctic ice sheets would raise the sea-level by $\sim 7\text{m}$ and $\sim 60\text{m}$, respectively (Schulsen and Duval 2009, p. 1). For a deeper understanding of the influence of ice on the climate fundamental knowledge of ice dynamics and rheology is essential (Montagnat et al., 2011) and information about the rheology can be gathered by studying the ice microstructure during deformation experiments. Furthermore, ice can also be used as a rock analogue (Wilson 1981, 1983). The first researchers to investigate the rheological properties of ice were Reusch (1864), Pfaff (1875) and Koch (1885). Further progress was made by Main (1887) and McConnell and Kidd (1888). Significantly later, further pioneering work in the experimental modelling of ice creep by laboratory studies was done by Glen (Glen and Perutz 1954, Glen 1955) and Steinemann (1958). Glen (1955) was also the first to state an empirical relationship between applied stress and resulting strain rate in ice deformations, which is now widely known as ‘‘Glen’s flow law’’: $\dot{\epsilon} = B\sigma^n$ (Wilson et al, 2014). $\dot{\epsilon}$ denotes the strain rate, σ the stress and B and n are empirical constants. The same relationship, with different empirical parameters, also holds for other crystalline materials, such as metals (Glen 1955; Mittermijer 2010, p. 566).

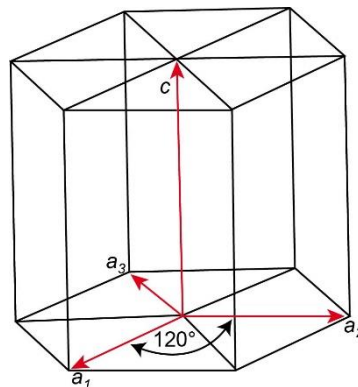


Figure 1.4. Sketch showing the hexagonal lattice of ice. The c -axis is perpendicular to the three a -axis and the basal plane (after Schulsen and Duval, 2009, p. 25).

Isotropic ice deformed under constant applied stress passes through different stages of creep (Fig. 1.4, Budd and Jacka, 1989), as also observed in other polycrystalline materials (e.g. Roesler et al. 2007, Section 11.1). After an initial elastic regime, primary creep, associated with a decreasing strain rate and mostly inelastic, occurs until around

1% strain. This is followed by secondary creep and a regime of accelerating strain rate. Beyond 10% shortening a steady state tertiary flow with constant strain rate may develop, if no cracking occurs. During this equilibrium deformation and rotation are balanced by crystal growth and change (Budd and Jacka 1989, Schulsen and Duval 2009, p. 103). The steady state is therefore in general associated with an equilibrium grain size irrespective of the initial grain size (Jacka 1984b, Budd and Jacka 1989, Jacka and Li Jun 1994). Other microstructural parameters are not established as steady state indicators.

On the atomic scale creep can be explained by the movement of dislocations (e.g. Weertman 1955, Schulsen and Duval 2009, p. 5f). Dislocations are highly mobile on the basal planes (Fig. 1.5) in ice which leads to an easy slip along this plane (Schulsen and Duval 2009, p. 10, Weertman 1983). Slip along non-basal planes is of significantly less importance (Gilra 1974, Duval et al. 1983). The deformation of a particular grain therefore depends on the resolved basal shear stress and thus on the orientation of the c -axis relative to the main stress axes (Schmid and Boas 1935, p. 111, Azuma 1995, Wilson et al. 2014). Depending on this orientation we differentiate between “easy” and “hard” glide positions and “soft” and “hard” grains, respectively (Wilson and Peterzell 2012, Piazzolo et al. 2013). This fact further motivates the investigation of the microstructure and fabric during deformation experiments.

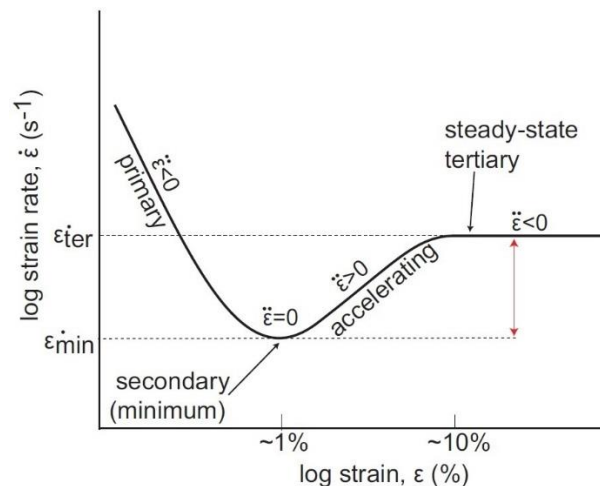


Figure 1.5. Idealised creep curve of ice shows the various stages of strain vs. strain rate. Modified after Wilson et al. (2014) and Budd and Jacka (1989).

1.1 Aims of this study and motivation

The visual investigation of the microstructure using a simple polarising microscope with an attached universal stage is time consuming and difficult to accomplish for continuous deformation experiments. The Fabric Analyser simplifies this process enormously and enables a continuous observation of the c -axis orientation, in addition to routine observations of microstructural evolution under crossed polarisers. For the efficient analysis of Fabric Analyser based data Peternell et al. (2014) developed a set of MATLAB® scripts. These original FAME (*Fabric Analyser based Microstructure Evaluation*) scripts offered a set of plotting tools, such as grain size statistics, shape preferred orientation (SPO) and crystallographic preferred orientation (CPO) plots. As the toolbox was script-based, it was not particularly convenient for users with no experience in MATLAB® or other programming languages. Furthermore, the FAME scripts couldn't be run without the proprietary commercial MATLAB® environment. A GUI-based MATLAB® software on the contrary can be compiled with the freeware MATLAB® Compiler runtime (MCR) and run on operation systems without requiring a valid MATLAB® licence. A development of a GUI-based (graphical user interface) software was therefore obvious.

However, the main motivation for the further development of FAME was the fact that the analysis of Fabric Analyser data with regard to the fabric and microstructure of rock and ice sections required further tools which were not part of the original FAME scripts. For example, grain-based orientation density plots using the method of Fisher et al. (1987) and fabric ternary diagrams (Benn, 1994) were regarded as necessary. Several further improvements were required: (i) a more developed grain labelling algorithm; (ii) a more efficient environment for defining the grain labelling parameter; (iii) an adequate way of grain labelling to define the position of the grain boundaries in the thin section plane as a foundation for the 3D grain boundary reconstruction (see below); (iv) a simpler data structure for the labelled grain maps was therefore desirable. Based on these requirements, the need to develop comprehensive GUI-based software for processing Fabric Analyser data arose.

Another important topic of this thesis was the development of a Fabric Analyser-based method for analysing grain boundaries in 3D, as stated in the title of the project founded by the research cluster "Rechnergestützte Forschungsmethoden in den Naturwissenschaften"

ten” (SRFN) of the University of Mainz and granted to M. Peternell (Principal Investigator; Institute of Geosciences), E. Schömer (Institute of Computer Science) and R. Schulze (University Medical Center): “3D rock-microstructure modelling by the use of an automated Fabric Analyser”. (<https://www.csm.uni-mainz.de/3d-modellierung-von-gesteins-mikrostrukturen-mit-hilfe-eines-automatischen-gefuegemikroskops/>).

Considering the importance of grain boundaries, no automatized computer-based light-optical method exists which enables the analysis of the grain boundary geometry in 3D from thin sections. The only available instrument is the classical u-stage, which is operated manually and therefore time consuming and tedious to use.

The aim was to develop a method which analyses the dip of grain boundaries and enables reconstruction of 3D models of complete grain boundaries. The data was to be acquired with a Fabric Analyser and further processes by an external computer, e.g. with the help of C++ or MATLAB®. Manual input by the user was intended to be as small as possible.

The method measures the thickness of the transition region between the grains in the retardation data and uses this value to calculate the dip of the grain boundary. A specific algorithm needed to be developed and tested which determines this thickness without any user input. The acquisition of the necessary retardation data from different light angles required a development of a modified instrument software for the Fabric Analyser in cooperation with the manufacturer D. Russel-Head. Afterwards, the grain boundary dip data acquired through the Fabric Analyser needed to be verified by measurements with the universal stage. With the help of FAME the location of the grain boundary in the observation planes could be determined and the dip between grains measured. An extensive set of algorithms needed to be developed to reconstruct grain boundary segments out of this incoherent data set. The result could be finally used for the reconstruction of complete grain boundaries.

A second application of FAME is the analysis of *in-situ* (e.g. Means 1980, Urai et al. 1980, Jessell 1986, Peternell et al. 2011) constant strain ice deformation experiments. In many studies (e.g. Mellor and Cole 1982, Jacka 1984a, Hamann et al. 2007) the ice samples are only shortened until a strain of ~10%. Notably exceptions are for example Wilson and Russel-Head (1982), Li Jun et al. (1996) and Wilson et al. (2014). Almost all of these experiments, excluding Wilson et al. (2014), analyse only the microstructure before or

after the deformation or solely record the stress-strain relationship. No profound information about the evolution of the microstructure is obtained. There is therefore a significant lack in understanding of the development of microstructure and fabric at high strain values and during steady state. By using the Fabric Analyser and a coupled deformation press (Paternell et al., 2011) *in-situ* observations are possible.

An extensive set of *in-situ* deformation experiments were conducted by M. Paternell and C.J.L. Wilson in the years 2010 to 2013. This data needed to be analysed and evaluated. Once again, FAME proved to be indispensable for the task. Altogether, 29 different experiments with more than 24,000 individual frames were considered. The primary aim of this study was to better understand the evolution of the microstructure in the high strain regime (>20% strain) and to determine the onset of the steady state. The equilibrium mean grain size and other microstructural variables, such as the nucleation rate, were investigated for its use as steady state indicators.

1.2 Methods and instrumentation

The main instrument applied for this research is the Fabric Analyser, an automated polarising optical microscope that determines the orientation of *c*-axes of uniaxial materials at each pixel in the field of view (Paternell et al. 2009, 2010, 2011, 2014; Wilson et al., 2003, 2007). The spatial resolution is up to 2.8 μm /pixel in the Melbourne-based instrument, all other used instruments up to 5 μm /pixel. Complete thin sections can be automatically scanned in ~30-90 minutes at a resolution of 5 μm /pixel. Different Fabric Analyser instruments were used, which differ in some details. The G50 in Melbourne was used together with a deformation press (details in Paternell et al. 2011) for recording the *in-situ* ice deformations by M. Paternell and C.J.L. Wilson (Chapter 4). Data acquired by this device was also used for testing the FAME software (Chapter 2) during its development. A second G50 facility, located in the Alfred Wegener Institute for Polar and Marine Research in Bremerhaven, was used for collecting the data for the grain boundary modelling (Chapter 3). A G60 prototype, and a second facility with improved accuracy, both located in Mainz, were also used.



Figure 1.6. Photograph of a Leitz polarising microscope with attached universal stage.

For determining the grain boundary geometry a Leitz polarising microscope with 5-times magnification objective and an attached Leitz UT4 universal stage was used (Fig. 1.6). A versatile and dimmable LED light source was developed and custom-built by the author for illuminating the field of view. For observing thin section samples and taking microphotographs with an attached CMOS camera a Leitz DMRP polarising microscope (Fig. 1.7) was used.



Figure 1.7. Photograph of a Leitz DMRP polarising microscope.

The MATLAB® environment was used for processing data and developing the FAME software (Chapter 2). The open source toolboxes MTEX (Bachmann et al., 2011) and PolyLX (Lexa, 2003; Lexa et al, 2005) were applied in some cases. Next to MATLAB®, some minor code was developed in C++, for example for processing and modifying Fabric Analyser raw data efficiently.

1.3 Structure of thesis

This thesis is divided into five chapters. Chapter 1 provides a comprehensive introduction and discusses the aims of this study. It further deals with the applied instruments and methods. Chapters 2, 3 and 4 are the main part of the thesis. Each of these chapters are independent and self-contained, and therefore contain an introduction, conclusions and references.

Chapter 2 deals with the FAME (*Fabric Analyser based Microstructure Evaluation*) software for analysing Fabric Analyser-based microstructural data. This chapter contains an overview of the work flow and organisation of FAME and discusses newly introduced algorithms, tools and plots. It was published in *Computers & Geosciences* (Hammes and Peternell, 2016). Further information about FAME and its use are to be found in the FAME manual.

Chapter 3 considers FAGO (Fabric Analyser Grain boundary reconstruction), a new method for reconstructing the 3D structure of grain boundaries in minerals using data acquired with the Fabric Analyser. The material was published in *Journal of Microscopy* with small editorial changes (Hammes and Peternell, *in press*).

Chapter 4 analyses the steady state in uniaxial *in-situ* ice deformation experiments, recorded by the Fabric Analyser. This contribution was submitted to *Earth & Planetary Science Letters* (EPSL).

In contrast to the published or submitted contributions, small editorial changes were necessary in chapters 2 to 4. This includes a change to British English, a modified figure enumeration and a consistent reference formatting.

Final conclusions and suggestions for future work are discussed in Chapter 5.

1.4 Contributions

The presented work was done by the author under the fruitful supervision of M. Peterneil, C.J.L. Wilson and C.W. Passchier.

The progress of FAME since the publication of the original scripts by Peterneil et al. (2014), as considered in [Chapter 2](#), was developed by the author. This includes the development and implementation of algorithms, programming of the graphical user interface and the writing of the FAME manual. The Fabric Analyser data used for testing purposes and for the presented examples was mainly acquired by M. Peterneil.

The 3D grain boundary reconstruction considered in [Chapter 3](#), is originally based on an idea by M. Peterneil. The author has developed and implemented the necessary algorithms and conducted the u-stage and Fabric Analyser measurements.

The *in-situ* ice deformation experiments discussed in [Chapter 4](#) were run by M. Peterneil and C. J.L. Wilson in the years 2010 to 2013 in Melbourne, Australia. The data analysis, the determination of the analysis parameter and the evaluation of the data was done by the author using FAME and further software written by him.

References

- Adams, B.L., Wright, S.I., Kunze, K., 1993. Orientation imaging: the emergence of a new microscopy. *Metallurgical Transactions A* 24, 819-831.
- Ardenne, M. v., 1937. Das Elektronen-Rastermikroskop – Theoretische Grundlagen. *Zeitschrift für Physik* 109, 553-572.
- Azuma, N., 1995. A flow law for anisotropic polycrystalline ice under uniaxial compressive deformation. *Cold Regions Science and Technology* 23, 137-147.
- Bachmann, F., Hielscher, R., Schaeben, H., 2011. Grain detection from 2d and 3d EBSD data – Specification of the MTEX algorithm. *Ultramicroscopy* 111, 1720-1733.
- Barraud, J., 2000: The use of watershed segmentation and GIS software for textural analysis of thin sections. *Journal of Volcanology and Geothermal Research* 154, 17-33.
- Benn, D.I., 1994. Fabric shape and the interpretation of sedimentary fabric data. *Journal of Sedimentary Research* A64, 910-915.
- Birchenall, C.E., 1959. *Physical Metallurgy*. McGraw-Hill, New York, 323pp.

- Bragg, W.H., Bragg, W.L., 1913. The reflection of X-rays by crystals. *Proceedings of the royal society* 88, 428-438
- Budd, W.F. and Jacka, T.H., 1989. A review of ice rheology for ice sheet modelling: *Cold Regions Science and Technology* 16, 107-144.
- Clarke, D.R., 1987. Grain boundaries in polycrystalline ceramics. *Annual Review of Materials Research* 17, 57-74.
- Dingley, D.J, Randle, V., 1992. Microtexture determination by electron back-scatter diffraction. *Journal of Materials Science* 27, 4545-4566.
- Dippel, L., 1866. *Das Mikroskop und seine Anwendung – Band 1*. Friedrich Vieweg & Sohn, Braunschweig, pp. 490.
- Duval, P., Ashy, M.F., Anderman, I., 1983. Rate-controlling processes in the creep of polycrystalline ice. *Journal of Physical Chemistry* 87, 4066-4074.
- Fedorow, E. v., 1891. Eine neue Methode der optischen Untersuchung von Krystallplatten in parallelem Lichte. *Tschermak's Mineralogische und Petrographische Mitteilungen*, 12, 505-509.
- Doherty, R.D., Hughes, D.A., Humphreys, F.J., Jonas, J.J., Juul Jensen, D., Kassner, M.E., King, W.E., McNelley, T.R., McQueen, H.J., Rollett, A.D., 1997: Current issues in recrystallization: a review. *Materials Science and Engineering A* 238, 219-274.
- Fisher, N.I., Lewis, T., Embleton, B.J.J., 1987. *Statistical analysis of spherical data*. Cambridge University Press, Cambridge, pp. 329.
- Fueten, F., 1997. A computer-controlled rotating polarizer stage for the petrographic microscope. *Computer & Geoscience* 23, 203-208.
- Fueten, F., Mason, J., 2007. An artificial neural net assisted approach to editing edges in petrographic images collected with the rotating polarizer stage. *Computers & Geosciences* 32, 1176-1188.
- Gilra, N.K., 1974. Non-basal glide in ice. *Physica status solidi (a)* 21, 323-327.
- Glen, J.W., Perutz, M.F., 1954. The growth and deformation of ice crystals. *Journal of Glaciology* 2, 397-403.
- Glen, J.W., 1955. The creep of polycrystalline ice. *Proceedings of the Royal Society of London A* 228, 519-538.
- Goodchild, J.S., Fueten, F., 1998. Edge detection in petrographic images using the rotating polarizer stage. *Computers & Geosciences* 24, 745–751.
- Hagenmuler, P., Chambon, G., Flin, F., Xi Wang, Lesaffre, b., Naaim, M., 2013: Description of snow microstructures as a 3D assembly of grains. *International Snow Science Workshop (ISSW)*, Oct 2013, Grenoble – Charmonix Mont-Blanc, France, 67-91.

- Hamann, I., Weikusat, C., Azuma, N., Kipfstuhl, S., 2007. Evolution of ice crystal microstructure during creep experiments. *Journal of Glaciology* 53, 479-489.
- Hammes, D. M., Peterzell, M., 2016. FAME: Software for analysing rock microstructures, *Computers & Geosciences* 90A, 23-33.
- Hammes, D. M., Peterzell, M., *in press*. Reconstruction of 3D grain boundaries from rock thin sections, using an advanced polarised-light microscopy method. *Journal of microscopy*. Early view available online: <http://onlinelibrary.wiley.com/doi/10.1111/jmi.12605/full>
- Hansen, D.P., Wilen, L.A., 2002. Performance and applications of an automated c-axis ice-fabric analyser. *Journal of Glaciology* 48, 159-170.
- Hassanpour, A., 2012. The use of ArcGIS for determination of quartz optical axis orientation in thin section image. *Journal of Microscopy* 245, 276-287.
- Heilbronner, R., 2000. Automatic grain boundary detection and grain size analysis using polarization micrographs or orientation images. *Journal of Structural Geology* 22, 969-981.
- Humphreys, F.J., 2001. Grain and subgrain characterisation by electron backscatter diffraction. *Journal of Materials Science* 36, 3833-3854.
- Humphreys, F.J., Hatherly, M., 2004. *Recrystallization and related annealing Phenomena*. 2nd edition, Elsevier, Amsterdam, pp. 658.
- Jacka, T.H., 1984. The time and strain required for development of minimum strain rates in ice. *Cold Regions Science and Technology* 8, 261-268. (cited as Jacka 1984a)
- Jacka, T.H., 1984. Laboratory studies on relationships between ice crystal size and flow rate. *Cold Regions Science and Technology* 10,31-42. (cited as Jacka 1984b)
- Jacka, T.H., Li Jun, 1994. The steady state crystal size of deforming ice. *Annals of Glaciology* 20, 13-18.
- Jessel, M.W., 1986. Grain boundary migration and fabric development in experimentally deformed octachloropropane. *Journal of Structural Geology* 8, 527-542.
- Jessel, M.W., 1987. Grain-boundary migration microstructures in naturally deformed quartzite. *Journal of Structural Geology* 9, 1007-1014.
- Kingery, W.D., 1984. The chemistry of ceramic grain boundaries. *Pure and Applied Chemistry* 56, 1703-1714.
- Knoll, M., Ruska, E., 1932. Das Elektronenmikroskop. *Zeitschrift für Physik* 78, 318-339.
- Koch, K.R., 1885. Beiträge zur Kenntniss der Elasticität des Eises. *Annalen der Physik* 261, 438-450.

- Kruhl, J.H., 2001. Crystallographic control on the development of foam textures in quartz, plagioclase and analogue material. *International Journal of Earth Science* 90, 104-117.
- Kruhl, J.H., Peternell, M., 2002. The equilibration of high-angle grain boundaries in dynamically recrystallized quartz: the effect of crystallography and temperature. *Journal of Structural Geology* 24, 1125-1137.
- Kuntcheva, B., Kruhl, J.H., Kunze, K., 2006. Crystallographic orientation of high-angle grain boundaries in dynamically recrystallized quartz: First results. *Tectonophysics* 421, 331-346.
- Lexa, O., 2003. Numerical Approaches in Structural and Microstructural Analyses. Unpublished PhD Thesis. Charles University, Prague, pp. 137.
- Lexa, O., Stípská, P., Schulmann, K., Baratoux, L., Kröner, A., 2005. Contrasting textural record of two distinct metamorphic events of similar P-T conditions and different durations. *Journal of Metamorphic Geology* 23, 649-666.
- Larson, B.C., Wenge Yang, Ice, G.E., Budai, J.D., Tischler, J.Z., 2002. Three-dimensional X-ray structural microscopy with submicrometre resolution. *Nature* 415, 887-890.
- Laue, M., Tank, F., 1913. Die Gestalt der Interferenzpunkte bei den Röntgenstrahlinterferenzen. *Annalen der Physik* 346, 1003-1001.
- Liebl, C., Kuntcheva, B., Kruhl, J.H., Kunze, K., 2007. Crystallographic orientations of quartz grain-boundary segments formed during dynamic recrystallization and subsequent annealing. *European Journal of Mineralogy* 19/5, 735-744.
- Li Jun, Jacka, T.H., Budd, W.F., 1996. Deformation rates in combined compression and shear for ice which is initially isotropic and after the development of strong anisotropy. *Annals of Glaciology* 23, 247-252.
- Main, J.F., 1887. Note on some experiments on the viscosity of ice. *Proceedings of the Royal Society of London* A42, 491-501.
- Mandal, S., Pradeep, K.G., Zaefferer, S., Raabe, D., 2014. A novel approach to measure grain boundary segregation in bulk polycrystalline materials in dependence of the grain boundaries' five rotational degree of freedom. *Scripta Materialia* 81, 16-19.
- McConnel, J.C., Kidd, D.A., 1888. On the plasticity of glacier and other ice. *Proceedings of the Royal Society of London* A44, 331-367.
- McLaren, A.C., 1986. Some speculations on the nature of high-angle grain boundaries in quartz rocks. *Laboratory Studies: The Paterson Volume* (ed. by B.E. Hobbs and H.C. Heard), Vol. 36, pp. 233-245. American Geophysical Union, Washington.
- Means, W.D., 1980. High temperature simple shearing fabrics: a new experimental approach. *Journal of Structural Geology* 2, 197-202.
- Mittermijer, E.J., 1987. *Fundamentals of materials science*. Springer, Berlin-Heidelberg, pp. 594.

- Montagnat, M., Blackford, J.R., Piazzolo, P., Arnaud, L., Lebensohn, R.A., 2011. Measurements and full-field predictions of deformation heterogeneities in ice. *Earth and Planetary Science Letters* 305, 153-160.
- Panozzo Heilbronner, R., Pauli, C., 1993. Integrated spatial and orientation analysis of quartz *c*-axes by computer-aided microscopy. *Journal of Structural Geology* 15, 369-382.
- Passchier, C.W., Trouw, R.A.J., 2005. *Microtectonics*, 2nd edition, Springer, Berlin-Heidelberg, pp. 366.
- Pauling, L., 1935. The structure and entropy of ice and of other crystals with some randomness of atomic arrangement. *Journal of the American Chemical Society* 57, 2680-2684.
- Paternell, M., Kohlmann, F., Russell-Head, D.S., Wilson, C.J.L., Seiler, C., Gleadow, A.J.W. 2009. A new approach to crystallographic orientation measurements for apatite fission track analysis: Effects of crystal morphology and implication for automation. *Chemical Geology* 265, 527-539.
- Paternell, M., Hasalová, P., Wilson, C.J.L., Piazzolo, S., Schulmann, K., 2010. Evaluating quartz crystallographic preferred orientations and the rule of deformation partitioning using EBSD and fabric analyser techniques. *Journal of Structural Geology* 32, 803-817.
- Paternell, M., Russell-Head, D.S., Wilson, C.J.L., 2011. A technique for recording polycrystalline structure and orientation during in situ deformation cycles of rock analogues using an automated fabric analyser. *Journal of Microscopy* 242, 181-188.
- Paternell, M., Dierckx, M., Wilson, C.J.L., Piazzolo, S., 2014. Quantification of the microstructural evolution of polycrystalline fabrics using FAME: application to *in situ* deformation of ice. *Journal of Structural Geology* 61, 109-122.
- Pfaff, F., 1875. Versuche über die Plasticität des Eises. *Annalen der Physik* 231, 169-174.
- Piazzolo, S., Wilson, C.J.L., Luzin, V., Brouzet, C., Paternell, M., 2013. Dynamics of ice mass deformation: Linking processes to rheology, texture and microstructure. *Geochemistry Geophysics Geosystems* 14, 4185-4194.
- Poirier, J.P., 1985. *Creep of Crystals*. Cambridge University Press, Cambridge (UK), 260pp.
- Prior, D.J., Boyle, A.P., Brenker, F., Cheadle, M.C., Day, A., Lopez, G., Peruzzo, L., Potts, G.J., Reddy, S., Spiess, R., Timms, N.E., Tribby, P., Wheeler, J., Zetterström, L., 1999. The application of electron backscatter diffraction and orientation contrast imaging in the SEM to textural problems in rocks. *American Mineralogist* 84, 1741-1759.
- Prior, D.J., Lilly, K., Seidermann, M., Vaughan, M., Becroft, L., Easingwood, R., Diebold, S., Obbard, R., Daghlian, C., Baker, I., Caswell, T., Golding, N., Goldsby, D., Duraham, W.B., Piazzolo, S., Wilson, C.J.L., 2015. Making EBSD on water ice routine. *Journal of Microscopy* 259, 237-256.

- Reusch, E., 1864. Beiträge zur Lehre vom Eis. *Annalen der Physik* 197, 573-578.
- Roesler, J. Harders, H., Baeker, M., 2007. Mechanical behaviour of engineering materials: Metals, Ceramics, Polymers, and composites, Springer-Verlag, Berlin, pp. 534.
- Rolland du Roscoat, S., King, A., Philip, A., Reischig, P., Ludwig, W., Flin, F., Meysonnier, J., 2011. Analysis of Snow Microstructure by Means of X-Ray Diffraction Contrast Tomography. *Advanced Engineering Materials* 13, 128-135.
- Rollet, A.D., Lee, S.-B., Campman, R., Rohrer, G.S., 2007. Three-dimensional characterization of microstructure by electron back-scatter diffraction. *Annual Review of Material Research* 37, 627-658.
- Rowenhorst, D.J., Gupta, A., Feng, C.R., Spanos, G., 2006. 3D crystallographic and morphological analysis of coarse martensite: Combining EBSD and serial sectioning. *Scripta Materialia* 55, 11-16.
- Russell-Head, D. S. and Wilson, C.J.L., 2001. Automated fabric analyser system for quartz and ice. *Geological Society of Australia. Abstracts* 64, 159.
- Sander, B., 1948, Einführung in die Gefügekunde der geologischen Körper: Band 1. Springer-Verlag, Wien, pp. 215.
- Schmid, E., Boas, W., 1935. Kristallplastizität – Mit besonderer Berücksichtigung der Metalle. Springer-Verlag, Berlin-Heidelberg, pp. 373.
- Schulsen, E.M., Duval, P., 2009. Creep and fracture of ice, Cambridge University Press, Cambridge (UK), pp. 401.
- Steinemann, S., 1958. Experimentelle Untersuchungen zur Plastizität von Eis. Beiträge zur Geologie der Schweiz, geotechnische Serien, *Hydrologie* 10, 1-72.
- Sutton, A. P., Ballu, R. W., 2006. Interfaces in crystalline materials. Clarendon Press, Oxford, pp. 819.
- Swygenhoven, H.V., 2002. Grain boundaries and dislocations. *Nature* 296, 66-67.
- Turner, F.J., Weiss, L.E., 1963. Structural analysis of metamorphic tectonites. McGraw_Hill, New York, pp. 545.
- Urai, J.L., Humprheys, F.J., Burrows, S.E., 1980. *In-situ* studies of the deformation and recrystallization of rhombohedral camphor. *Journal of Materials Science* 15, 1231-1240.
- Venables, J.A., Harland, C.J., 1973. Electron back-scattering patterns: a new technique for obtaining crystal-lographic information in the scanning electron microscope. *Philosophical Magazine* 27, 1193-1200.
- Vernon, R.H., 1976. *Metamorphic Processes*. Allen & Unwill, London, pp. 247.
- Voll, G. 1960. New work on petrofabrics. *Liverpool and Manchester Geological Journal* 2, 503-567.

- Weertman, J., 1955. Theory of steady-state creep based on dislocation climb. *Journal of Applied Physics* 26, 1213-1217.
- Weertman, J., 1983. Creep deformation of ice. *Annual Review of Earth and Planetary Sciences* 11, 215-240.
- Wenge Yang, Larson, B.C., Tischler, J.Z., Ice, G.E., Budai, J.D., Liu, W., 2004. Differential-aperture X-ray structural microscopy: a submicron-resolution three-dimensional probe of local microstructure and strain. *Micron* 35, 431-439.
- White, J.C., White, S.H., 1981. On the structure of grain boundaries in tectonites. *Tectonophysics* 39, 143-170.
- Wilén, L.A., 2000. A new technique for ice-fabric analysis. *Journal of Glaciology* 46, 129-139.
- Wilson, C.J.L., 1981. Experimental folding and fabric development in multi-layered ice. *Tectonophysics* 78, 139-159.
- Wilson, C.J.L., 1983. Foliation and strain development in ice mica models. *Tectonophysics* 92, 93-122.
- Wilson, C.J.L., Russell-Head, D.S., Sim, H.M., 2003. The application of an automated fabric analyser system to the textural evolution of folded ice layer in shear zones. *Annals of Glaciology* 37, 7-17.
- Wilson, C.J.L., Russell-Head, D.S., Kunze, K., Viola, G., 2007. The analysis of quartz c-axis fabrics using a modified optical microscope. *Journal of Microscopy* 227, 30-41.
- Wilson, C.J.L., Peternell, M., 2012. Ice deformed in compression and simple shear: control of temperature and initial fabric. *Journal of Glaciology* 58, 11-22.
- Wilson, C.J.L., Peternell, M., Piazzolo, S., Luzin, V., 2014. Microstructure and fabric development in ice: Lessons learned from *in situ* experiments and implications for understanding rock evolution. *Journal of Structural Geology* 61, 50-77.
- Wolf, D., Yip, S., 1992. *Materials Interfaces*. Chapman & Hall, London, pp. 716.
- Xi Wang, Flin, F., Coeurjolly, D., Lesaffre, B., 2013. Digital Flow for grain segmentation from 3D microtomographic images of snow. *International Snow Science Workshop (ISSW)*, Oct 2013, Grenoble – Charmonix Mont-Blanc, France, 83-86.
- Zaefferer, S., Wright, S. I., Raabe, D., 2008. Three-dimensional orientation microscopy in a focused ion beam-scanning electron microscope: A new dimension of microstructure characterization. *Metallurgical and Materials Transactions A* 39, 374-389.

2. FAME: Software for analysing rock microstructures

Abstract

Determination of rock microstructures leads to a better understanding of the formation and deformation of polycrystalline solids. Here, we present FAME (Fabric Analyser based Microstructure Evaluation), an easy-to-use MATLAB®-based software for processing datasets recorded by an automated fabric analyser microscope. FAME is provided as a MATLAB®-independent Windows® executable with an intuitive graphical user interface. Raw data from the fabric analyser microscope can be automatically loaded, filtered and cropped before analysis. Accurate and efficient rock microstructure analysis is based on an advanced user-controlled grain labelling algorithm. The preview and testing environments simplify the determination of appropriate analysis parameters. Various statistic and plotting tools allow a graphical visualisation of the results such as grain size, shape, c-axis orientation and misorientation. The FAME2elle algorithm exports fabric analyser data to an elle (modelling software)-supported format. FAME supports batch processing for multiple thin section analysis or large datasets that are generated for example during 2D in-situ deformation experiments. The use and versatility of FAME is tested on quartz and deuterium ice samples.

This chapter was published as:

Hammes, D. M. and Peternell, M., 2016. FAME: Software for analysing rock microstructures, Computers & Geosciences 90A, 23-33.

2.1 Introduction

A comprehension of microstructure, the spatial arrangement of crystals and texture is necessary to better understand the formation and deformation of polycrystalline solids such as many rocks, metals, ceramics and ice. Since the invention of polarising microscopy, the universal stage (Fedorow, 1891) and Sander's pioneering works (Sander, 1948), much progress has been made in developing devices and methods for analysing optical

microstructures of polycrystalline aggregates in a thin section. A further milestone was the invention of electron backscatter diffraction (EBSD, Dingley and Randle, 1992) and its application to rock and ice samples (Prior et al., 1999 and 2015). In parallel to the application of EBSD techniques, several automated fabric analyser microscopes were developed to determine rock microstructures and quartz textures from rock and ice thin sections (Panozzo Heilbronner and Pauli, 1993; Fueten, 1997; Wilen, 2000; Hansen and Wilen, 2002; Wilson et al., 2003 and 2007). These systems enable the analysis of whole thin sections with high accuracy and resolution in relative short time frames (Peternell et al., 2010). The Fabric Analyser G50 (Wilson et al., 2003 and 2007) enables *c*-axis orientation measurement of uniaxial minerals with birefringence colours in the second or higher orders such as calcite, tourmaline or zircon from a standard 25-30 micron thick thin section, and <500 micron thick ice sections. MATLAB® based “fabric analyser microstructure evaluation” scripts were developed to automatically determine rock microstructure and texture from whole thin sections (Peternell et al., 2014 and Wilson et al., 2014), or continuously during 2d *in situ* deformation experiments (Peternell et al., 2011).

In this study we present further developments of the initial MATLAB scripts into a user friendly stand-alone software package FAME, which offers a range of new analysis and testing functions. These functions include: (1) A “crop tool” and “preview” function that allows the user to select an arbitrary area within a thin section; (2) A new “testing” environment that semi-automatically supports the user to find appropriate parameters for automatic grain labelling analysis; (3) A new “step growth” operation that enables the user to more precisely segment grain shapes from initial pixel scanned data; (4) An option to plot eigenvalues that relate to texture and its strength.

The FAME software is compiled for Windows® operation systems Windows® 7 and 8 with the installation of the freeware MATLAB® Compiler Runtime (MCR, <http://de.mathworks.com/products/compiler/mcr/>).

2.2 FAME Software

2.2.1 Data processing (overview)

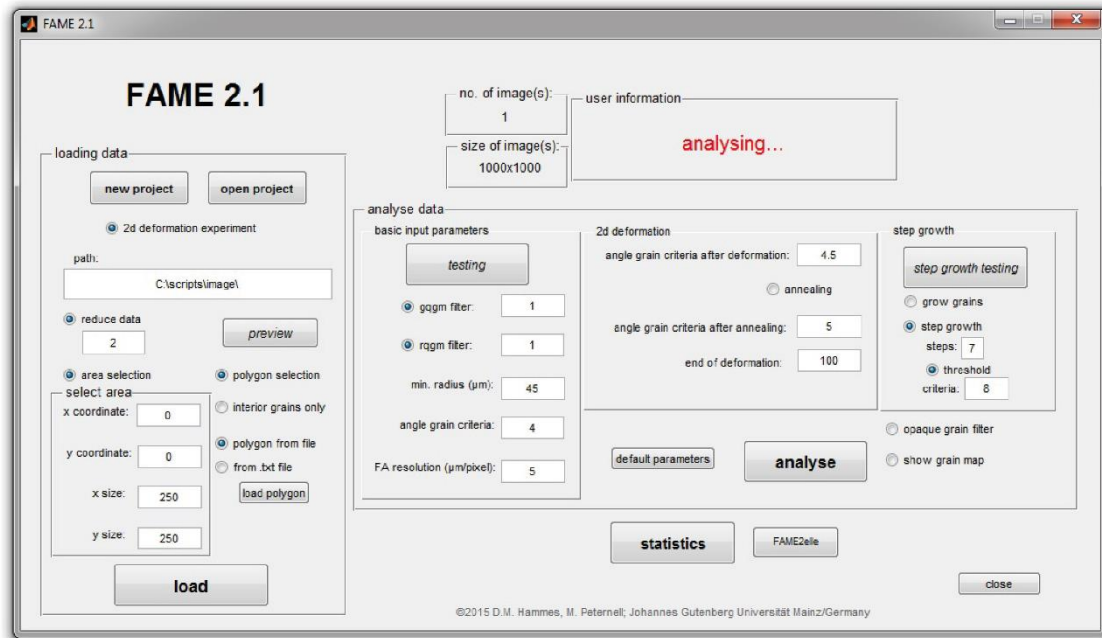


Figure 2.1. Main graphical user interface of FAME.

FAME is controlled by its graphical user interface (GUI; Fig. 2.1) and three main FAME processes (“loading data”, “analysing data” and “data output”), and related sub-processes shown in figure 2. The “loading” and “analysing” functions are similar to the original scripts described in Peternell et al. (2014), and are summarised in the following.. The “loading data” main process opens an already existing project or imports (“load”) the binary Fabric Analyser (.cis) data file, containing pixel related information such as *c*-axis orientation in polar coordinates, retardation, and geometric and retardation quality for each pixel in the field of view (Peternell et al., 2011; Figs. 1, 2). A data “preview” tool allows the user to access the raw image files, and to evaluate the effect to filters applied to the raw data. The “load” sub-process converts the *c*-axis orientation data to a MATLAB® .mat file into Euler angles using the Bunge convention (mtx_import.txt). This is compatible with EBSD software such as hkl® or oim® and the open source MATLAB® toolbox MTEX (Hielscher and Schaeben, 2008). Large datasets can be re-

duced (here called “reduce data”) by loading each n^{th} ($n \in \mathbb{N}$) measure point, which enables analysis on slower computers. However, excessive data reduction may lead to inaccurate results, and therefore any reduction must be tested carefully (Peternell et al., 2014).

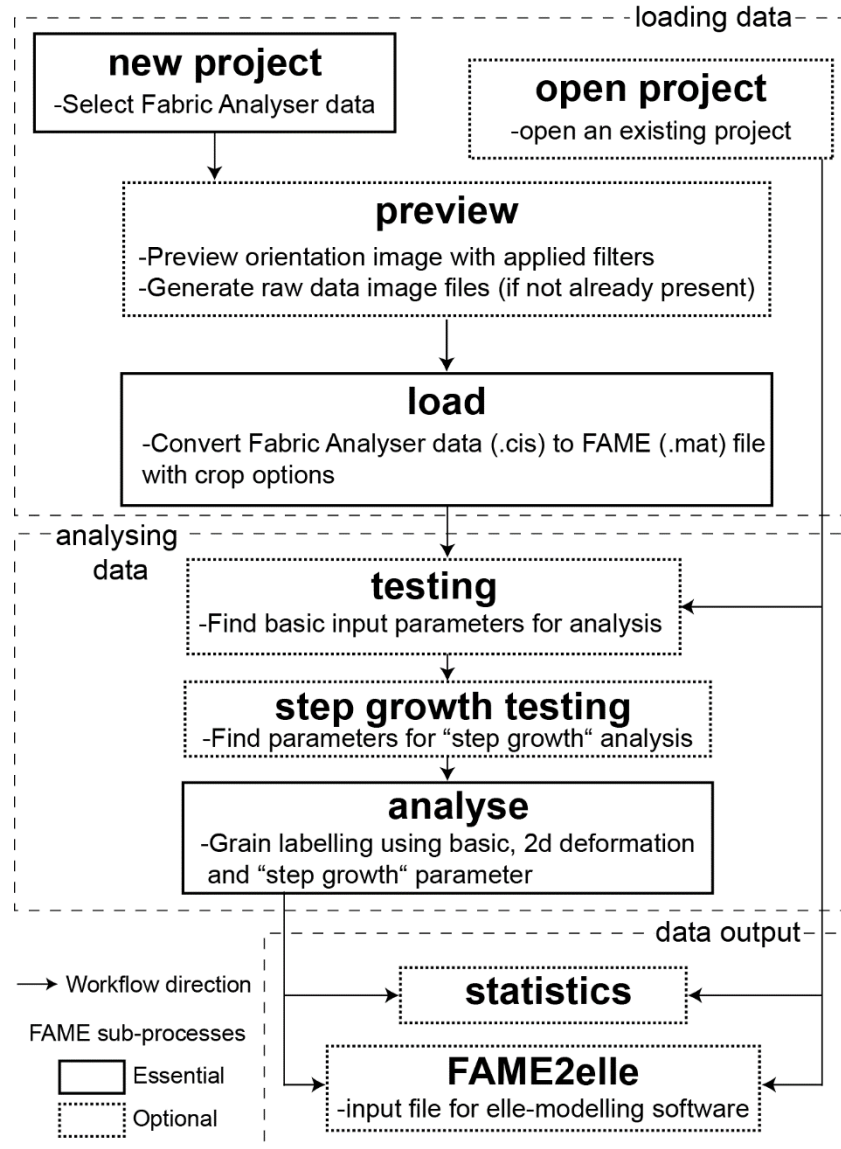


Figure 2.2. Simplified work flow of FAME.

The “analysis” process uses the generated .mat file to label grains and determine grain microstructures (Fig. 2.1), and the “testing” and “step growth testing” tools simplify the determination of the required parameters. Grain labelling is the key for any automated microstructural analysis, and is based on the computer capability to recognise grains from pixel data. The labelling is performed with the MTEX function “calcGrains”, using a Voronoi decomposition based algorithm and results in a polygonal grain structure (Bachmann et al., 2011). It is then converted into a FAME grain that consists of a pixel grain

structure; with a number of connected pixels sharing a common grain identity. All information from a Fabric Analyser measured pixel is attributed to the congruent FAME grain pixel including mean grain orientation. FAME grains are colour coded equal to Fabric Analyser AVA (“Achsenverteilungsanalyse”; Sander, 1948) (axial distribution maps), where each colour represents a unique *c*-axis orientation (Fig. 2.3a). A FAME grain map represents all grains of a single FAME analysis (Fig. 2.3b). To run an analysis, several input parameters (Table 1) are necessary and discussed in Peternell et al. (2014). The resulting data can be used for further statistical analysis (“statistics” in Figs. 2.1, 2.2), such as plotting a mineral shape preferred orientation, grain size diagram, *c*-axis orientation stereonet, distribution density function, and *c*-axis misorientation maps. Furthermore, the data can be exported to a file format supported by the elle (Jessel et al., 2001) modelling software.

Figure	Angle grain criteria 1*	Angle grain criteria 2*	Angle grain criteria 3*	Minimum radius (µm)	Growth steps	Growth criteria
2.2b)	3.526	---		40	---	
2.2c)	3.526	---		40	6	9
2.6a)	3.295	4.95	5.158	63	---	
2.6b)	3.295	4.95	5.158	63	6	9
2.8b)	2.5	---		40	7	1

*In case of in situ deformation experiment criteria 1 at beginning and criteria 2 at end of deformation, and criteria 3 at end of annealing

Table 2.1: Input parameters for grain labelling. Specified using the “testing” and “step growth testing” toolboxes. For all figures: Reduce data=2, Geometric quality filter=1, Retardation quality filter=1.

2.2.2 Data preview and cropping tools

The “preview” function (Fig. 2.2) offers the possibility to display raw or filtered Fabric Analyser data directly on the computer screen. Filter criteria are the reduce data, geometric quality and retardation quality filters (Peternell et al., 2014). In the case of a batch data analysis the user can select the image number for preview. Most rock microstructures are not homogenous and regions of interest may be irregular in shape. Then a polygonal shape can be drawn manually on a displayed preview, or any rectangular region can be selected by typing in the appropriate x-y coordinates corresponding to height and width of the area to be analysed.

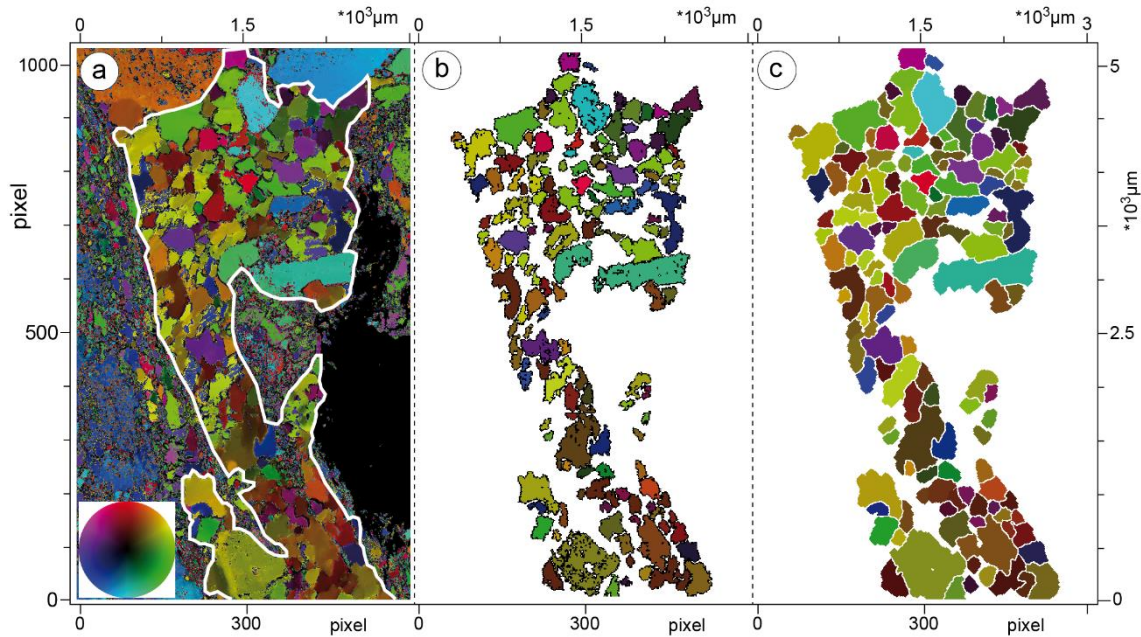


Figure 2.3. Data cropping with FAME (a) AVA (“Achsenverteilungsanalyse”; axial distribution map) from annealed quartzite, Scotland, with a quartz-rich lense in the centre (white outline); Colour wheel indicates c -axis orientation for each pixel in the field of view; (b) Grain map of interior grains of (a); colours indicate mean c -axis orientation for each grain; (c) Image of (b) with applied FAME “step growth” algorithm (Section 2.2.4).

Fig. 2.3 is an example of the cropping tool applied to an AVA image from a quartz lense within a mylonitic orthogneis from the Bohemian massif (Peternell et al., 2011). The irregularly shaped quartz lense is outlined and separated from the surrounding feldspar and mica dominated domains by using the “crop” function (Fig. 2.3a). To avoid a border effect, by growing grains close to an artificial boarder, grains in the whole data set were labelled and grain centres located inside the selected polygon were chosen for further data processing (Fig. 2.3b). The final FAME grain map replicates the original grain and orientation distributions (Fig. 2.3a, c, Table 2.2). White areas inside the FAME grain maps (Fig. 2.3c) correlate with areas that contain minor amount of feldspar and very fine grains ($\leq 5 \mu\text{m}$), which are less than the 5 microns per pixel resolution of this analysis (Fig. 3).

2.2.3 Testing

The quality of any grain map depends on 4 parameters used during the “analysis” function, namely: (1 and 2) Geometric and retardation quality, named in the GUI as geometric quality grain map (gqgm) and retardation quality grain map (rqgm) filters, are used to

evaluate the initial quality of each pixel in the field of view, with a range between 0 (rejected) to 100 (excellent; Peternell et al., 2009); (3) The angle grain criteria (Table 2.1) is a misorientation angle, which defines the position of grain boundaries (Bachmann et al., 2011); and (4) The minimal grain radius, is a lower grain size threshold that depends on the maximum resolution of a Fabric Analyser measurement (Peternell et al., 2014). Manual determination of the ideal parameters can be difficult and time intensive, because every single grain map has to be evaluated by the user. Until now, there has been no algorithm available to automatically evaluate how well a FAME grain map matches the original sample. To ease this task the “testing” environment (Fig. 2.2) was developed

A range, given by the minimal and the maximal values, and the number of data points in the range are chosen for each of the four parameters. For each combination the accompanying grain map is generated and stored as a .jpeg file. If k, l, m and n are the number of points of the 4 parameters, then different $k \cdot l \cdot m \cdot n$ combinations are possible. The user can now select a suitable image and use the appropriate parameters for further analysis or improve the results with a second round of testing. Rather than manually adjusting these parameters, this automatic operation seems to be more time efficient, with a single image generation taking no more than a few minutes. (for information about calculated times please see FAME manual).

Sample	Figure	Method	Number grains	Grain size (μm)	Area covered by grains (%)	Correct indexed grains* (%)
Quartz lens	2b)	FAME (no growth)	149	164	24.2	85
	2c)	FAME (step growth)	132	220	37.1	92
	2a)	Manually digitized	142	200	34.1	100
Annealed ice	6b)	FAME (no growth)	164	297	49.5	76
	6c)	FAME (step growth)	138	404	72.7	90
	6a)	Manually digitized	127	423	73.2	100
Mt. Isa	---	FAME (no growth)	293	284	89.3	97
	8b)	FAME (step growth)	292	324	94.9	97
	3	Manually digitized	295	322	96.3	100

*Manually digitized grains that match position with approx. same shaped and oriented FAME grain.

Table 2.2: Input parameters for grain labelling. Specified using the “testing” and “step growth testing” toolboxes. For all figures: Reduce data=2, Geometric quality filter=1, Retardation quality filter=1.

To demonstrate the “testing” operation a region of almost pure quartz (Fig. 2.4) was selected. To reduce the number of generated grain maps, only 4 values of the minimal

radius and 6 of the angle grain criteria were chosen, with the geometric and retardation quality filter set to one. The resulting array of 24 images is shown in Fig. 2.5. In comparison with original grain map (Fig. 2.4) a minimal radius of 63 and an angle grain criteria of 2.48 produced the best results (Table 2.2).

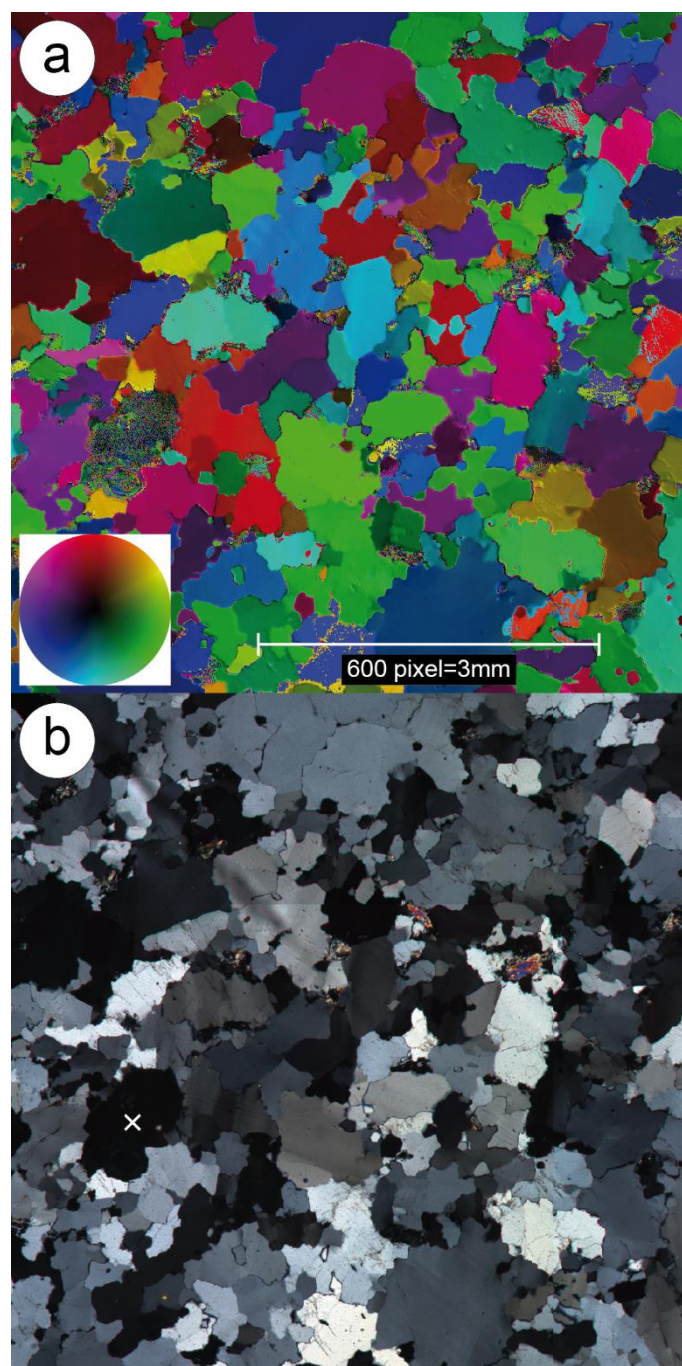


Figure 2.4. AVA (axial distribution analysis) image (a) and cross polarised microphotograph (b) of a quartzite thin section from Mt Isa, Australia; Colour wheel indicates c-axis orientation. (Sample 7905; Wilson, 1973)

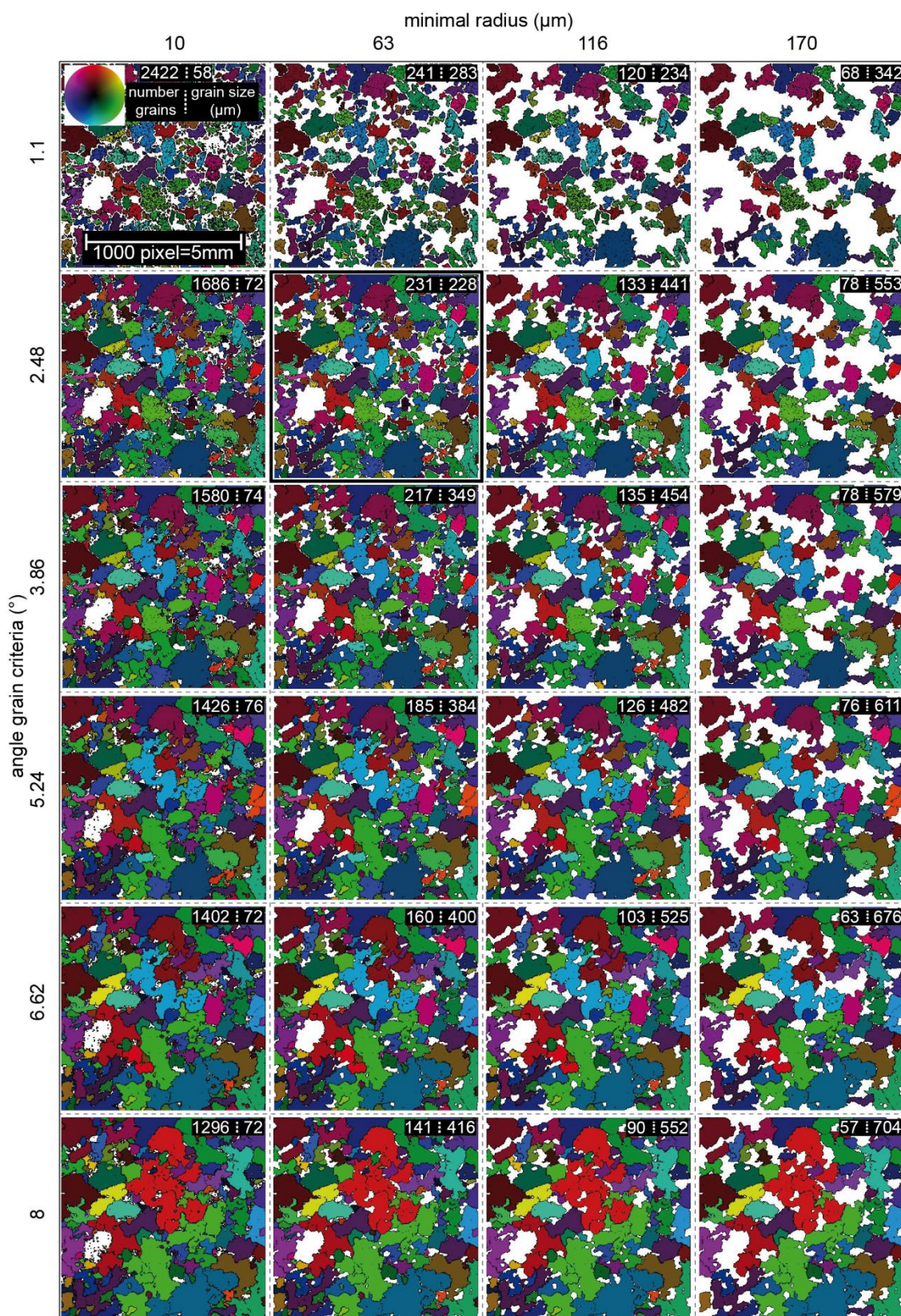


Figure 2.5. Results of “testing” environment for the Mt Isa quartzite section (Fig. 3) to determine best parameters for “calc grain” algorithm. 24 possible combinations of “minimal radius” and “angle grain” are shown. Grain map with “minimal radius” = 63 μm and “angle grain” criteria = 3.86° leads to best result compared to the orientation image (Fig. 3); Colour wheel indicates *c*-axis orientation.

2.2.4 Step growth

Fabric Analyser based MTEX grain maps are in most cases incomplete in comparison to the original grains identified in the thin section by eye (Figs. 2.3a, b). Compared to their appearance in the thin section, MTEX grains are statistically smaller (Table 2) and several original grains cannot be indexed with FAME (white holes). This is caused by miss-indexed pixels in the AVA image, particular at grain boundaries and adjacent to inclusions (Peternell et al., 2009 and 2010), or in grains with a very steep dipping *c*-axis orientation or a strongly deformed crystal lattice. FAME offers a pixel wise growth function (“step growth”, Fig. 2.1) that enables the user to reduce these effects of miss-indexing (Fig. 2.6).

The first step of the grow function (Fig. 2.6a) is to transform the MTEX grain structure, which contains information about the labelled grains as vertices, to an x-y- coordinate related matrix structure. The matrix has the same dimensions as the Fabric Analyser input pixel image. Each matrix entry (pixel) is linked to the position corresponding to the *c*-axis azimuth and plunge from the MTEX generated grain map, and a grain affiliation integer. The resulting matrix has the dimension “image height” x “image width” x 3 (*c*-axis azimuth, dip, affiliation integer). The “growth” algorithm (Fig. 2.6a) is a simple and fast algorithm applied to each pixel of the FAME matrix, starting from the upper left. Fig. 6b illustrates the principles of the algorithm for one step. For any empty entry (n, m) it is checked clockwise whether any of the 4 neighbouring entries (4-connected) are non-empty, and starts with entry (n, m-1). If it is empty (Fig. 2.6b) the next clockwise entry (n+1, m) is investigated, and if not empty (Fig. 2.6b) its colour is attributed to entry (n, m). This process is carried out for every entry in the original matrix. In this way, grains increase their size at the expense of the empty space. “Growth” can be repeated until the user decides that the required result is achieved (Fig. 2.6c; “steps” in “step growth”, Fig. 2.1). After “Growth” is finished, neighbouring grains with an orientation angle difference smaller than a user-defined threshold (“criteria” in “step growth”, Fig. 2.1) are merged into a new and larger grain. This is advantageous where an original grain was split during MTEX grain labelling, e.g. because of the presence of subgrains. FAME offers a growth testing environment (“step grow testing”, Fig. 2.1) to determine the best number of grow steps and merging threshold. The function is always applied to the complete loaded dataset and the grain affiliation integer for each entry of the resulting data matrix is used for area and shape statistics. For a user friendly visualization of the final FAME grain map,

a cut algorithm is used to generate a white grain boundary around each grain, and the map can be converted to a RGB colour image (Fig. 2.6c).

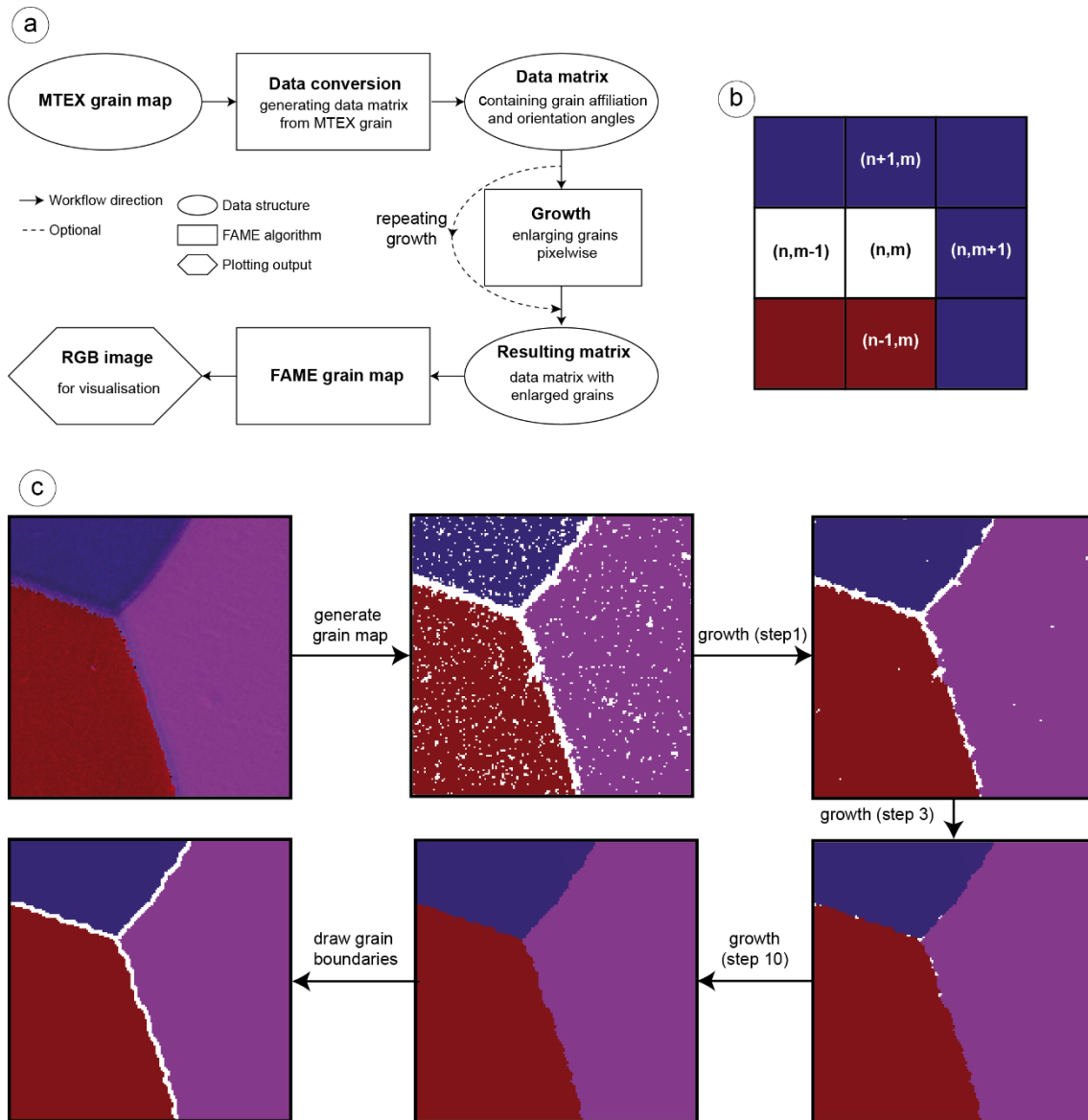


Figure 2.6. Principles of the “step growth” algorithm. (a) Flow chart of algorithm. (b) Sketch to visualize the “step growth” pattern. White pixels indicate areas that could not be attributed to a grain by the “calc grain” algorithm. Each other colour defines a grain with a mean c -axis orientation; (c) “step growth” demonstrated using a simplified example of three intersecting grains.

The result of “step growth” (Fig. 2.3c) demonstrates that without any growth algorithm the position of grains and their basic shape (Fig. 2.3a, b), but growing grains leads to better shaped correspondence and the grain statistics are more similar (Fig. 2.3c, Table 2.2). Most non-labelled regions in Fig. 2.3b and 2.3c consist of either small grain aggregates, below the grain size threshold, or belong to feldspar or mica grains that cannot be analysed with the Fabric Analyser. The “step growth” algorithm can be used to improve

grain statistics, particularly for batch data analysis, e.g. time series analysis of a changing microstructure during 2d in situ deformation experiments (e.g. Peternell et al., 2011 and 2014). In such an experiment a 5 x 5 mm x ~250 μ thin section of deuterium ice was deformed at -7°C for 22 hours followed by 9.5 hours of annealing at the same temperature. The final microstructure is shown in Fig. 2.7a.

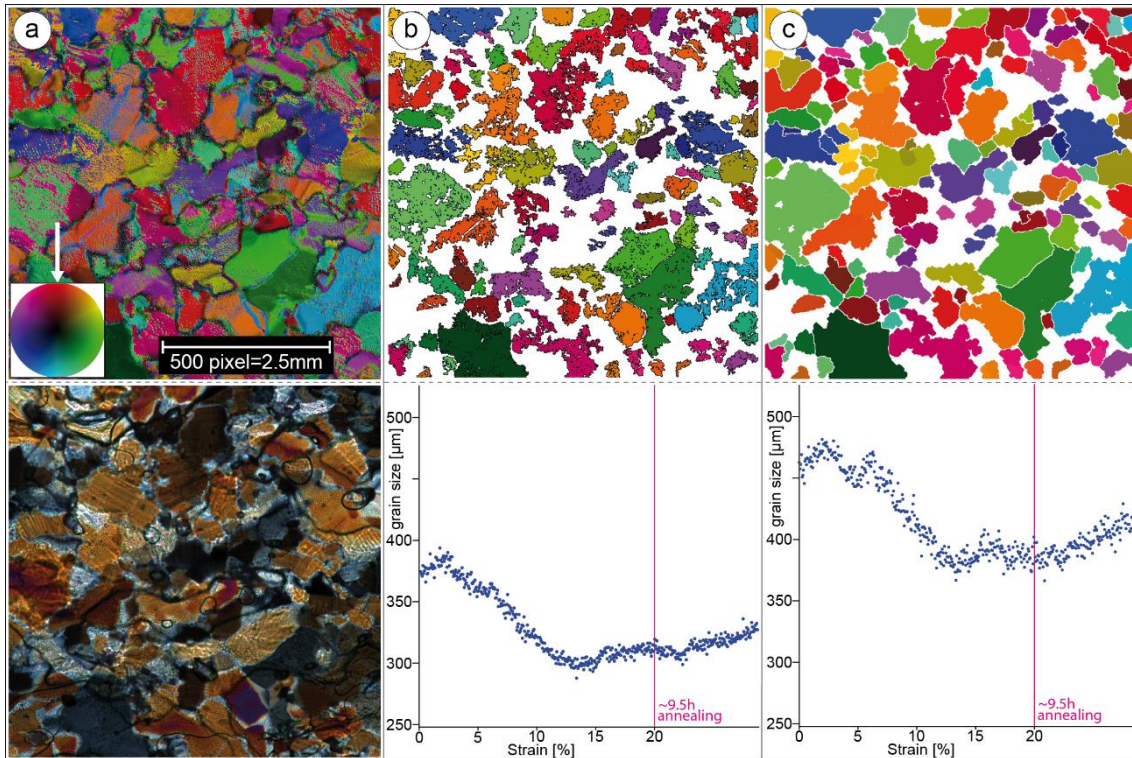


Figure 2.7. FAME step growth applied to deuterated ice (sample 18_4), deformed and annealed after a 2D in situ deformation experiment (Peternell et al., 2014). (a) AVA image (top) and cross polarised image (bottom) of annealed section. (b) Grain map of (a) without any additional grain growth (top) and related grain size evolution diagram (bottom). (c) Grain map (top) and grain size evolution (bottom) with “step growth” applied. Colour wheel indicates *c*-axis orientation; White arrow demonstrates deformation direction

During deformation ice microstructures were recorded every 4 minutes with the Fabric Analyser and processed with FAME without (Fig. 2.7b) and with (Fig. 2.7c) “step growth” applied. Grain size evolution for both cases is shown in grain size versus strain diagrams and represent a typical evolution for deforming ice at high temperatures (Piazolo et al., 2013; Peternell et al., 2014; Wilson et al., 2014). First, the initial grain size increases driven by grain boundary migration processes. After 2-3 percent strain dislocation density controlled grain nucleation becomes dominant leading to grain size reduction. After ~10-13 percent strain grain boundary migration and grain nucleation processes are

balanced and leading to alternating increase and decrease in grain sizes. During the following annealing, grains start to grow again. The resulting grain sizes in Figure 2.7b and c are similar, with a systematically larger grain size where “step growth” was applied (Fig. 2.7c). This is due to the “step growth” input parameters “steps” and “criteria” (Fig. 2.1, Table 2.1) being kept constant for each single analysis. By carefully adjusting “step growth” comparable grain statistics are achieved (Table 2.2), without underestimating the real grain sizes.

2.2.5 Crystallographic orientation (texture) analysis

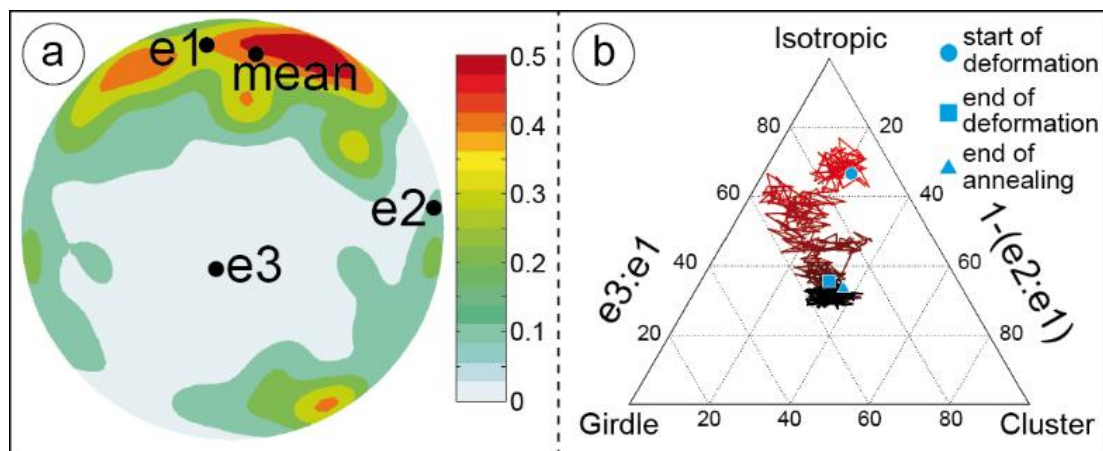


Figure 2.8. Representation of c -axis orientation data. (a) Orientation density plot of annealed deuterated ice (Fig 6c top), using Fisher distribution. Colour bar indicates orientation density. (b) Fabric evolution of *in-situ* deformation experiment (Fig 6c bottom). Eigenvalues $e1$, $e2$, $e3$ are calculated from c -axis orientation tensor for each deformation step. Different strain intervals are indicated in colours.

Crystallographic orientation analysis of rocks was pioneered by Schmidt (1925) and Sander (1948) and is a significant part of the “Gefügekunde” (structural analysis, Turner and Weiss, 1963). The FAME “statistics” tool (Fig. 2.2) offers different methods to visualise crystallographic orientations as shown in Fig. 2.8. A stereographic density plot, based on the Fisher distribution (Fisher et al. 1987; Fig. 2.8a) or the small circle count method (Mellis, 1941). The shape and strength of the orientation data can be determined using the orientation tensor or eigenvalue method (Scheidegger 1965 and Watson 1966). The eigenvalues $e1$, $e2$, $e3$ can be plotted as a ternary diagram with the two indices isotropy $I=e3/e1$ and elongation index $E=1-(e2/e1)$ (Sneed and Folk, 1958). The three end members of the diagram may be redefined as isotropic texture, planar girdles and linear clusters (Benn, 1994). Intermediate shapes are defined using k values, given by

$\ln(e1/e2)/\ln(e2/e3)$ and strength of a texture as its deviation isotropy $\ln(e1/e3)$ (Woodcock, 1977). Batch texture analyses (Fig. 2.7), can also be displayed on a ternary diagram in order to illustrate textural development during progressive deformation (Fig. 2.8b, Pternell et al., 2014). An initial near isotropic *c*-axis orientation distribution decreases into a girdle to cluster type texture and is not significantly changed during subsequent annealing (Fig. 2.8b). Such texture development is similar to results from 3d deformation experiments using neutron x-ray diffraction technique (Piazolo et al., 2013) and *c*-axis orientations from large ice shields (Wilson et al., 2014).

2.2.6 Application of FAME to the elle modelling software

In recent years elle (Jessel et al., 2001; Piazolo et al., 2010; Griera et al., 2011; <http://www.materialsknowledge.org/elle/>) has been developed into a powerful tool for numerical simulation of rock microstructures. A common starting elle file is based on a rock microstructure image file that is either drawn manually with any drawing software, or automatically digitized from a microphotograph, or imported from EBSD analysis (Bons et al. 2008). With the “FAME2elle” function FAME derived grain maps from real rock microstructures can be converted into an elle-supported graphics format (ppm files, Fig. 2.9). Different rock microstructures from Fabric Analyser scans of up to 10 x 10 cm thin sections can be used. In the case of *in situ* deformation experiments, FAME offers the unique possibility to generate elle input files at different stages of the deformation, including full grain statistics, and in the case of uniaxial minerals such as quartz or ice, *c*-axis orientations for each grain. In this way, real rock deformation experiments can be used as an input geometry for numerical simulation and the results from the model at different time steps can be directly compared to the experiments. The workflow of “FAME2elle” is shown in Fig. 2.9a.

A major task of “FAME2elle” is to fill non-labelled regions within a FAME generated microstructure (Fig. 2.9b, white regions), because elle needs all areas to be defined. We developed a 2-seeding procedure to: (1) fill the gaps completely with grain structure and (2) to preserve the original rock microstructure as far as possible. In a first step optional “Seeding large grains” (Fig. 2.9a) will fill larger non-labelled regions with new grains (Fig. 2.9b, black x). Grain sizes of the new grains are normally distributed with mean and standard deviation from the FAME microstructure. The probability of spawning other new grains is limited by the fraction of white area and number of FAME grains. In the

“Seeding small grains” step, the remaining area is filled by small grains with a normal distribution of around a mean grain size defined by the minimal grain radius (section testing). Finally, these new grains will grow pixel wise to fill any remaining gaps in the microstructure (Fig. 2.9a, “Fill area”). The orientation for each grain in elle is given as three Euler angles. The Fabric Analyser can only determine *c*-axis orientations and therefore “FAME2elle” (Fig. 2.2) generates a random third Euler angle for each grain. In the case of newly seeded grains the function offers two ways to attribute crystallographic orientation. The default setting is that a mean orientation is attributed to each grain derived from the Fabric Analyser *c*-axis orientations derived from an adjacent grain. Alternatively, EBSD data from a similar microstructure can be attributed to new grains in both seeding steps (Fig. 9a, “Orientation data”). EBSD orientations in Euler angles can be imported as a single text file. The gap free FAME grain map is scaled to common elle file sizes of 128x128, 256x256px, 512x512px, or 1024x1024px (Fig. 9a, “Scaling”). In the case of non-square FAME grain maps a maximal square will be cut from the centre of the image and rescaled.

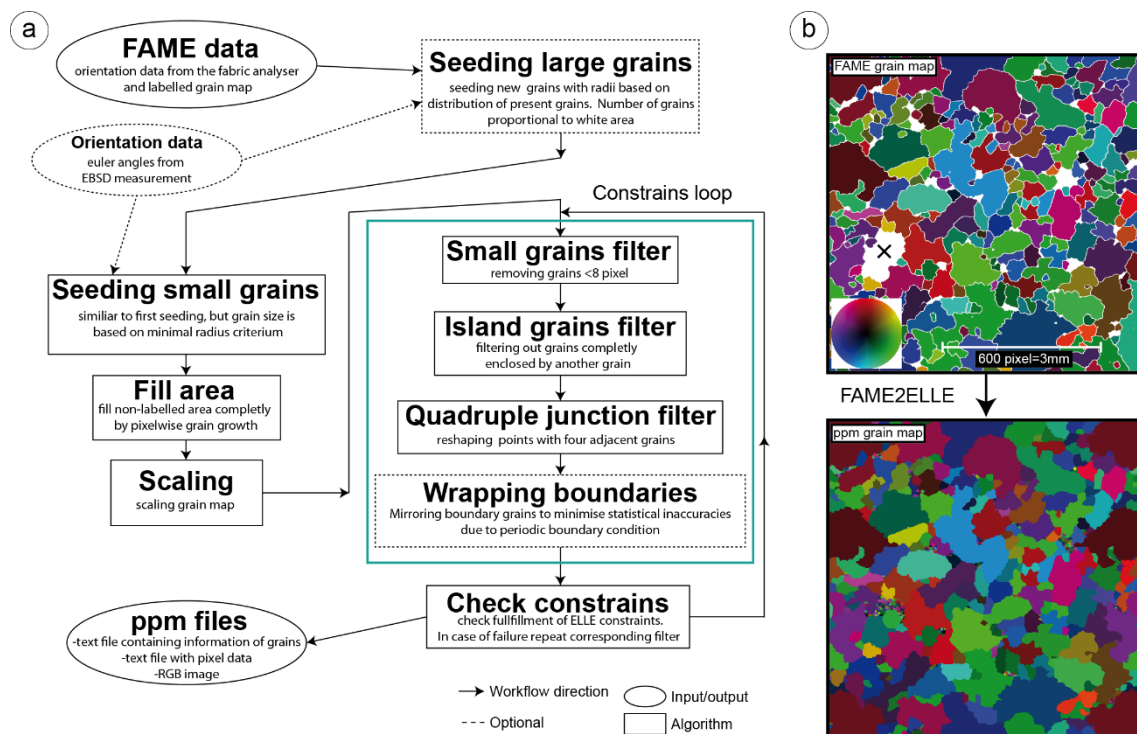


Figure 2.9. Flow chart of FAME2elle (a) and conversion of a FAME grain map (corresponding orientation image: Fig. 3) to an elle supported ppm grain map (b). The statistically seeded grains and the wrapping boundaries are obvious (bottom). Colour wheel indicates *c*-axis orientation.

After scaling the FAME grain map, a series of correcting algorithms are performed to fulfil further elle requirements (Fig. 2.9a, rectangle). All Grains smaller than 8 pixels are removed by merging into a surrounding grain (“Small grains filter”). A region growing algorithm locates grains completely enclosed by another grain and incorporates them into the surrounding grain (“Island grain filter”). Furthermore, quadruple junctions, i.e. single points where four adjacent grains meet, are not supported in elle. The “quadruple junction filter” transforms such junctions into a triple junction by replacing one of the adjacent pixels. elle preferentially uses wrapping boundaries in its simulations (Bons et al. 2008). Grains at the top and left edge are mirrored to the bottom and right, and the corresponding grains are replaced (“Wrapping boundaries”, optional). This series of algorithms will be repeated until all requirements are fulfilled. Finally a grain map (ppm) and pixel orientation (.txt) data file will be generated and can be imported into elle.

FAME2elle is illustrated using the quartz section (Figs. 2.5, 2.9b). Most of the non-labelled area in the FAME grain map (Fig. 2.9b) corresponds to mica and small quartz grains. Because mica is opaque we can only generate a single phase elle grain map. Therefore, new quartz grains are seeded at all non-labelled regions (Fig. 2.9b, white) with mean *c*-axis orientations gained from the Fabric Analyser AVA image (Fig. 2.4a), even if they are artificial at the mica positions. This is not the optimal solution, but a reasonable approach and could be highly improved by adding information from EBSD. Wrapping boundaries causes minor additional changes in the original microstructure. However, the final microstructure in the grain map (ppm) has not changed significantly during the conversion process (Fig. 2.9b).

2.3. Conclusion

The FAME software started originally as an improved and GUI-based version of a set of MATLAB® scripts (Peternell et al., 2014). During its development it had grown into an extensive tool box for importing, processing and visualisation of fabric analyser data. In contrast to the former scripts, a multitude of powerful analysis and statistics tools have been added: A testing environment enables the user to find best parameters for later analysis in a reasonable time, and with the new step growth algorithm improved user-controlled grain segmentation is possible. Other useful features include the cropping toolbox, path diagram plots for *in-situ* deformation experiments and FAME2elle, which exports

FAME grain maps to the elle-compatible ppm format. FAME has already been extensively tested on a diverse range of polycrystalline materials, including quartz, ice, deuterated-ice and Norcamphor. Furthermore, FAME comes with an intuitive graphical user interface and has grown into a powerful software for automated rock microstructure analysis and a bridging platform to numerical simulation of microstructural development with elle.

References

- Bachmann, F., Hielscher, R., Schaeben, H., 2011. Grain detection from 2d and 3d EBSD data – Specification of the MTEX algorithm. *Ultramicroscopy* 111, 1720-1733.
- Benn, D.I., 1994. Fabric shape and the interpretation of sedimentary fabric data. *Journal of Sedimentary Research* A64, 910-915.
- Bons, D.B., Koehn, D., Jessel, M.W., 2008. *Microdynamics Simulation*. Springer Verlag, Berlin, pp. 405.
- Dingley, D.J., Randle, V., 1992. Microtexture determination by electron back-scatter diffraction. *Journal of Materials Science* 27, 4545-4566.
- Fedorow, E.v., 1891. Eine neue Methode der optischen Untersuchung von Krystallplatten in parallelem Lichte. *Tschermak's Mineralogische und Petrographische Mitteilungen*, 12, 505-509.
- Fisher, N.I., Lewis, T., Embleton, B.J.J., 1987. *Statistical analysis of spherical data*. Cambridge University Press, Cambridge, pp. 329.
- Fueten, F., 1997. A computer-controlled rotating polarizer stage for the petrographic microscope. *Computer & Geoscience* 23, 203-208.
- Griera, A., Bons, P.D., Jessel, M.W., Lebensohn, R., Evans, L., Gomez-Rivas, E., 2011. Strain localization and porphyroblast rotation. *Geology* 39, 275-278.
- Hansen, D.P., Wilen, L.A., 2002. Performance and applications of an automated c-axis ice-fabric analyser. *Journal of Glaciology* 48, 159-170.
- Heilbronner, R., 2000. The influence of three-dimensional grain size distribution on the rheology of polyphase rocks. *Journal of Structural Geology* 20, 695-705.
- Hielscher, R., Schaeben, H., 2008. A novel pole figure inversion method: specification of the MTEX algorithm. *Journal of Applied Crystallography* 41, 1024-1037.
- Jessel, M., Bons, P., Evans, L., Barr, T., Stüwe, K., 2001. Elle: The numerical simulator of metamorphic and deformation microstructures. *Computers & Geosciences* 27, 17-30.

- Mellis, O, 1941. Gefügediagramme in stereographischer Projektion. *Zeitschrift für Kristallographie, Mineralogie und Petrographie* 53, 330-353.
- Panozzo Heilbronner, R., Pauli, C., 1993. Integrated spatial and orientation analysis of quartz *c*-axes by computer-aided microscopy. *Journal of Structural Geology* 15, 369-382.
- Peternell, M., Kohlmann, F., Russell-Head, D.S., Wilson, C.J.L, Seiler, C., Gleadow, A.J.W. 2009. A new approach to crystallographic orientation measurements for apatite fission track analysis: Effects of crystal morphology and implication for automation. *Chemical Geology* 265, 527-539.
- Peternell, M., Hasalová, P., Wilson, C.J.L., Piazzolo, S., Schulmann, K., 2010. Evaluating quartz crystallographic preferred orientations and the rule of deformation partitioning using EBSD and fabric analyser techniques. *Journal of Structural Geology* 32, 803-817.
- Peternell, M., Russel-Head, D.S., Wilson, C.J.L., 2011. A technique for recording polycrystalline structure and orientation during in situ deformation cycles of rock analogues using an automated fabric analyser. *Journal of Microscopy* 242, 181-188.
- Peternell, M., Dierckx, M., Wilson, C.J.L., Piazzolo, S., 2014. Quantification of the microstructural evolution of polycrystalline fabrics using FAME: application to *in situ* deformation of ice. *Journal of Structural Geology* 61, 109-122.
- Piazzolo, S., Jessell, M.W., Bons, P.D., Evans, L., Becker, J.K., 2010. Numerical Simulations of Microstructures Using the Elle Platform: A Modern Research and Teaching Tool. *Journal of the Geological Society of India* 75, 110-127.
- Piazzolo, S., Wilson, C.J.L, Luzin, V., Brouzet, C., Peternell, M., 2013. Dynamics of ice mass deformation: Linking processes to rheology, texture and microstructure. *Geochemistry, Geophysics, Geosystems* 14, 4185-4194. DOI 10.1002/ggge.20246
- Prior, D.J., Boyle, A.P, Brenker, F., Cheadle, M.C., Day, A., Lopez, G., Peruzzo, L., Potts, G.J., Reddy, S., Spiess, R., Timms, N.E., Tribby, P., Wheeler, J., Zetterström, L., 1999. The application of electron backscatter diffraction and orientation contrast imaging in the SEM to textural problems in rocks. *American Mineralogist* 84, 1741-1759.
- Prior, D.J., Lilly, K., Seidermann, M., Vaughan, M., Becroft, L., Easingwood, R., Diebold, S., Obbard, R., Daghlian, C., Baker, I., Caswell, T., Golding, N., Goldsby, D., Duraham, W.B., Piazzolo, S., Wilson, C.J.L., 2015. Making EBSD on water ice routine. *Journal of Microscopy* 28, DOI: 10.1111/jmi.12258
- Sander, B., 1948, Einführung in die Gefügekunde der geologischen Körper: Band 1. Springer-Verlag, Wien, pp. 215.
- Scheidegger, A.E., 1965. On the statistics of orientation of bedding planes, grain axes, and similiar sedimentological data. United States Geological Survey Professional Paper 525-C, 164-167.
- Schmidt, W., 1925. Gefügestatistik. *Tschermaks Mineralogische u. Petrographische Mitteilungen* 38, 392-423.

- Sneed, E.D., Folk, R.L., 1958. Pebbles in lower Colorado River, Texas, a study in particle morphogenesis. *Journal of Geology* 66, 114-150.
- Turner, F.J., Weiss, L.E., 1963. *Structural analysis of metamorphic tectonites*. McGraw Hill, New York, pp. 545.
- Watson, G.S., 1966. The statistics of orientation data. *Journal of Geology* 74, 786-797.
- Wilén, L.A., 2000. A new technique for ice-fabric analysis. *Journal of Glaciology* 46, 129-139.
- Wilson, C.J.L., 1973. The prograde microfabric in a deformed quartzite sequence, Mount Isa, Australia. *Tectonophysics* 19, 39-81.
- Wilson, C.J.L., Russell-Head, D.S., Sim, H.M., 2003. The application of an automated fabric analyser system to the textural evolution of folded ice layer in shear zones. *Annals of Glaciology* 37, 7-17.
- Wilson, C.J.L., Russell-Head, D.S., Kunze, K., Viola, G., 2007. The analysis of quartz c-axis fabrics using a modified optical microscope. *Journal of Microscopy* 227, 30-41.
- Wilson, C.J.L., Peternell, M., Piazzolo, S., Luzin, V., 2014. Microstructure and fabric development in ice: Lessons learned from *in situ* experiments and implications for understanding rock evolution. *Journal of Structural Geology* 61, 50-77.
- Woodcock, N.H., 1977. Specification of fabric shapes using an eigenvalue method. *Geology Society of America Bulletin* 88, 1231-1236.

3. Reconstruction of 3D grain boundaries from rock thin sections, using an advanced polarised-light microscopy method

Abstract

Grain boundaries play a significant role in materials by initiating reactions and collecting impurities. Here we present FAGO (Fabric Analyser Grain boundary reConstruction), a first step towards the automatic determination of three-dimensional (3D) grain boundary geometry using polarised light. The trace of the grain boundaries from 2D rock thin sections are determined primarily from data acquired using an automatic fabric analyser microscope and the FAME software (Fabric Analyser based Microstructure Evaluation; Peternell and colleagues and Hammes and Peternell). Based on the Fabric Analyser G50's unique arrangement of nine differently oriented light sources the retardation can be determined independently for each light direction and at each pixel in the field of view. FAGO combines these retardation datasets for each individual pixel together with retardation profiles across grain boundaries, to determine the orientations of the boundaries. The grain boundary traces are then broken up into segments of equal orientation, using the profile-obtained orientation data. Finally, a 3D grain boundary model is reconstructed. The data processing is almost fully automatic using the MATLAB® environment. Only minor manual inputs are required.

This chapter was accepted as:

Hammes, D. M. and Peternell, M., in press. Reconstruction of 3D grain boundaries from rock thin sections, using an advanced polarised-light microscopy method. Journal of Microscopy. Early view available online: <http://onlinelibrary.wiley.com/doi/10.1111/jmi.12605/full>

3.1 Introduction

Grain boundaries are planar defects in the lattice that separate regions of different crystallographic orientation (Vernon, 1976; Humphreys and Hatherly, 2004). High angle-grain boundaries with misorientations of $\sim 10^\circ$ - 20° (Humphreys and Hatherly, 2004; McLaren, 1986) are distinguished from low-angle grain boundaries, which are seen as defects in a single crystal (Poirier, 1985). The energy of the boundary increases with the misorientation and therefore influences the nucleation of new grains (Vernon 2004). Grain boundaries are of significant importance during dislocation processes which involves grain boundary migrations (Barber, 1985).

Shape and crystallographic orientation of grain boundaries reflect the deformation and annealing history of rocks. In particular, Kruhl (2001) and, Kruhl and Peternell (2002) have demonstrated a relationship between the annealing temperature and the *c*-axis orientation of the grains relative to the geometric orientation of the boundary. The bulk of grain boundary research has been undertaken on metals, and to far lesser extent in ceramics (Clarke, 1987; Wolf and Yip, 1992; Sutton and Ballu, 2006), minerals and rocks. Pioneering work was done on quartz and tectonically deformed rocks by White (1977) and White and White (1981). Voll (1960), Kruhl and Peternell (2002), Kuntcheva et al. (2006) and, Liebl et al. (2007) investigated the crystallographic orientation of high-angle grain boundaries in quartz. The traditional optical instrument for measuring *c*-axis orientation and grain boundary geometry is a polarising microscope with universal stage (“u-stage”, von Fedorow, 1891).

In the last two decades, several new instrumental methods have been developed to investigate the 3D structure of grain boundaries, with particular emphasis on metals. One of the most common of these, primarily based on 2D EBSD (electron back-scatter diffraction; Prior et al., 1999), is 3D EBSD (Rollet et al., 2007). To acquire the data needed to reconstruct the 3D structure, the sample is analysed section-by-section, using a focused ion beam. A high resolution is possible, but by the consecutive removal of layers by the ion beam a sample can't be analysed twice (Zaefferer et al., 2008). Mandal et al. (2014) developed a non-destructive 3D method combining two sets of 2D EBSD measurements on specially prepared specimens to acquire the crystallographic properties of grain boundaries. In contrast to the electron beam-based EBSD, a synchrotron X-ray microbeam (DAXM: differential-aperture X-ray microscopy) can be applied to probe the crystal

structure to obtain the grain-boundary normal direction (Larson et al., 2002; Wenge Yang et al., 2004). Furthermore X-ray diffraction contrast tomography (Rolland du Roscoat et al., 2011), as well as neutron tomography (Winkler, 2006), can be used to resolve the 3D grain structure.

Here we present FAGO (Fabric Analyser Grain boundary recONstruction), a new method to determine the 3D grain boundary geometry in birefringent materials such as minerals in rock thin sections. The data sets are acquired using an automated fabric analyser instrument (Fabric Analyser G50, Russell-Head Instruments, Melbourne, Australia; Wilson et al., 2003, 2007; Wilson and Peternell, 2011), a modified polarising microscope with a specific light and filter arrangement (see Section 3.3). The subsequent data processing is highly automated by use of the MATLAB® environment.

3.2. Grain boundary principles

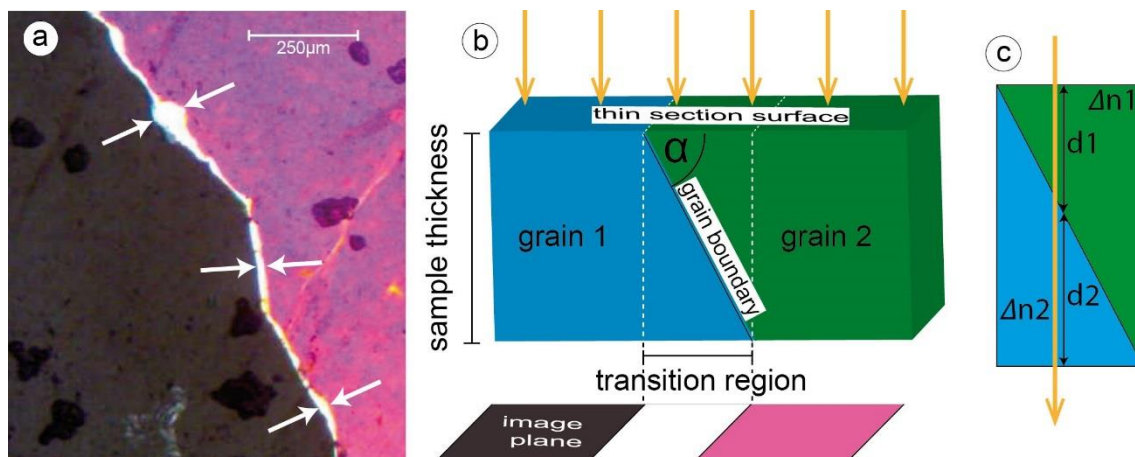


Figure 3.1. Foundations of the FAGO method. (a) Photomicrograph of a grain boundary (arrows) in a 92 μm -thick quartz thin section under crossed polarized light. (b) Simplified model of a straight grain boundary under vertical light (yellow arrows) to indicate the apparent thickness of the grain boundary in the image (Section 3.2), given by the width of the transition region between the two grains. α : Grain boundary dip. (c) Illustration of the distances (d_1 , d_2) traversed by the light in the respective grains to estimate the retardation at the grain boundary. Δn_1 , Δn_2 are the corresponding birefringences.

In the scope of this study grain boundaries in quartz are considered on the scale of optical microscopy ($\sim\mu\text{m}$) as regions separating grains with a misfit of crystallographic orientation of up to $\sim 12^\circ$, depending on the material (Fig. 3.1a). The quartz grain boundary in the 92 μm thick sample is clearly visible as a bright line of varying width (arrows). For this study, we analysed only quartz grain boundaries that consist of a finite number

of straight grain boundary segments with different lengths (Kruhl and Peternell, 2002). Only segments with a minimum length of $\sim 25 \mu\text{m}$ were determined with a microscope resolution of $5 \mu\text{m}/\text{pixel}$. Smaller segments were merged together and a mean orientation was determined. The origin of the characteristic interference colour at the grain boundary can be demonstrated in a simplified model (Fig. 3.1b): In the transition region adjacent to the grain boundary the incident light traverses both grains, resulting in an interference colour that is different from both grains. The apparent thickness of the grain boundary in the image (e.g. under crossed polarisers) depends on the dip α , measured downwards from the thin section horizontal surface. In the cases where the width of the transition region (and the sample thickness) is known, the calculation of α is possible. α is an essential parameter of the grain boundary geometry and will be used for the reconstruction of a 3D grain boundary model (see Section 3.6).

We therefore assume for the 3D reconstruction that the grain boundary is composed of planar segments and therefore no details of the curvature of the grain boundary in the vertical direction are reflected in the reconstruction. Practical observations under the microscope show that the assumption of straight grain boundary segments are justified in most cases, even for a $\sim 150 \mu\text{m}$ thick thin section.

3.3. Instrumentation

3.3.1 Fabric Analyser Instrument

The Fabric Analyser is an automated optical polarising microscope that determines the c -axis orientations of uniaxial materials at each pixel in the field of view with a spatial resolution of $5 \mu\text{m}/\text{pixel}$ (Wilson et al., 2007; Peternell et al. 2009, 2010; Wilson and Peternell, 2011). In addition to c -axis orientation maps retardation images are generated. A retardation image shows the highest birefringence colour at each pixel, dependent on the light direction, sample thickness and analysed material (Peternell et al., 2009). The Fabric Analyser G50 and new G60 series are the only available optical fabric analyser microscopes, which can be used for the 3D grain boundary determination, and here we present results from a G50 instrument.

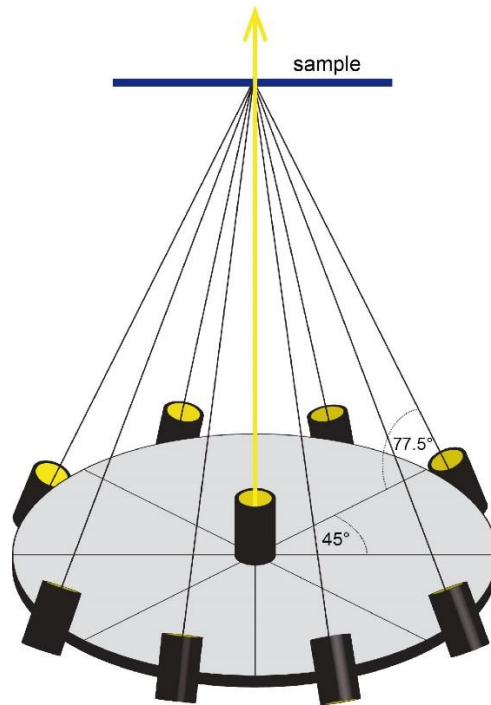


Figure 3.2. Arrangement of the eight inclined and one vertical light sources in the fabric analyser.

The G50 uses an arrangement of nine white high-power LEDs as light sources (Fig. 3.2). The one in the centre is oriented perpendicular to the thin section plane, and the others are equally distributed and inclined 77.5° to the thin section plane. Based on this arrangement of light sources retardations were recorded from nine different directions. Due to the enhanced contrast and its physical significance FAGO uses retardation data instead of simple crossed polar images. The Fabric Analyser acquisition software was modified to enable the recording of retardation images from the individual light sources.

3.3.2 Polarising microscope and universal stage

The universal stage allows the manual rotation and tilting of thin section samples under an optical microscope, and therefore enables in addition to the measurement of the crystallographic c -axis the determination of the grain boundary dip angle in standard thick sections ($\sim 30 \mu\text{m}$) with an accuracy of $\pm 2^\circ$ (Kruhl and Peternell, 2002). With an increased thickness of the samples an increased accuracy is expected for perfectly planar grain boundaries. Nevertheless, in practice grain boundaries are often curved, rough or open, which increases the accuracy in case of our thicker samples ($92 \mu\text{m}$, $144 \mu\text{m}$) to $\pm 6^\circ$ for angles $\geq 70^\circ$ and $\pm 7^\circ$ for $\leq 70^\circ$ on average. Due to the construction of the u-stage, measuring grain boundary dips of $\leq 30^\circ$ is not possible.

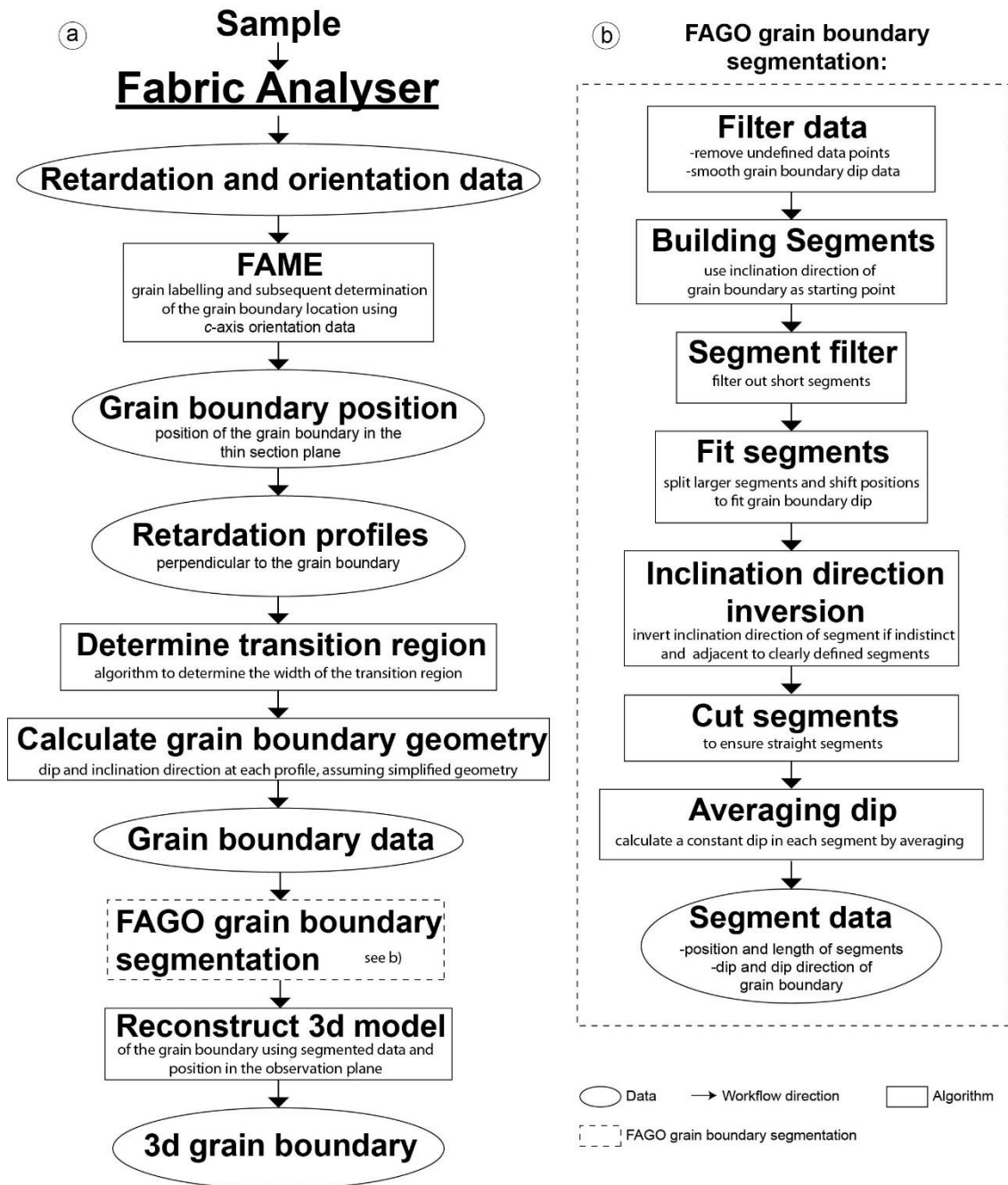


Figure 3.3. Workflow of FAGO 3D grain boundary analysis (a) and the grain boundary segmentation part considered in detail (b). The FAME software (Hammes and Peternell, 2016) is used for determination of the grain boundary location.

In this study, a Leitz (Wetzlar, Germany) polarising microscope with 5x magnification objective and an attached Leitz UT4 universal stage was used. A Leitz DMRP polarising microscope was applied in addition for general observations and for taking photomicrographs using a CMOS camera.

3.4. FAGO grain boundary analysis

In figure 3.3 the simplified workflow of FAGO is shown. The retardation data acquired by the Fabric Analyser is used to determine dip variations along a grain boundary. The dip data is divided into so called “FAGO segments”. The results are finally used to reconstruct a 3D model of the grain boundary.

3.4.1. Retardation

Determination of grain boundary geometry in FAGO is mainly based on measuring and analysing the retardation. In the optical mineralogy of rocks the retardation Γ is defined as

$$\Gamma = d \cdot \Delta n, \quad (3.1)$$

where d is the traversed path distance in the crystal and Δn the birefringence (Kerr, 1977, p. 92). The actual birefringence not only depends on the birefringence of the material, but also on the crystallographic orientation relative to the light source.

Assuming a linear superposition, the retardation of light passing through the boundary between two grains 1 and 2 can be approximated by the linear relationship:

$$\Gamma = d_1 \Delta n_1 + d_2 \Delta n_2, \quad (3.2)$$

where d_1 , d_2 are the distances traversed in the respective grains and Δn_1 , Δn_2 the corresponding birefringence. However, thin amorphous films may occur along grain boundaries (Wirth 1996), or they may be open on the nm-scale (Kruhl et al., 2013), which can lead to light scattering. Therefore, equation (3.2) is a first simplified model to simulate an ideal two-crystal system (Fig. 3.1b) with a straight and planar grain boundary (Fig. 3.4a). In this idealised case the retardation is assumed to be linear (equation 3.2) in the transition region near the grain boundary and constant otherwise.

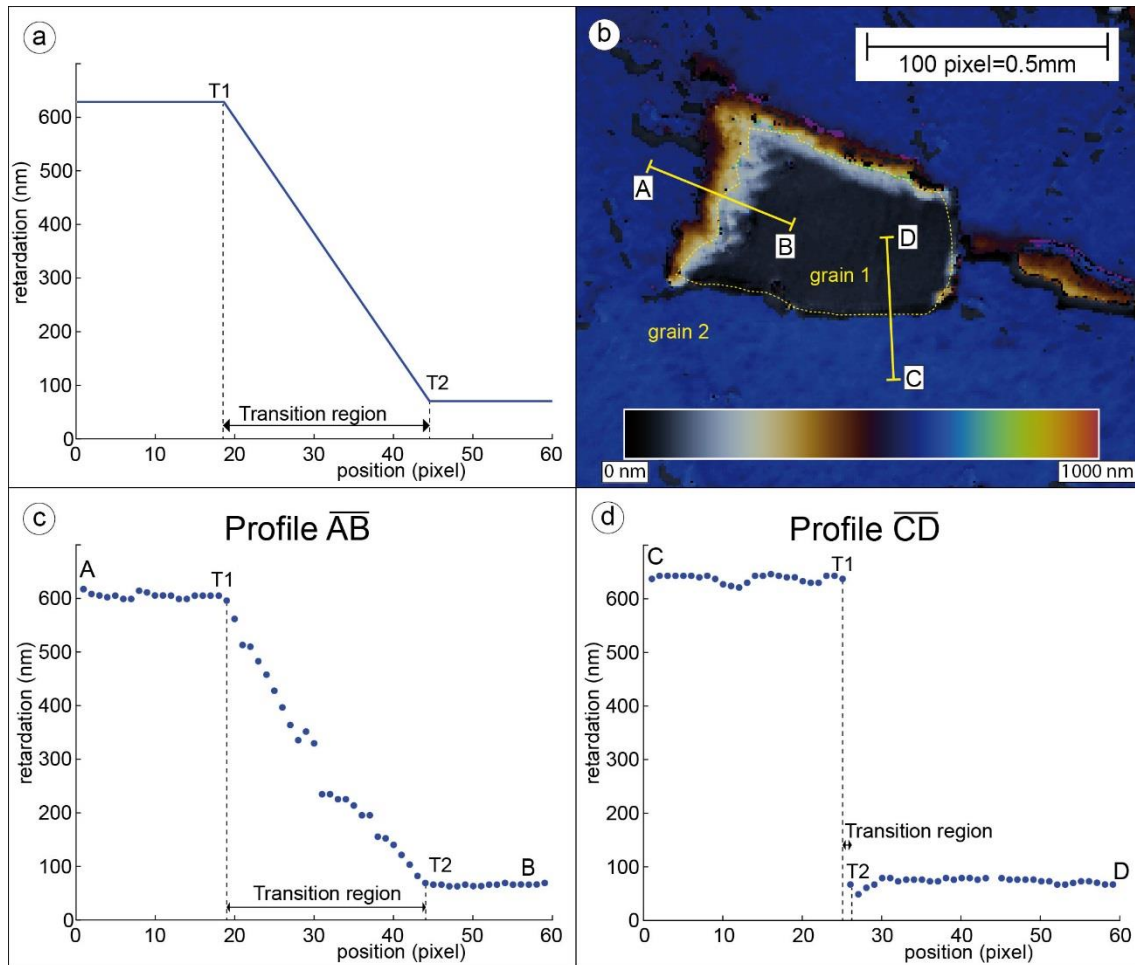


Figure 3.4. Retardation profiles and illustration of the transition region. (a) Theoretical retardation profile. Retardation image of quartz grains (b) and retardation profiles across lines \overline{AB} (c) and \overline{CD} (d). The grain boundary dip is $34^\circ \pm 4^\circ$ at \overline{AB} and $88^\circ \pm 2^\circ$ at \overline{CD} . T1, T2 indicate start- and endpoint of the transition region. Sample thickness = $92 \mu\text{m}$. Colour bar represents interference colour and related retardation.

3.4.2. Fabric Analyser retardation profiles

Retardation profiles recorded by the Fabric Analyser are the key element of FAGO. Figure 3.4b shows the retardation image of quartz grain 1 surrounded by quartz grain 2. Two retardation profiles were drawn across the grain boundary (Fig. 3.4c, d). The fringe structure near profile \overline{AB} represents an inclined grain boundary segment with a dip of $34^\circ \pm 4^\circ$, as verified by the universal stage. The retardation profile of the ideal two-crystal system (Fig. 3.4a) is modelled according to the general form of linear retardation profiles such as along \overline{AB} (Fig. 3.4c): Constant inside the grains and nearly linear in the transition region. In contrast, the retardation profile along \overline{CD} (Fig. 3.4d) can be approximated by a step function without a clear transition zone. No fringe structure, as along \overline{AB} , can be recognised in the retardation image near \overline{CD} as only a faint black line. This is typical for

an almost vertical grain boundary (dip: $88 \pm 2^\circ$) and in accordance with the ideal two-crystal system. Based on these observations a relationship between the width of the transition region and the grain boundary dip is to be expected.

3.4.3. Defining the width of the transition region

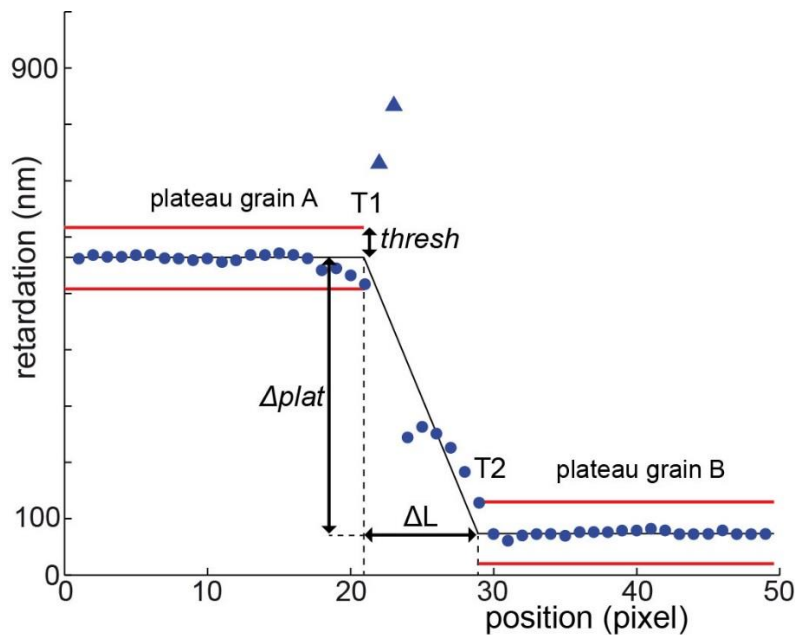


Figure 3.5. Example of retardation profile to demonstrate how the width ΔL of the transition region is determined. Start- (T1) and endpoint (T2) of ΔL are defined by a threshold ('thresh'; red lines). Circles represent retardation measurements and outliers are indicated by triangles. $\Delta plat$ is the retardation difference between the two plateaus. The idealized profile is traced by the solid black lines.

Knowing the ΔL width of transition region (Fig. 3.5) is necessary for determining the grain boundary dip α . In contrast to the theoretical retardation profile (Fig. 3.4a), the transition region is less clearly defined in Fabric Analyser recorded profiles (Fig. 3.4c, d). Ideally, the retardation is constant within each grain and therefore in each plateau (Fig. 3.5). Impurities in the material and other deficiencies lead to outliers in the profiles (triangles in Fig. 3.5). Filtering of the retardation data is therefore necessary to ensure a correct identification of the transition region.

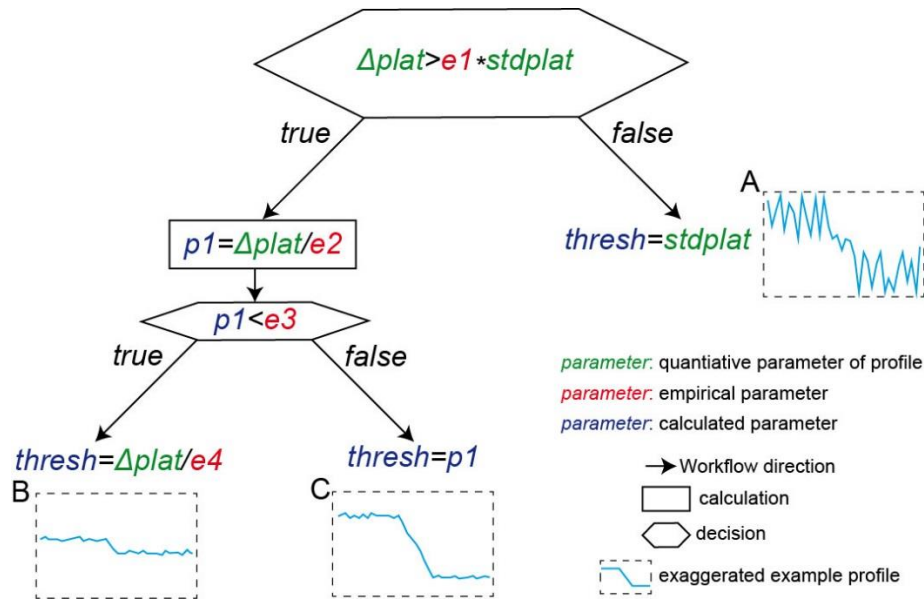


Figure 3.6. Workflow of algorithm to define threshold (*thresh*) for the determination of the transition region width from figure 5. $\Delta plat$ is the retardation difference between the two plateaus and $stdplat$ the standard deviation of the retardation in the plateaus. The parameters $e1-4$ are further explained in the text. Example profiles with exaggerated features for demonstrating the specific cases are shown in boxes A-C.

The start (and end) point T1 and T2, respectively of the transition region is defined as the position where the retardation data leaves a defined threshold (*thresh*) around the plateaus. The determination of an appropriate value for *thresh* is therefore essential for the measurement of the transition region width (Fig. 3.6). If the difference between the plateaus ($\Delta plat$) is smaller than the product of the standard deviation of the retardation in the plateau regions ($stdplat$) with an empirical parameter ($e1$), the standard deviation is used as a threshold (example profile in box A: Fig. 3.6). In the case of profiles with small retardation variations a criteria $p1$ is defined, using a second empirical parameter ($e2$). If $p1$ is smaller than a given parameter ($e3$), the threshold is set to $p1$ (example profile shown in box C). In the opposite case of profiles with close plateaus (box B), *thresh* is defined based on another empirical parameter ($e4$). The parameters $e1-e4$ are defined empirically by comparing FAGO measurements using different combinations of the parameter with u-stage reference measurements. For the sets of grain boundaries in 20 μm -, 92 μm - and 144 μm -thick sample sections as discussed in Section 3.5 the dip was determined with FAGO using a few hundred combinations of parameters and the deviation to the u-stage measurements calculated. The parameter combination with the smallest deviation was chosen and with a second and third run of the scheme more precisely defined. The parameter combination $e1=10$, $e2=10$, $e3=5$ and $e4=4$ resulted in the smallest deviations for the considered samples and were used throughout this publication. A slightly different

parameter combination might result in slightly better results for one sample thickness, but the stated combination gave in general the best overall results. Based on the results of the three sample sections and the fact that the retardation profiles are expected to have a similar form it is likely that the stated parameter combination can also be applied to different sample thicknesses and other materials besides quartz.

3.4.4. Transition region width and grain boundary orientation

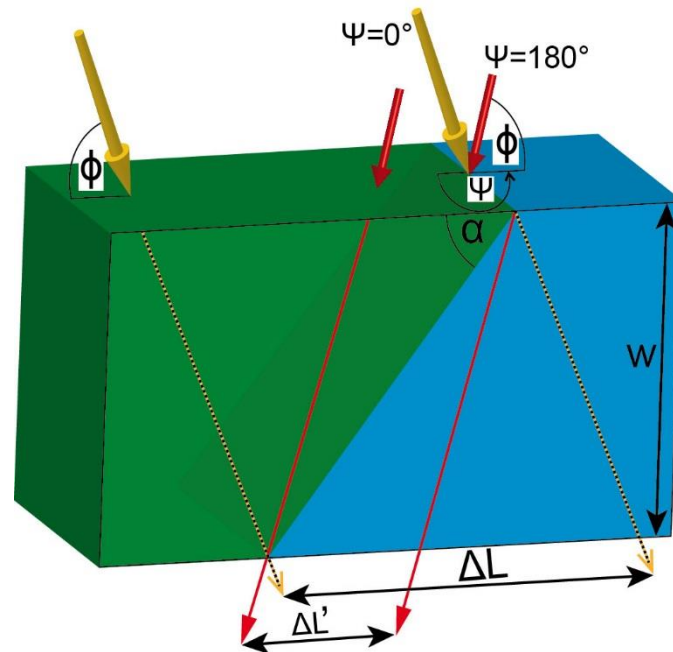


Figure 3.7. Simplified sketch to illustrate the geometric relation between the grain boundary in thin section for two different light direction azimuth $\psi=0^\circ$ (yellow arrows) and $\psi=180^\circ$ (red arrows). w : thin section thickness; ΔL , $\Delta L'$: width of transition region for the two different light directions (yellow, red arrows); α : grain boundary dip; Φ : light direction dip angle.

A simplified grain boundary geometry (Fig. 3.7) is assumed for deriving a quantitative relationship between the width of the transition region (ΔL) and the dip of the grain boundary (α). It follows for light sources oriented at a dip angle Φ and an azimuth angle (ψ) relative to the grain boundary:

$$\Delta L/w = |1/\tan(\alpha) + \cos(\psi)/\tan(\Phi)|, \quad (3.3)$$

Where w is the sample thickness. In the case of the Fabric Analyser Φ is 90° (vertical LED) or 77.5° (inclined LEDs).

Using equation (3.3), the grain boundary dip can be determined using the transition region width for each of the nine light directions and an average is calculated. In the averaging process angles with large deviations from the median (e.g. $>30^\circ$) are excluded.

Considering the model in figure 3.7), the transition region width is expected to be smaller for a light source tilted in the direction of the grain boundary inclination (ΔL ; $\psi=180^\circ$) than in the opposite direction (ΔL ; $\psi=0^\circ$). Comparing the transition region widths for all nine light directions allows to determine the inclination direction, which describes whether the grain boundary is inclined toward the right- or left side relative to the grain boundary. The inclination direction is not identical to the dip direction, which is measured in degrees (0-360°) instead of “left” or “right”.

3.4.5. FAGO grain boundary segmentation

To acquire the dip of a grain boundary (for example between grains 1 and 2 in Fig. 3.8a), its position in the thin section is necessary. Manual placement of the retardation profiles across the trace of the grain boundary, in the 2D thin section, is possible but time intensive. Instead the FAME software (Paternell et al., 2014; Hammes and Paternell, 2016) is applied on the *c*-axis orientation data (Fig. 3.8b) to produce a labelled grain map (Fig. 3.8c) and consequently the position of the grain boundary trace (dashed line in Fig. 3.8b). Each profile line is perpendicular to the grain boundary (yellow profile lines in Fig. 3.8c) and the maximum extent of the individual profiles is restricted by the proximity of other grain boundaries. FAGO optionally supports an automatic determination of the profile length by recognizing characteristic variations in the retardation along the profile direction.

Microscopic investigations using a universal stage have shown that quartz grain boundaries are mostly divided into several straight segments (Kruhl, 2001; Kruhl and Paternell, 2002). Similar observations are also reported from other materials (Wolf and Yip, 1992). The assumption of a grain boundary divided into segments with approximately constant dip also facilitates the reconstruction of a 3D model. The box in figure 3.3 visualises the steps in building of FAGO grain boundary segments using the dip data. Before single measurements are merged into a FAGO segment, the dip and inclination direction data is filtered from undefined data points (inclination direction = N; Fig. 3.8d-

f) and outliers (“x” in Fig. 3.8d). Undefined data results from complicated retardation profiles where a determination of the transition region width is not possible.

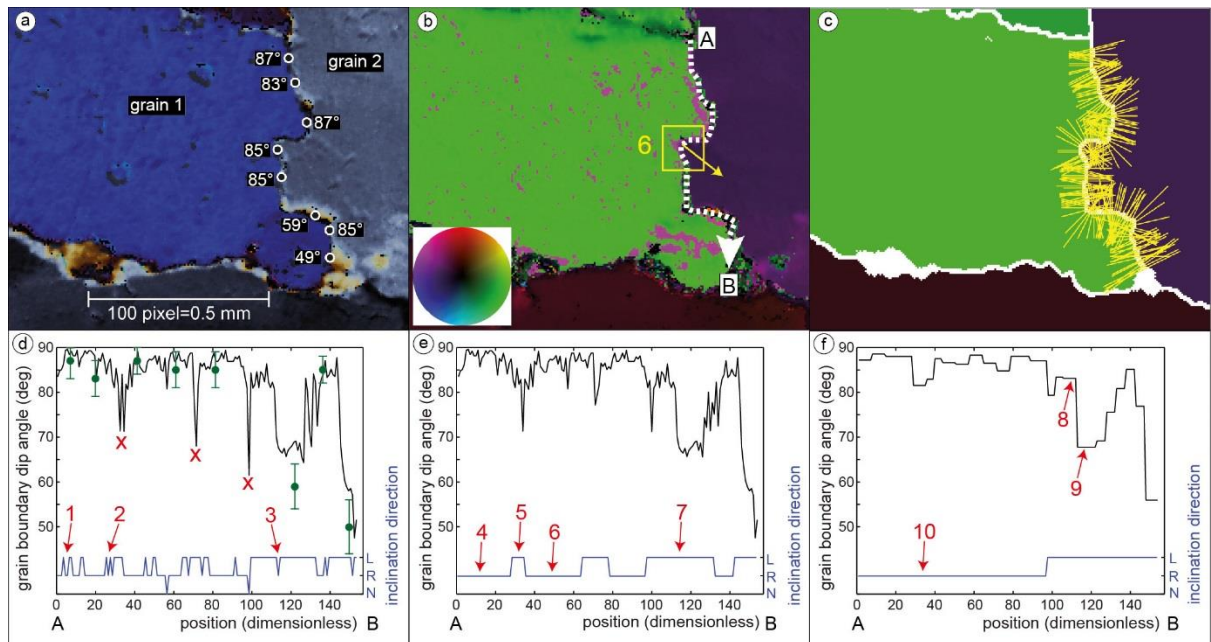


Figure 3.8. Acquiring grain boundary dip and inclination direction from fabric analyser data. Retardation image (a), *c*-axis orientation image (b) and FAME labelled grain map (c) of a 92 μm quartzite thin section. Colour wheel indicates *c*-axis orientation in b) and c). Broken line \overline{AB} in b) represents the position of the grain boundary from FAME and lines in c) the retardation profile lines. Variation of dip- and inclination directions along the grain boundary before segmentation (c), after splitting of larger segments (d; “fit segments” in fig. 3.3) and after completed segmentation process (e). R: grain boundary inclined towards right side in direction of A->B (arrow in b); L: opposite direction; N: no determination possible. Grain boundary dip measurements with universal stage are indicated by points in a) and with error bars in d) for comparison. Crosses mark stray points in the dip measurements. Numbers identify grain boundary parts (further discussed in the text) to illustrate the segmentation process. The yellow arrow marks the mean strike of the profiles in segment 6. The data points in d)-f) are connected by lines for better visualisation.

The initial state for building the FAGO segments is based on the inclination direction: Every coherent part of the grain boundary with coincident inclination direction represents a FAGO segment (e.g. inclination direction curve in Fig. 3.8d). Short FAGO segments (≤ 4 data points) are filtered out by combination with longer neighbouring segments. This is demonstrated on the single point segment 3 in Fig. 3.8d), which becomes part of a larger segment (7 in Fig. 3.8e). In addition to the inclination direction, the dip is used for further refinement of the FAGO segments (Fig. 3.3, “Fit segments”). If a single FAGO segment consists of two parts with similar angles in each part, but a considerable angle

difference ($>8^\circ$) between the parts, the segment is divided. In this way, FAGO distinguishes segments with the same inclination direction, e.g. “left-left” or “right-right”, but with different dip (e.g. segments 8, 9 in Fig. 3.8f). Afterwards the start- and end points of the segments are shifted ≤ 4 pixel in both directions to avoid corner effects and to further increase the correlation between the segments and the dip data. For the case where a FAGO segment with indistinct inclination direction is neighbouring two segments with different but clearly defined directions, the inclination direction of the middle segment is inverted (Fig. 3.3, “Inclination direction inversion”). For example, segment 5 is neighbouring two segments (4, 6) and its unprocessed data (2 in Fig. 3.8d) shows a less clearly defined direction (i.e. more variations in the inclination direction) than segments 4 and 6. Segment 5 therefore inverts its direction (10 in Fig. 3.8f).

The previous steps of the grain boundary segmentation can lead to “curved” grain boundaries (e.g. segment 6 in Fig. 3.8b, e), which have no equivalent in nature and are in contradiction to the observations of Kruhl and Peternell (2002) where quartz grain boundaries consist of a set of shorter and longer straight segments. Therefore, such curved segments are iteratively partitioned based on the strike of the profiles (yellow lines in Fig. 3.8c). A curved segment is subdivided into two equal-length parts if four or more profiles deviate by at least 11.25° ($=360/32$) from the mean strike of the segment (e.g. yellow arrow in Fig. 3.8b). During this process (Fig. 3.3; “cut segments”) a minimum segment length of four data points needs to be ensured.

Finally, the dip is calculated in each FAGO segment and the value assigned to every data point in the segment (“Averaging dip”; Figs. 3.3, 3.8f). The dip and inclination direction for each grain boundary segment determined with FAGO enables a three dimensional visualisation of a complete grain boundary. Two examples of 3D grain boundary models generated with FAGO are discussed in Section 3.6.

3.5. Verification of grain boundary segment orientation

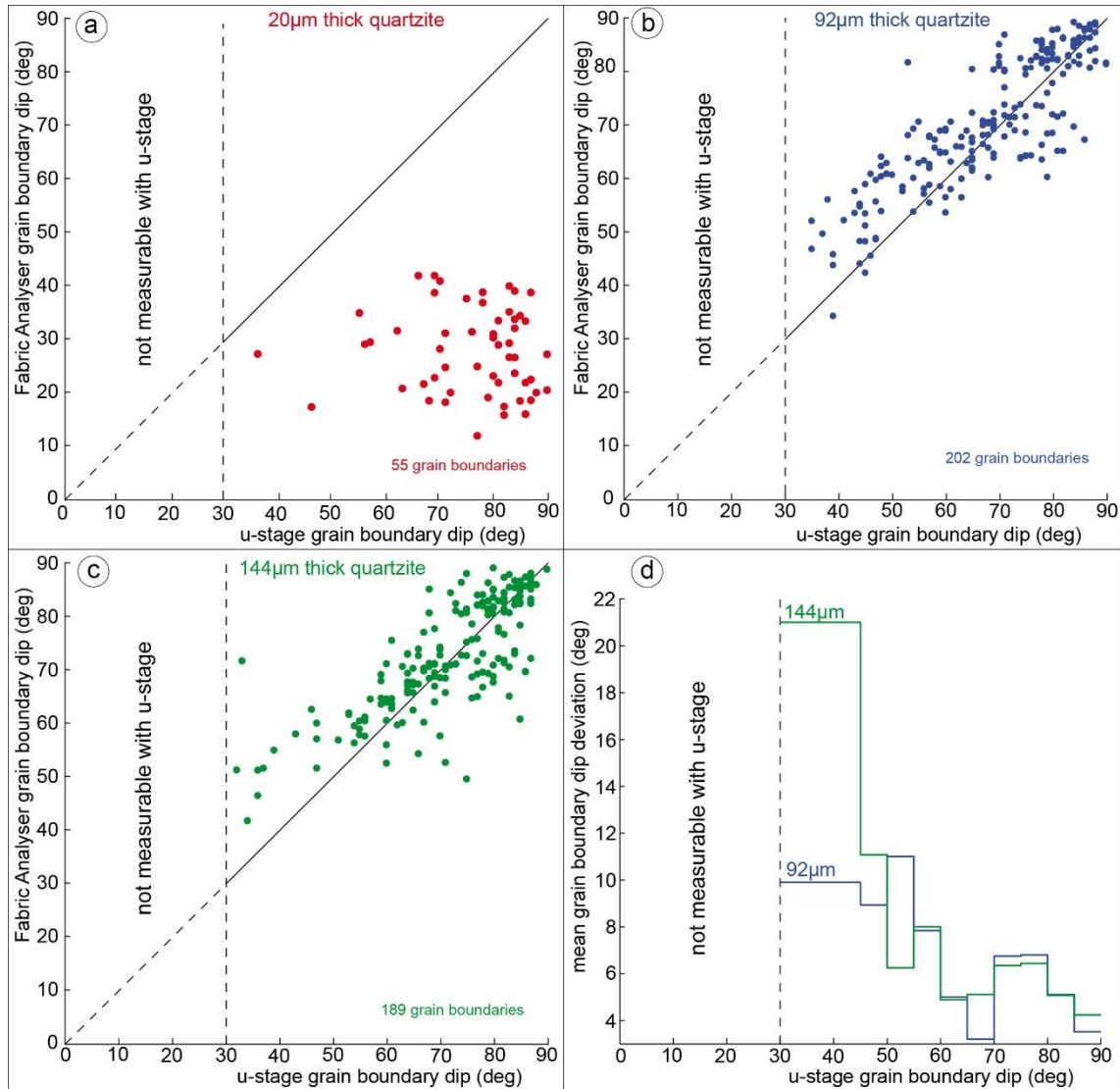


Figure 3.9. Grain boundary segment dip measured with FAGO compared with reference measurements using a microscope with universal stage attached. The profile length was determined manually. Data from quartzite samples with 20 μm (a), 92 μm (b) and 144 μm (c) thickness. (d) Mean grain boundary dip difference between FAGO and u-stage (*see text*) for the 92 μm and 144 μm samples.

To establish the applicability of equation 3.3 and the retardation profile analysis algorithm (Section 3.4.3) reference measurements with a universal stage were performed. Three quartzite thin section samples with different thicknesses of 20 μm , 92 μm and 144 μm were scanned. We have chosen a 20 μm thick thin section, which is close to a typical sample thickness of 25-30 μm , in order to evaluate the minimum thickness of a quartz bearing section that can be used with our method. A mechanical micrometre (accuracy: $\pm 1 \mu\text{m}$) was used for the measurement of the section thicknesses. The estimated thickness

inaccuracy of $\pm 3 \mu\text{m}$ is mainly based on variations in the thickness of the sample. In each sample a number (20 μm : 64, 92 μm : 204, 144 μm : 195) of well-defined grain boundary segments (i.e. no larger inclusions) were measured with the universal stage (Table 3.1). Profile lengths for each FAGO generated retardation profile were manually and automatically determined and only grain boundaries with a minimum length of 45 μm ($\cong 9$ pixels) have been analysed. All nine light directions and on average eight, but at least three, data points per grain boundary segment were used. The dip for each grain segment was calculated using the profile analysis algorithm (Section 3.4.3) and equation 3.3. The results are summarised in Figure 3.9 and Table 3.1.

Sample thickness	20 μm		92 μm		144 μm	
	Manual	Automatic	Manual	Automatic	Manual	Automatic
Profile length determination						
Number of analysed grain boundary segments	64	64	204	204	195	195
Determination not possible (number of segments)	9	14	2	3	6	9
Mean dip difference to u-stage (deg)	48.7 $^{\circ}\pm 11.1^{\circ}$	52.8 $^{\circ}\pm 10.2^{\circ}$	6.1 $^{\circ}\pm 4.0^{\circ}$	7.1 $^{\circ}\pm 4.6^{\circ}$	5.9 $^{\circ}\pm 4.2^{\circ}$	7.5 $^{\circ}\pm 5.8^{\circ}$

Table 3.1. Results of FAGO grain boundary dip determination for single segments compared with u-stage reference measurements. The confidence interval of the mean dip difference was estimated using the median absolute deviation (MAD). Their magnitude is obtained by the number of outliers.

Dip measurements from the 20 μm thick sample are grossly underestimated and different to the u-stage reference (Fig. 3.9a). This discordance is most likely effected by the small thickness of the sample. The retardation decreases with decreasing sample thickness (equation 3.1) and therefore the absolute retardation between neighbouring grains. This leads to a decreased plateau difference in the retardation profiles and can cause an inaccurate determination of the transition region (Section 3.4.2). We suggest that with the recent Fabric Analyser G50 thin ($\lesssim 20 \mu\text{m}$) and regular thick thin sections (25-30 μm thick) are not usable for the 3D grain boundary orientation analysis of quartz.

In contrast to the 20 μm section, the FAGO dip values of the 92 μm and 144 μm samples are in good correlation with the corresponding universal stage measurements (Fig. 3.9b, c). Some of the outliers can be traced back to tiny inclusions or other defects in or near the grain boundaries, which in turn may lead to a failure in the determination of the transition region width. Another reason for larger deviations, in particular in the 92 μm

sample, is a very small ($\lesssim 100$ nm) difference in retardation between two neighbouring grains and similar to the 20 μm sample. In general, the determination of the dip becomes more accurate between grains with large differences in the retardation values.

To obtain an angle dependent estimate of the dip measurement accuracy, the angle data of the 92 μm and 144 μm samples was partitioned in intervals with a width of 5° ; angles $<45^\circ$ were grouped together in one interval. For each interval i a mean difference from the reference $\Delta\alpha_{-}(i)$ was calculated:

$$\Delta\alpha_{-}(i) = \frac{1}{n} \sum_{j=1}^n |\alpha_{j,FA} - \alpha_{j,ref}|, \quad (3.4)$$

Where $\alpha_{j,FA}$ is the Fabric Analyser determined angle and $\alpha_{j,ref}$ the corresponding universal stage recorded value; n is the number of angle measurements in each interval. $\Delta\alpha_{-}(i)$ can be used as an estimate of the accuracy of the dip measurement. For angles $>45^\circ$, the mean dip differences are in good agreement for the 92 μm and the 144 μm thick sections (Fig. 3.9d). The length of the grain boundary and therefore the segmentation in the thin section surface increases with the thickness of the section and a decreasing dip. In case of fractured and curved grain boundaries the assumption of a planar grain boundary segment is therefore increasingly violated by an increased sample width. This would lead to a higher inaccuracy expected for the 144 μm section. However, this effect is offset for angles $>50^\circ$ by the increased accuracy due to an enlarged transition region width, which is equivalent to a higher resolution. The rise of the mean dip difference with decreasing angle (Fig. 3.9d), in particular for the 144 μm section, can be explained by two reasons: (I) the increase of the transition region width: The steepness of the transition region decreases and the definition of a start- and end point (T1, T2 in Fig. 3.4c, d) may become inconclusive. This in general leads to an underestimated transition region width and therefore to an overestimated dip. (II) Larger dip values increase the inaccuracy of the universal stage and therefore artificially cause a larger deviation of the dip in figure 3.9 and table 3.1. On the other hand, angles smaller 30° can only be measured with the Fabric Analyser, a great advantage over the classical u-stage measurement technique.

In contrast to the good dip accuracy the success rate for the inclination direction determination is low with $\sim 60\%$ in case of the 92 μm and 144 μm samples. However, the analysis of single grain boundary segments does not take into account the orientation of neighbouring segments, used by FAGO (Section 3.4.5). Therefore, to tap the full potential

of FAGO at least larger parts of a grain boundary or the whole boundary should be analysed.

3.6. 3D grain boundary reconstruction

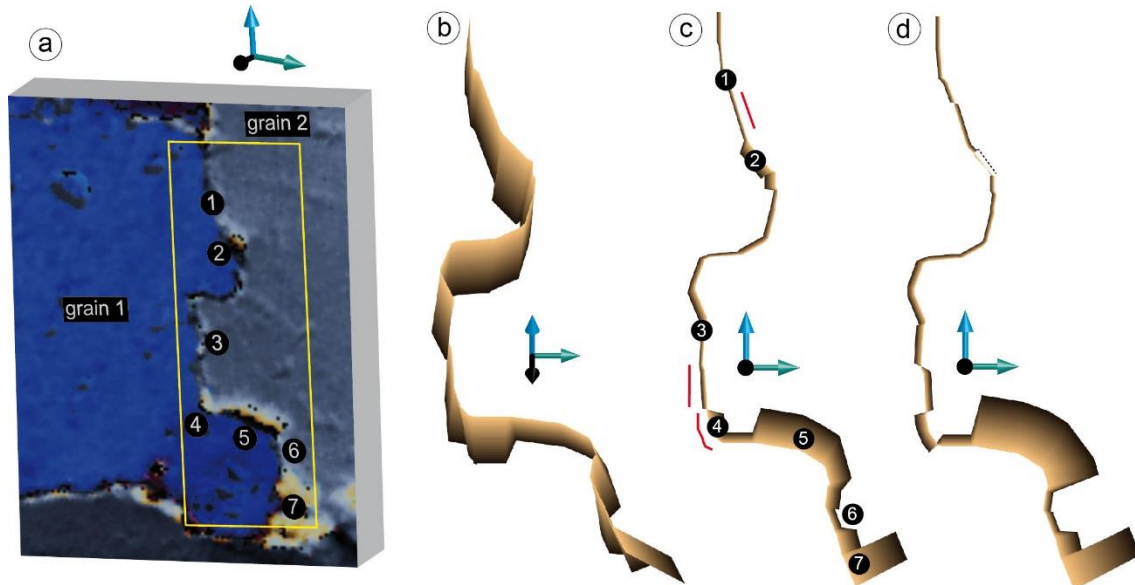


Figure 3.10. 3D reconstruction of a grain boundary in a 92 μm -thick quartzite sample. (a) Retardation image with highlighted grain boundary (rectangle). (b) Tilted view of FAGO-reconstructed 3D grain boundary. (c) FAGO and (d) u-stage grain boundary models viewed from the top. Black arrows indicate direction normal to thin section surface. Bottoms of the 3D reconstructions are coloured in black. Numbers indicate specific regions of the grain boundary (see Section 3.6). Grain boundary parts marked with red lines in c) show a different inclination direction compared to the u-stage reference d). Dotted lines in c) mark a region where no proper reconstruction based on u-stage measurements is possible.

The determination of dip and inclination direction for each FAGO grain boundary segment, enables a three dimensional visualisation of a complete grain boundary. Based on the assumptions of straight and segmented grain boundaries, the reconstructed model is composed of geometric planes. In Figure 3.10b and c a FAGO modelled grain boundary from Section 3.4.5 (Fig. 3.8) is visualised and viewed from two different perspectives. The grain boundary is composed of almost vertical (1, 3, 6 in Fig. 3.10a, c), moderately inclined (4) and highly inclined (5, 7) parts. The lower part (3-6) is in general inclined towards grain 1. Figure 3.10d shows a grain boundary model with the segments measured by the universal stage for comparison. At location 2 the grain boundary shows a small bulge which can't be represented properly in the u-stage model and also impedes a proper

FAGO analysis. Comparison with u-stage measurements (Fig. 3.10d) shows that the inclination direction agree in 17 out of 22 (77%) FAGO segments (Fig 10c; mismatching sections indicated with red lines). The mean difference between the FAGO model and the u-stage measured segments is $2.9^\circ \pm 2.8^\circ$.

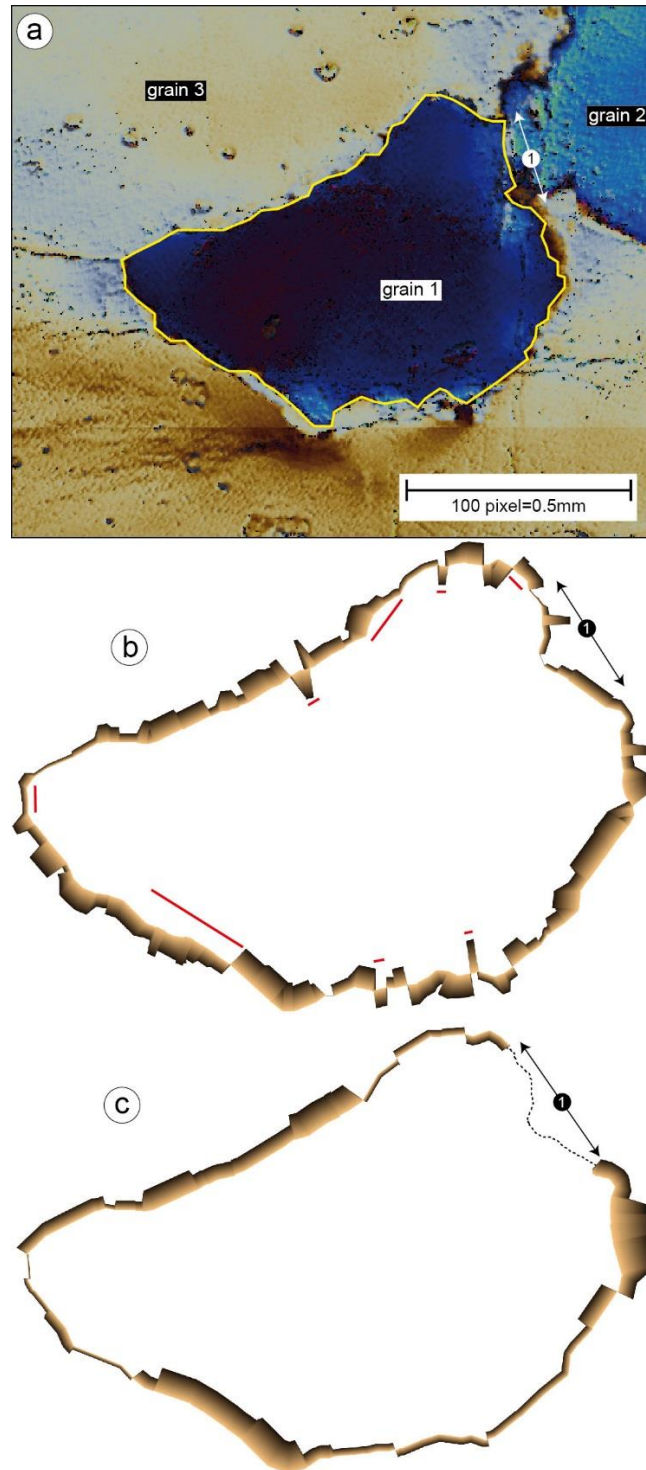


Figure 3.11. Estimated average retardation difference (nm) between two grains for different materials and sample thicknesses; equal distribution of orientations assumed. Birefringences by Tröger (1982).

Figure 3.11 illustrates as a second example the complete grain boundary around a grain in the 144 μm section. The data was processed automatically as in the first example, a manual input was only necessary for the FAME grain labelling and the selection of the particular grain. Grains 1 and 2 are separated only by a subgrain boundary and in addition, fractures occur in this region (1 in Fig 3.11b). No u-stage reconstruction (Fig 3.11c) was therefore possible at this part. The inclination direction agrees for 75 out of 105 (71%) FAGO segments. For this particular example the deviation of the FAGO model from u-stage measure is $8.1^\circ \pm 4.5^\circ$ on average.

By considering the magnitude of the confidence intervals, the dip accuracies of the 3D models are in the same range as the single segments (Section 3.5, Table 3.1). The inclination direction-determination match between FAGO and u-stage measurements increases by ~10-17% by taking the relations between neighbouring segments during the FAGO segmentation process (Fig. 3.3) into account, in contrast to analysing the segments individually (Table 3.1). The improvement can be explained by the fact that neighbouring segments are connected and influence each other, and often share the same inclination direction.

3.7. Application on other materials

The applicability of FAGO was solely demonstrated using quartz samples due to its abundant occurrence as a rock-forming mineral (Deer et al., 1966, p. 340). In fact any other birefringent material could be used if it has an appropriate sample thickness. As demonstrated in the 20 μm quartz sample, a significant retardation difference between the examined grains is necessary to ensure a suitable determination of the grain boundary dip. To evaluate a suitable sample thickness for a specific material, the average retardation difference between two grains (equal distribution of orientations assumed) was estimated for different materials (Table 3.2). Quartz samples with a thickness of 92 μm and 144 μm give satisfactory results, and therefore samples with a similar average retardation difference (~340-530 nm) will lead to similar good results. In case of orthoclase the sample thickness should be ~200 μm and for olivine ~50 μm . A thickness of ~600 μm is necessary in the case of ice.

Material	Retardation difference (nm)				
	20µm sample	50µm sample	92µm sample	144µm sample	200µm sample
Quartz	74	180	340	530	740
Orthoclase	33	83	150	240	330
Olivine (Forsterite)	200	500	930	1400	2000
Pyroxene (Augite)	550	1400	2500	4000	5500
Calcite	1400	3500	5400	10000	14000
Ice	11	28	52	82	110

Table 3.2. Estimated average retardation difference (nm) between two grains for different materials and sample thicknesses; equal distribution of orientations assumed. Birefringences by Tröger (1982).

3.8. Discussion

In contrast to manual u-stage measurements, analysing the 3D grain boundary geometry with FAGO is fast and almost fully automatized and therefore requires only minor input by the user. The dip measurement is not restricted to angles $<45^\circ$ and FAGO offers the generation of 3D grain boundary models for visualisation. With the recent Fabric Analyser resolution, minimum grain boundary length is limited to $\sim 25 \mu\text{m}$. Hardware changes in the Fabric Analyser light arrangements, in particular more tilted ($<77.5^\circ$) outer light sources (Fig. 3.2) will lead to an improved determination of the grain boundary dip and inclination direction. FAGO assumes planar grain boundaries and provides no information about the irregularities of grain boundaries in the depth. By using optical light, FAGO is non-destructive and does not require any special sample preparation as in 3D EBSD. In case of quartz, a 92 μm thick sample was successfully analysed and the lower limit of sample thickness and related minimum grain sizes are between 20-92 μm , but need to be more accurately determined in future studies.

3D EBSD is able to analyse grain boundaries in the depth with high accuracy, but the instrumentation required by FAGO is significantly less elaborate and complete thin sections can be scanned in <1 h. FAGO can then be applied to the data using any regular Windows® based computer.

3.9. Conclusion

FAGO is a new method to determine grain boundary geometry in birefringent materials by evaluating retardation data recorded with the Fabric Analyser system. Its applicability and usefulness is demonstrated on quartz thin sections. First results indicate the potential of this method for an automatic 3D reconstruction of grain boundaries of any translucent mineral from 2D rock thin sections. The determination of the inclination direction leads to good results in the case of single segments, and the accuracy is significantly improved by considering neighbouring grain boundary-segment relationships.

Grain boundary analysis with FAGO is very fast and almost fully automatized, and 3D grain boundary models from single crystals can be generated for any grain inside the sample. The described method opens a new field for grain boundary investigation. FAGO-based investigation is a first step towards a better understanding how rock grain boundaries of different mineral assemblages evolve during changing temperature and pressure conditions, and vice versa, how the grain boundaries control the evolving rock microstructure.

References

- Barber, D.J., 1985. Dislocations and microstructures. *Preferred Orientation in Deformed Metals and Rocks: An Introduction to Modern Texture Analysis* (ed. by H.-R. Wenk), pp. 149-182. Academic Press, Orlando.
- Clarke, D.R., 1987. Grain boundaries in polycrystalline ceramics. *Annual Review of Materials Research* 17, 57-74.
- Deer, W.A., Howie, R.A., Zussman, J., 1966. *An introduction to the rock-forming minerals*. Longman, London.
- Fedorow, E.v, 1891. Eine neue Methode der optischen Untersuchung von Krystallplatten in parallelem Lichte. *Tschermak's Mineralogische und Petrographische Mitteilungen* 12, 505-509.
- Hammes, D.M., Peternell, M., 2016. FAME: Software for analysing rock microstructures. *Computers & Geosciences* 90, 24-33.
- Humphreys, F.J., Hatherly, M., 2004. *Recrystallization and related annealing Phenomena*. 2nd edition, Elsevier, Amsterdam.
- Kerr, P.F., 1977. *Optical Mineralogy*. 4th edition, McGraw-Hill, New York.

- Kruhl, J.H., 2001. Crystallographic control on the development of foam textures in quartz, plagioclase and analogue material. *International Journal of Earth Science* 90, 104-117.
- Kruhl, J.H., Peternell, M., 2002. The equilibration of high-angle grain boundaries in dynamically recrystallized quartz: the effect of crystallography and temperature. *Journal of Structural Geology* 24, 1125-1137.
- Kruhl, J.H., Wirth, R., Morales, L.F.G., 2013. Quartz grain boundaries as fluid pathways in metamorphic rocks. *Journal of Geophysical Research: Solid Earth* 118. 1-11.
- Kuntcheva, B., Kruhl, J.H., Kunze, K., 2006. Crystallographic orientation of high-angle grain boundaries in dynamically recrystallized quartz: First results. *Tectonophysics* 421, 331-346.
- Larson, B.C., Wenge Yang, Ice, G.E., Budai, J.D., Tischler, J.Z., 2002. Three-dimensional X-ray structural microscopy with submicrometre resolution. *Nature* 415, 887-890.
- Liebl, C., Kuntcheva, B., Kruhl, J.H., Kunze, K., 2007. Crystallographic orientations of quartz grain-boundary segments formed during dynamic recrystallization and subsequent annealing. *European Journal of Mineralogy* 19/5, 735-744.
- Mandal, S., Pradeep, K.G., Zaefferer, S., Raabe, D., 2014 A novel approach to measure grain boundary segregation in bulk polycrystalline materials in dependence of the grain boundaries' five rotational degree of freedom. *Scripta Materialia* 81, 16-19.
- McLaren, A.C., 1986. Some speculations on the nature of high-angle grain boundaries in quartz rocks. *Laboratory Studies: The Paterson Volume* (ed. by B.E. Hobbs and H.C. Heard), Vol. 36, pp. 233-245. American Geophysical Union, Washington.
- Peternell, M., Kohlmann, F., Russell-Head, D.S., Wilson, C.J.L., Seiler, C., Gleadow, A.J.W., 2009. A new approach to crystallographic orientation measurements for apatite fission track analysis: Effects of crystal morphology and implication for automation. *Chemical Geology* 265, 527-539.
- Peternell, M., Hasalová, P., Wilson, J.L., Piaziolo, S., Schulmann, K., 2010. Evaluating quartz crystallographic preferred orientations and the role of deformation partitioning using EBSD and fabric analyser techniques. *Journal of Structural Geology* 32, 803-817.
- Peternell, M., Russell-Head, D.S., Wilson, C.J.L., 2011. A technique for recording polycrystalline structure and orientation during in situ deformation cycles of rock analogues using an automated fabric analyser. *Journal of Microscopy* 242, 181-188.
- Peternell, M., Dierckx, M., Wilson, C.J.L., Piaziolo, S., 2014. Quantification of the microstructural evolution of polycrystalline fabrics using FAME: application to in situ deformation of ice. *Journal of Structural Geology* 61, 109-122.
- Poirier, J.-P., 1985. *Creep of crystals*. Cambridge University Press, Cambridge.
- Prior, D.J., Boyle, A.P., Brenker, F., Cheadle, M.C., Day, A., Lopez, G., Peruzzo, L., Potts, G.J., Reddy, S., Spiess, R., Timms, N.E., Timby, P., Wheeler, J., Zetterström, L.

- (1999) The application of electron backscatter diffraction and orientation contrast imaging in the SEM to textural problems in rocks. *American Mineralogist* 84, 1741-1759.
- Rolland du Roscoat, S., King, A., Philip, A., Reischig, P., Ludwig, W., Flin, F., Meyssonier, J., 2011. Analysis of Snow Microstructure by Means of X-Ray Diffraction Contrast Tomography. *Advanced Engineering Materials* 13, 128-135.
- Rollet, A.D., Lee, S.-B., Campman, R., Rohrer, G.S., 2007. Three-Dimensional Characterization of Microstructure by Electron Back-Scatter Diffraction. *Annual Review of Material Research* 37, 627-658.
- Sutton, A. P., Ballu, R. W., 2006. *Interfaces in Crystalline Materials*. Clarendon Press, Oxford.
- Tröger, W.E., 1982. *Optische Bestimmung der gesteinsbildenden Minerale. Teil 1 Bestimmungstabellen*. 5rd edn. Schweizerbart'sche Verlagsbuchhandlung, Stuttgart.
- Vernon, R.H., 1976. *Metamorphic Processes*. Allen and Unwill, London.
- Vernon, R.H., 2004. *A Practical Guide to Rock Microstructures*. Cambridge University Press, Cambridge.
- Voll, G., 1960. New work on petrofabrics. *Liverpool and Manchester Geological Journal* 2, 503-567.
- Wenge Yang, Larson, B.C., Tischler, J.Z., Ice, G.E., Budai, J.D., Liu, W., 2004. Differential-aperture X-ray structural microscopy: a submicron-resolution three-dimensional probe of local microstructure and strain. *Micron* 35, 431-439.
- White, S., 1977. Geological significance of recovery and recrystallization processes in quartz. *Tectonophysics* 39, 143-170.
- White, J.C., White, S.H., 1981. On the structure of grain boundaries in tectonites. *Tectonophysics* 78, 613-628.
- Wilson, C.J.L., Russell-Head, D.S., Sim, H.M. (2003) The application of an automated fabric analyser system to the textural evolution of folded ice layers in shear zones. *Annals of Glaciology* 37, 7-17.
- Wilson, C.J.L., Russell-Head, D.S., Kunze, K., Viola, G., 2007. The analysis of quartz *c*-axis fabrics using a modified optical microscope. *Journal of Microscopy* 227, 30-41.
- Wilson, C.J.L., Peternell, M, 2011. Evaluating ice fabrics using fabric analyser techniques in Sørdsdal Glacier, East Antarctica. *Journal of Glaciology* 57, 881-894.
- Winkler, B., 2006. Applications of neutron radiography and neutron tomography. *Reviews in Mineralogy & Geochemistry* 63, 459-471.
- Wolf, D. and Yip, S. (1992) *Materials Interfaces*. Chapman and Hall, London.

- Wirth, R., 1996. Thin amorphous films (1-2 nm) at olivine grain boundaries in mantle xenoliths from San Carlos, Arizona. *Contributions to Mineralogy and Petrology* 124, 44-54.
- Zaefferer, S., Wright, S. I., Raabe, D., 2008. Three-Dimensional Orientation Microscopy in a Focused Ion Beam-Scanning Electron Microscope: A New Dimension of Microstructure Characterization. *Metallurgical and Materials Transactions A* 39, 374-389.

4. A new insight into the steady state in constant strain rate pure shear experiments

Abstract

Understanding of the microstructural evolution and equilibrium grain size development during steady state tertiary flow is essential in order to improve our knowledge of ice and rock deformation. This contribution presents results from 2d in situ deformation experiments of natural glacier ice, with the development of the microstructure in the tertiary flow regime. We conducted one relative slower ($1 \cdot 10^{-6}$ 1/s) and two relative faster-strain rate ($2 \cdot 10^{-6}$ 1/s) pure shear experiments at -10°C , up to a shortening of $\sim 57\%$. Microstructure development was followed by time-lapse observations using an automatic fabric analyser microscope. By introducing two new microstructure-based indicators for the steady state, the ‘seeding rate’ and the ‘microstructure activity’, it was shown that a steady state was only reached in the two high strain rate experiments. In contrast, in the slow strain experiment there is insufficient seeding of new grains to enable continuous recovery and there is a bimodal grain size distribution. These results are explained by inhomogeneous stress concentration on grains in ‘hard’ glide position together with the development of a bimodal grain size distribution. In the case of such a bimodal distribution the use of a stabilised mean grain size as a stress piezometer and a criterion for steady state should be handled with caution.

This chapter was send to Earth and Planetary Science Letters as:

Hammes, D. M., Peternell, M., Wilson, C.J.L.: A new insight into the steady state in constant strain rate pure shear experiments.

4.1 Introduction

Plastic deformation of crystalline solids such as ice and quartz produces distinctive and informative microstructures. These include lattice distortion, which reflects the density of lattice defects; low-angle boundaries within grains. These reflect the operation of recovery processes such as dislocation climb; and dynamic recrystallization, which reflects a variety of processes that produce new grains as well as the migration of grain-boundaries driven by lattice strain energy and grain-boundary surface energy (Urai et al., 1986). In a steady state tertiary flow, deformation and crystal rotation are balanced by crystal growth and change, leading to an equilibrium grain size irrespective of the initial grain size and has provided geologists with a tool, known as the dynamically recrystallized grain-size piezometer (Twiss, 1986; Stipp and Tullis, 2003).

Microstructures can in principal provide information on the slip systems active during deformation (Lloyd et al., 1997; Halfpenny et al., 2006), and on the magnitude of stress within a grain. In crystalline solids such as ice and quartz deformation depends on the resolved shear stress for slip on the basal plane (Weertman, 1983; Wilson et al., 2014). In ice, the contribution of non-basal slip is in general insignificant (Duval et al., 1983) except if basal slip is impeded by a ‘hard’ grain or a constraining plate during experimental deformation, in which case prismatic slip and/or kinking is produced (Wilson et al., 2014). Depending on grain orientation and magnitude of the resolved shear stress it is possible to differentiate between ‘easy’ and ‘hard’ glide positions and identify ‘soft’ and ‘hard’ grains within a polycrystalline aggregate. For grains with basal planes oriented at $\sim 45^\circ$ to the compression axis, they will be in an ‘easy glide’ orientation and will have a high Schmid factor (Azuma, 1995).

There is a substantial amount of published information about the mechanical properties and rheology of polycrystalline ice (e.g., Kamb, 1972; Jacka, 1984; Jacka and Jun, 1994; Wilson and Peternell, 2012; Piazzolo et al., 2013), and there has also been extensive discussion of microstructural evolution and recrystallization mechanisms involving bulges of grain boundaries, microstructures reflecting increasing lattice mismatch (e.g. subgrain rotation; Stipp et al., 2003; Urai et al. 1986), and grain boundary migration (GBM, De La Chapelle and Castelnau, 1998; Piazzolo et al., 2013; Faria et al., 2014; Wilson et al., 2014; Montagnat et al., 2015), but there has been little discussion of the influence of resolved stress on the transition between these microstructural types. Similarly there is also a scarcity of microstructural data involving grain-scale dynamics during a steady state tertiary

flow regime. In particular it is believed that grain-size represents an equilibrium between grain-size reduction processes driven by GBM under the influence of either lattice strain energy or surface energy (e.g., Derby and Ashby, 1987; De Bresser et al., 1998; Montési and Hirth, 2003; Cross et al., 2015).

In this study we use natural ice as an analogue for quartz from the point of view of its deformational characteristics (Kamb, 1972; Wilson et al., 2014) to look at the microstructural changes occurring during a high-strain pure shear deformation. It has a similar symmetry (hexagonal vs. trigonal for low-T quartz), similar set of slip systems (easy slip on the basal plane, harder slip on prism, rhomb, and pyramid planes), and it shows similar microstructures. A substantial body of experimental and theoretical work has also shown that grain size reduction caused by dynamic recrystallization during climb-assisted dislocation creep (Poirier, 1985) can result in a steady-state grain size after strains involving ~20% shortening. Whereas, few longer experiments involving strains >50% have been undertaken because of the impractically long time-frame involved, and a belief that grain sizes at end of the experiment reflects the processes during a constant creep rate regime. The present paper addresses this issue using a newly developed approach, where we have been able to visualize the microstructure evolution during what appears to be steady-state tertiary flow regime. We will identify the role played by ‘soft’ and ‘hard’ grains during three high-strain *in-situ* deformation experiments, which most researchers would consider to have reached a steady-state grain size.

4.2 Methods

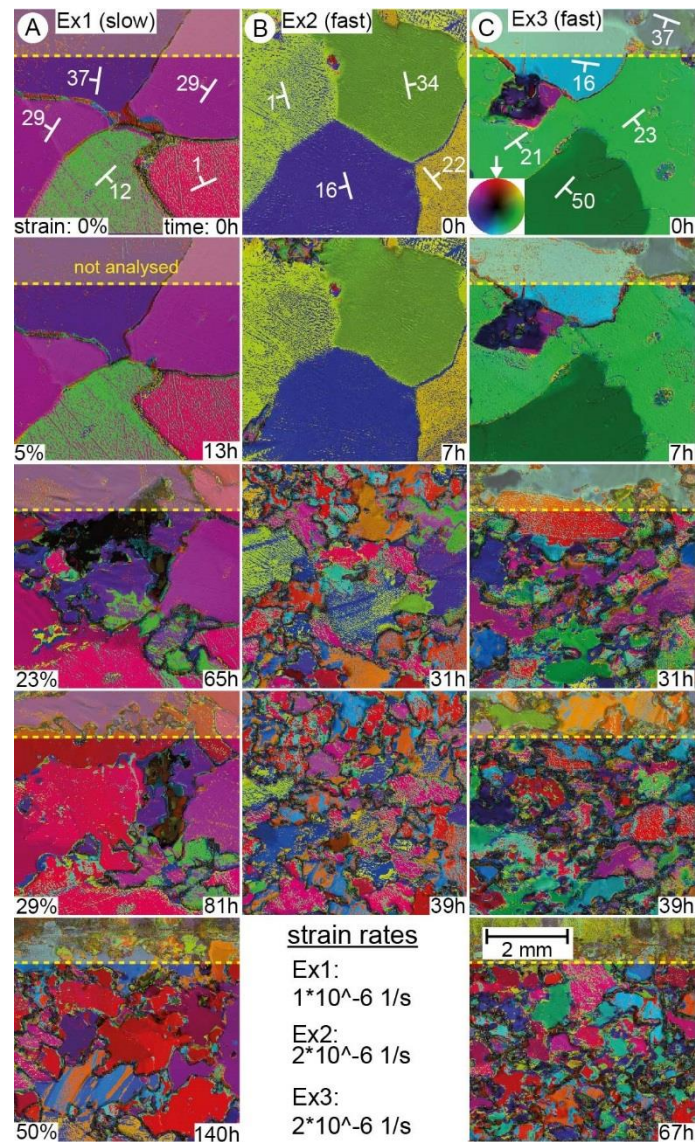


Figure 4.1. Sequence of axial distribution analysis (AVA) images taken during a vertical shortening of ice showing microstructural development of Ex1 (A), Ex2 (B) and Ex3 (C). The initial orientation of (0001) or basal plane in the large grains is represented by the white dip and strike symbol. Inset shows different colours indicating *c*-axis orientation with respect to vertical compression axis (white arrow).

The natural ice used in this study was obtained from ~10 cm diameter ice cores taken from the Sørødal Glacier, East Antarctica (Wilson and Peterzell, 2011). Wafers, ~1.5 cm x 3 cm large and 250 μ m thick, were cut from the ice cores and polished on both sides. The samples ‘CG_3b_80-110_1’, ‘CGN_7_265-290’ and ‘RFD_289’ (referred to as Ex1, Ex2 and Ex3 in the following text) consist of millimetre sized grains and few submillimetre large interstitial grains for Ex3, and an optically derived arithmetic mean grain size varying from ~1600 μ m (Ex1, Ex2) to ~620 μ m (Ex3). A 5 mm x 5 mm large area was

located within each of the three wafers and was the focus for attention during the subsequent deformation. Samples were then deformed in a pure shear deformation press under an automatic fabric analyser microscope (Peternell et al., 2011), and a record of the microstructural evolution was recorded every 3 minutes (see supplementary Movie). The microstructural evolution in the selected area was recorded at a spatial resolution of 5 $\mu\text{m}/\text{pixel}$ during steady-state strain rates of $1 \cdot 10^{-6}$ 1/s (Ex1; named ‘slow’ experiment) and $2 \cdot 10^{-6}$ 1/s (Ex2 and Ex3; named ‘fast’ experiments). The samples were shortened to a total of 57.6% (Ex1), 37.9% (Ex2) and 50.3% (Ex3), respectively. The single-frame measurements recorded by the fabric analyser were supplemented with results from the FAME analysis (Fabric Analyser-based Microstructure Evaluation; Peternell et al., 2014; Hammes and Peternell, 2016). FAME enables automatic and continuous grain labelling, and therefore extraction of grain parameters such as size (equal area diameter method), shape and CPO. With FAME we calculated hard/soft grain maps, which indicate for each pixel inside a grain its tendency to be in a ‘hard’ or ‘soft’ basal glide position based on a modification of the Schmid factor (Azuma, 1995), which does not consider the constriction of the sample between the two glass plates. For example, the top left grain in Ex1 (0%, Fig. 4.1A) is in a moderately hard glide position based on the Schmid factor, and develops strong kink bands visible at 23% shortening, indicating an excessive high stress concentration. Similarly the top grain in Ex3 (0%, Fig. 4.1C) is in a soft glide position but shows structures related to a high stress concentration at 23% shortening. We therefore, introduce a correction of the Schmid factor, with a hardening component that depends on the angle between the grains *c*-axis orientation and the glass plate normal (see supplementary B for details).

In this study we use the concepts of ‘seeding rate’ and ‘microstructure activity’. The seeding rate is defined as the number of new visible ($>10 \mu\text{m}$) grains per hour and was calculated by noting the time stamp of every new seeding for the three experiments. The seeding events were then sorted into bins and interpolated. The number of bins is equal to the square root of the observed seeding in each experiment. The microstructure activity is a measure of the overall *c*-axis orientation change in area fraction per time. It is an indicator for all processes leading to change in microstructure in terms of surface area, such as recrystallization and grain boundary migration. The microstructure activity is calculated by comparing the pixel-wise orientation after definite time intervals and plotted versus strain. For each strain increment, the number of pixels whose orientation changes larger than a given threshold is counted and set in proportion to the total pixel number of

the observed area (Fig. 4.2). The most convincing results were achieved by using a threshold of 25° and a time interval length of 15 minutes.

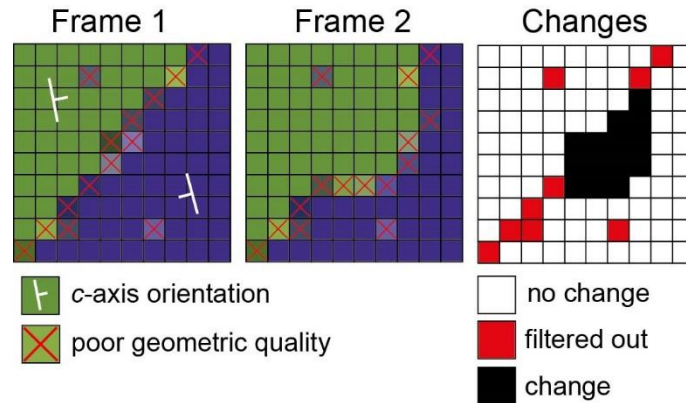


Figure 4.2. Visualisation of the calculation of the microstructure activity on a simplified example of grain boundary migration. The orientation between two frames is compared pixel wise and the pixel with a change in orientation larger than a given threshold are counted and set in relation to the total number of pixels. To minimise the effect of static grain boundaries, which often state large random changes in orientation, pixel with poor geometric quality (Paternell et al., 2009) in both frames are filtered out.

4.3 Results

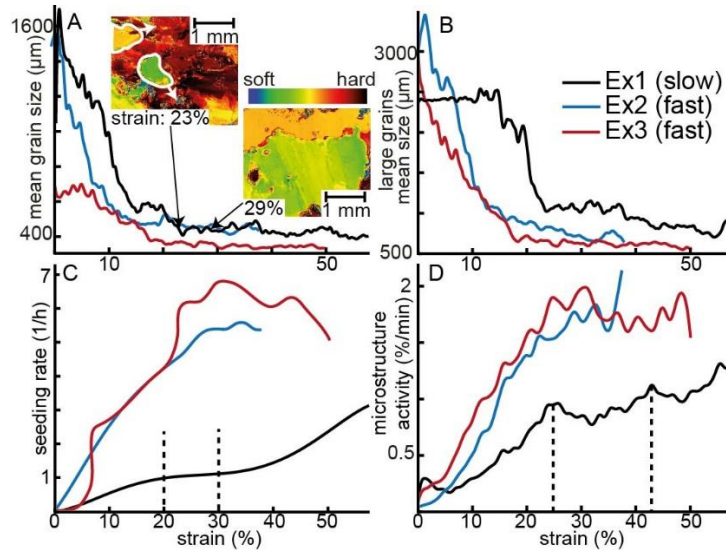


Figure 4.3. Results from microstructural analysis of the three experiments. A: Correlation between smoothed mean grain size and strain during progressive deformation (see supplementary for further information). B: Smoothed mean grain size vs. strain of calculated grains larger than the overall mean shown in A. C: Interpolated rate of newly seeded grains per time interval versus strain. B: Interpolated microstructure activity indicates overall *c*-axis orientation change in area fraction per time with progressive strain (further explanation in the text). ‘Softness’ maps represent grains, which are favourably oriented for easy glide directions and therefore preferably deformed in contrast to ‘hard’ grains (see supplementary A). White arrows indicate primary growth direction of the corresponding grains. Dashed lines indicate noteworthy spots.

4.3.1. Slow deformation (Ex1)

The initial microstructure consists of 5 large (1090-1320 μm) ice grains with basal planes that are oriented in both ‘hard’ and ‘soft’ glide orientations (Fig. 4.1A). During the initial 5% of shortening, the grain boundaries start to bulge. This is followed by the onset of nucleation along the grain boundaries (Fig. 4.1A: 5%; supplementary movie). From ~8% to ~23% a development of kinking is observed in the top left grain. Until ~14% strain the 5 initial large grains can be tracked and their mean grain size stays constant, followed by a sharp decrease from ~14% to ~23% (Fig. 4.3B). The overall mean grain size decreases from ~1300 μm to ~430 μm between 5% and 23% strain (Fig. 4.3A), and the grain size distribution is bimodal (Fig. 4.1A: 23%). Seeding rate and microstructure activity increased moderately from 0% to ~20% shortening (Fig. 4.3C, D). The ‘hard’ grain fraction increases until ~23%, and ‘hard’, ‘medium’ and ‘soft’ fractions reach a state of equal proportions (Fig. 4.4A). Between ~23% and ~29% shortening two ‘medium-hard’ grains grow rapidly to the expense of ‘hard’ grains (Fig. 4.3A, insert; Fig. 4.1A, 29%), and the grain fraction of medium large grains increases significantly during this stage (Fig. 4.4A). The seeding rate is still increasing from ~20% to ~30%, but less significantly than in the stages before and after (Fig. 4.3C). At ~23% the overall mean size stabilises (Fig. 4.3A) in contrast to the larger grains further decreasing in size (Fig. 4.3B). This is in accordance to a flattening of microstructure activity curve, which becomes serrated and shows two local maxima at ~25% and 43% (Fig. 4.3D). Some of the initial grains are still recognized as fragments at 29% strain. From ~30% to the end of the experiment the populations of the ‘medium hard’ grains are decreasing and the ‘hard’ and ‘soft’ grain fractions increase to reach a second state of equal proportions (Fig. 4.4A). In this strain regime the microstructure consists dominantly of medium sized interlobate grains and a number of small grains (Fig. 4.1A).

4.3.2. Fast deformation (Ex2 and Ex3)

In Ex2 the microstructure consists initially of 4 large (540-2210 μm) grains (Fig. 4.1B), in contrast to Ex3 where 3 large (820-2070 μm) grains are accompanied by small grain aggregates. Nucleation driven grain size reduction starts during the first ~3% shortening in Ex2. Bulging and GBM lead to slight grain size increase in Ex3 during the first ~5% of shortening (Fig. 4.1B, C; supplementary Movie). The initial stage is followed by a nucleation event and the mean grain size decreases in Ex2 and Ex3 until ~18% and

~20% shortening and stabilises at ~410 μm and ~340 μm , respectively (Fig. 4.1B, C, Fig. 4.3A; supplementary Movie). In contrast to Ex1 (Fig. 4.3B), the microstructures in Ex2 and Ex3 homogenize and a unimodal grain size distribution develops (Fig. 4.3B). The average size of the large grains decreases to finally stabilise after ~32% (Ex2) and ~20% strain (Ex3), respectively (Fig. 4.2B). With ongoing deformation the grains become increasingly interlobate and the grain boundaries ‘fuzzy’ (Fig. 4.1A, B). No significant fragments of the initial large grains are observed at 29% shortening and also newly seeded grains are increasingly replaced (Fig. 4.1B, C; supplementary Movie): Almost none of the grains observed at 23% are recognisable at 29% (Fig. 4.1B, C). The seeding rate shows an increase (Fig. 4.3C) in both experiments and stabilises after ~27% (Ex2) and ~23% (Ex3). The microstructure activity in Ex2 and Ex3 increase significantly until ~25% and ~29% and flattens off, but shows a second sharp increase after ~36% in Ex2. The population of the ‘medium hard’ grains in Ex3 is decreasing until ~10%, followed by a slight increase afterwards until the end of the experiment (Fig. 4.4B). The grain fractions of the ‘hard’ and ‘soft’ grains are significantly smaller, have similar magnitudes and show fluctuations, but no noteworthy trends (Fig. 4.4B).

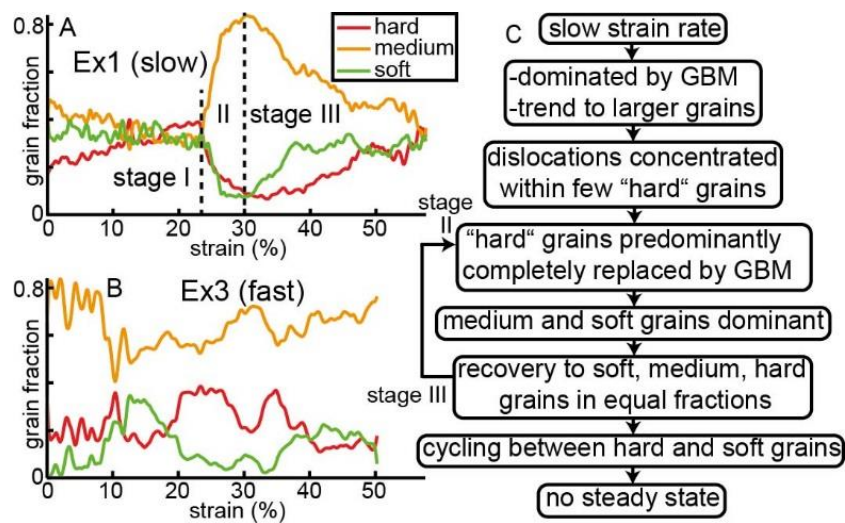


Figure 4.4. Smoothed area fractions of the ‘hard’, ‘medium’ and ‘soft’ grains vs. shortening in Ex1 (A) and Ex3 (B), and (C) corresponding workflow to explain the differences between Ex1 and Ex2, 3 (C). In Ex1 three stages in the ‘softness’ population are to be distinguished which suggest a cycling of the populations and inhibits the reaching of a steady state.

4.4. Discussion

The initial microstructures in Fig. 4.1 show similar grain sizes for the large grains (Fig. 4.1), but Ex3 has smaller interstitial grains at the beginning of the experiment. This bimodal distribution causes a significant statistical decrease in the starting grain size (Fig. 4.3A). Furthermore, the stabilised mean size at $\sim 38\%$ shortening in the ‘fast’ (Ex2; $410\ \mu\text{m}$) is similar to the ‘slow’ (Ex1; $420\ \mu\text{m}$) but different to ‘fast’ (Ex3; $340\ \mu\text{m}$; Fig. 4.3A). Thus the final mean grain size appears to depend on the initial crystal size but not on the applied stress. However, looking on the large grain fractions separately (Fig. 4.3B), grain size distributions of the three experiments reflect a unimodal distribution with final mean grain sizes only depending on the applied stress and therefore in accordance to with the work of Jacka and Li Jun (1994). We suggest that classical grain size distribution diagrams might be misleading in the case of many bimodal size distributions, in particular distributions with large size differences.

The definition of a ‘steady state’ as used in system theory and thermodynamics requires that the state variables or properties of the system are unchanging in time (Morrill 1972). In most ice deformation experiments, stabilization of the mean grain size during tertiary creep has been taken as an indication that the system is in steady state, and grain size reducing processes are balanced by grain growth (Budd and Jacka, 1989). Grain size is not the only measurable property in an ice deformation experiment, and we therefore, extend our observations on the seeding rate (Fig. 4.3C) and the microstructure activity (Fig. 4.3D). Both express the change in microstructure and are therefore indicators for state variables such as the internal energy and entropy. In the “fast” experiments (Ex2 and Ex3) all three variables stabilise at $\sim 20\%$ strain. The sharp increase at $\sim 36\%$ shortening in Ex2 is a local fluctuation and no indicator for a general change in behaviour, because no comparable event is observed in the seeding rate nor the microstructures. In contrast, in the ‘slow’ experiment (Ex1) seeding rate and microstructure activity continuously increase with ongoing deformation (Fig. 4.3C, D). This is an indication that Ex1 has not yet reached steady state.

The main reasons for not reaching steady state is the relative lower strain rate in Ex1 compared to Ex2 and Ex3. With the development of bimodal grain size distribution after the first $\sim 20\%$ of shortening in Ex 1. (Figs. 4.1, 4.4C; supplementary movie). Higher strain rates lead to higher stresses applied on the sample and therefore to an increase in

dislocation density (Johnston and Gilman, 1959). The increased dislocation density effects an intensified recrystallization (Duval et al., 1983) leading to smaller grain sizes and a unimodal grain size distribution. The observation is supported by the higher seeding rates and microstructure activities in experiments Ex2 and Ex3 in contrast to Ex1 (Fig. 4.3B and C). The intensified recrystallization, with the progress of deformation, increasingly removes dislocations until the rates of dislocation generation and removal are equal, and the recrystallization rate is consequently stagnating. This leads to a steady state, as observed in experiments Ex2, 3.

In stage I of Ex1 dislocations are statistically more concentrated primarily in the few large ‘hard’ grains and lead to a ‘hardening’ of the overall microstructure (Fig. 4A, C), reflected e.g. by kinking (Fig. 4.1A: 23%). In contrast to the fast experiments there is insufficient seeding of new grains (Fig. 4.3C) to enable a continuous recovery. After a critical state of ‘hardening’ is reached dislocation annihilation driven processes become dominant and lead to an abrupt depletion of the large ‘hard’ grains by GBM (Fig. 4.4A: stage II; Fig. 3A, inlet). A subsequent stage of hardening follows, similar to stage I (Fig. 4.4A: stage III). The repeated concentration of dislocations in large hard grains at this stage is caused by bimodal grain size distribution. The relative slower strain rate in Ex1 results in significant GBM and reduced seeding of new grains, which lead to the preservation of the bimodal grain size distribution after ~23% (Fig. 4.1A). This cycling-type behaviour of the ‘hard’, ‘medium’ and ‘soft’ grain proportions inhibits a steady state (Fig. 4.4C) in Ex1 during end of the experiment at 50% of shortening.

The present results thus need to be considered in any general model for grain size evolution in any material. As the presence of ‘hard’ vs. ‘soft’ grains and grain size distributions should be taken into account for the recrystallized grain size in relation to the deformation conditions (strain rate and temperature). The implications are significant as it would mean that dynamically recrystallization cannot be seen as a true grain-size piezometer as envisaged by Twiss (1986) or Stipp and Tullis (2003). Instead, deformation of a given material would be controlled by a combination of both diffusion and dislocation mechanisms as pointed out by De Bresser et al (2001), as self-organization of the grain size occurs in the material. Thus the widely accepted model, an equilibrium grain size, is not necessary for major rheological weakening in the Earth.

4.5. Conclusions

Our results indicate that the flow of ice and the establishment of a stabilised grain size (e.g. Budd and Jacka, 1989) may be much more heterogeneous than generally assumed, as the final microstructure may not reveal earlier heterogeneities in grain size evolution. By evaluating the rate of newly seeded grains and by introducing the ‘seeding rate’ and ‘microstructure activity’ enabled us to define the steady state based on the dynamics of the microstructure. By considering these two quantities it has been shown that ice deformed at a strain rate of $\sim 1 \cdot 10^{-6}$ 1/s at high temperatures (-10°C) does not necessarily lead to a steady state, not even at a strain of $\sim 58\%$ (Ex1). In comparison to the relative faster experiments, GBM becomes more dominant in a relative slower deformation and this leads to a bimodal grain size distribution. Dislocations are then concentrated on larger ‘hard’ grains, resulting in a cycling type behaviour of ‘hard’, ‘medium’ and ‘soft’ grain ratios, impeding the system to reach steady state. Furthermore, in the case of a strong bimodal grain size distribution, classical grain size vs. strain diagrams can lead to a wrong impression and need to be used with caution. Recrystallization is increasing with the progress of deformation (Fig. 4.3B, C), but grain size reduction processes and grain growth are in a balanced state as indicated by the constant grain size. The mean grain size is therefore no reliable indicator for the steady state. Only small changes in strain rate may dictate whether steady state can be reached. This may have implications for the prediction of the rheology in ice masses or other rocks, as it is not guaranteed that in all cases where ice or quartz is deformed to a high strain that a steady state is necessarily reached, even at a comparable low strain rate.

Supplementary Material

This chapter contains a two parts supplementary (A and B). In addition a supplementary movie is available on the attached CD ROM.

Supplementary A: Smoothing of data

To determine grain-based statistics, such as the mean grain size, from the pixel-based raw data of the Fabric Analyser, a grain labelling process is necessary (Paternell et al. 2014, Hammes et al. 2016). Every frame recorded during a deformation experiment is

labelled independently. Due to changes in the orientation and recrystallization two grains, which were labelled as separated grains can be labelled as a single grain in the next frame, which causes fluctuations in the mean grain size evolution. This effect is stronger in case of a total grain number $\lesssim 50$, and shown in the hard/soft area fraction vs. strain (Fig. 4.5: A-F) or the mean grain size (Fig. 4.5: G-I) at low strains ($\lesssim 10\%$), where the number of grains is even below ~ 10 . We therefore, apply a MATLAB® smoothing function to clarify trends and minimize the influence of fluctuations as a result of the FAME labelling algorithm. The degree of smoothing was chosen depending on the number of frames (Fig. 4.5, black line).

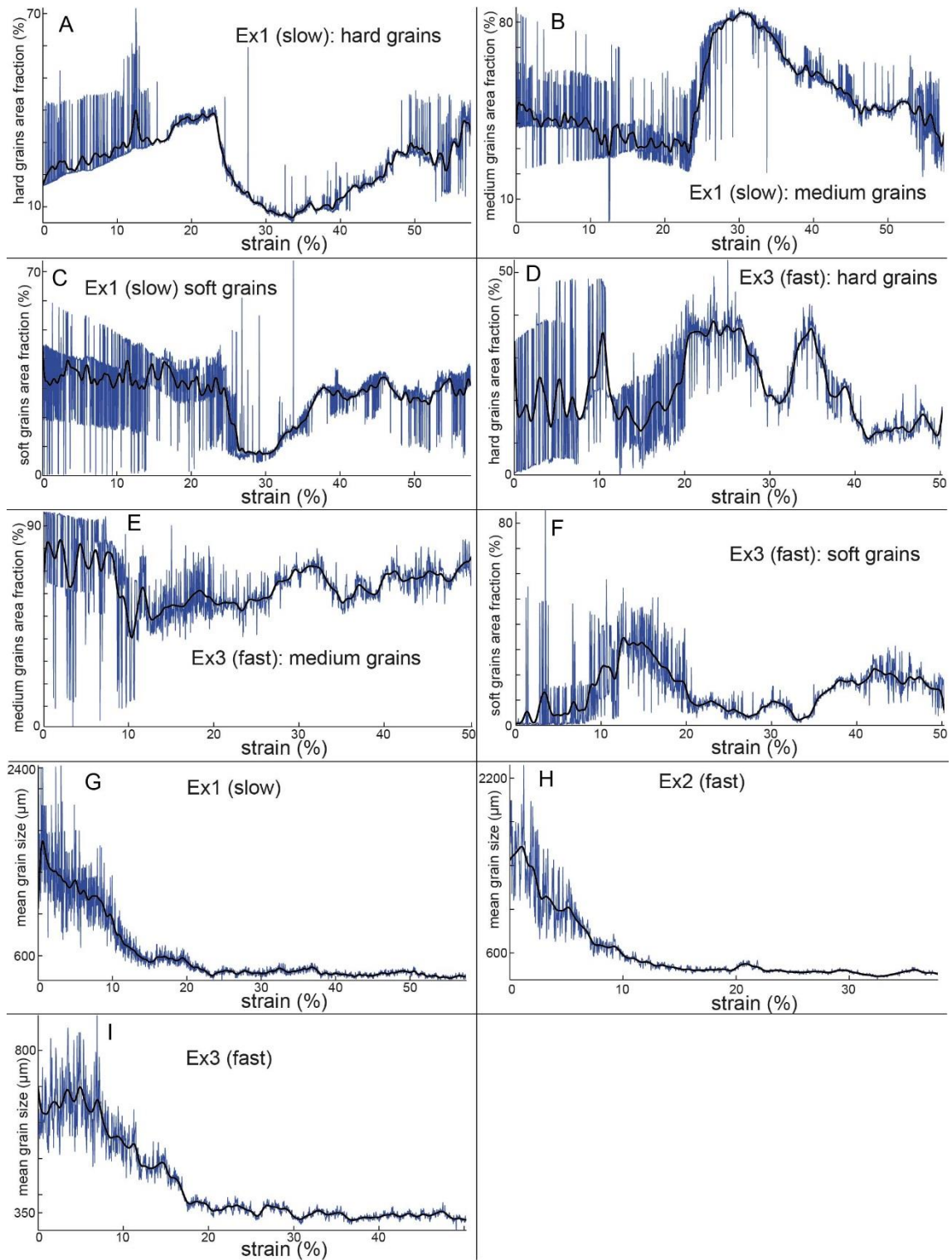


Figure 4.5. Raw (blue lines) and smoothed data (black lines) of area grain “softness” fractions vs. strain (A-C: Ex1, D-F: Ex3) and mean grain size (G-I).

Supplementary B: “Softness of grains and influence of glass plates

The concept of “hard” and “soft” grains is based on the assumption that slip occurs basically on the basal plane and other slip systems are less readily activated (Wilson et al., 2014). “Soft” grains are considered to be easier deformed than its “hard” counterparts. Therefore, the deformability of a grain depends primarily on the orientation of the basal plane (perpendicular to the crystallographic c -axis) relative to the direction of deformation.

We calculate the Schmid factor S using the equation (e.g. Azuma 1995):

$$S=|\cos(\text{angle1})*\sin(\text{angle1})^2| \quad (4.1)$$

The “angle1” is the angle between the deformation axis and the crystallographic c -axis. The factor $*2$ and the absolute is used for scaling. Thus a Schmid factor S of 0 indicates a maximal hard grain and a factor of 1 a maximal soft grain.

In case of 2D deformation experiments, the sample is constrained between two glass plates and the easy glide in some grains may be therefore restricted. This is best shown by the development of kink bands in the grain. Therefore a correction of the Schmid factor S is necessary and a correction factor *corfac* is introduced and multiplied with S to receive a corrected Schmid factor S' :

$$S'=corfac*S \quad (4.2)$$

For estimating the influence of the glass plates the direction of the crystallographic c -axis, which is perpendicular to both the basal plane and the a -axes, is considered (Fig. 4.6). The c -axis orientation is recorded by the Fabric Analyser. Three principal cases of basal plane orientation related to the glass plates are considered: 90° , 45° and 0° (Fig. 4.6, D-I). Due to the crystal symmetries, an influence of the basal plane azimuthal orientation (Fig. 4.6B) can be neglected in this simplified approach. In case of a basal plane parallel or perpendicular to the glass plates the basal plane can slip in any direction without being impaired by the plates (Fig. 4.6D). Nevertheless, grains in this orientation are already maximal hard due to the Schmid factor S and slip is less likely to occur. If the basal plane is perpendicular to the glass plates (latitude: 0°), slip can occur between the glass plates without being impeded (Fig. 4.6E, F). This can further be illustrated using the stereographic projection (Fig. 4.6G). The c -axis orientation of a grain (red dot) has the tendency

to move under uniaxial deformation (vertical arrows) in direction of the north/south poles. This incremental movement is possible by free slip directions along the azimuth and therefore not impeded by the glass plates. In case of the c -axis latitude oriented 45° to the glass plates, the slip will be in direction of the glass plates and impeded for this slip system (Fig. 4.6H). In the stereographic projection the movement of the c -axis orientation to the north/south poles is only possible along the latitude direction, which involves interaction with the glass plates (Fig. 4.6I). Grains in this orientation therefore get “harder” due to the influence of the glass plates. Nevertheless, activation of the prism can still lead to slip in this orientation. The correction factor *corfac* is therefore ≈ 1 for latitudes 0° and 90° (not impeded). At 45° it is smaller 1, because basal slip is restricted by the glass plates, but larger 0, due to possible activation of prism slip, and the values between are interpolated by a sine function (Fig. 4.6J; blue line):

$$\text{corfac} = 1 - (1 - \text{gpi}) * \sin(\text{lat} * 2) \quad (4.3)$$

The factor *2 considers that the curve is described by a half sine. An interpolation by linearization (Fig. 4.6J; black line) would also be possible, but a sine function seems to be a more reasonable approach, because the geometry of the slip plane is mostly described by trigonometric functions, such as the uncorrected Schmid factor S . The constant gpi (“glass plate influence”) defines the actual magnitude of the influence of the glass plates. $\text{gpi}=1$ means no influence, $\text{gpi}=0$ maximal influence. Comparison with the expected behaviour of the microstructure, such as occurrence of kinking in very hard grains, leads to a gpi of 0.4, which was used throughout this study.

In Fig. 4.2A and B in the main text “hard”, “medium” and “soft” grains refer to corrected Schmid factors of $0 \leq S'$, $0.33 < S' < 0.66$ and $S' \geq 0.66$, respectively.

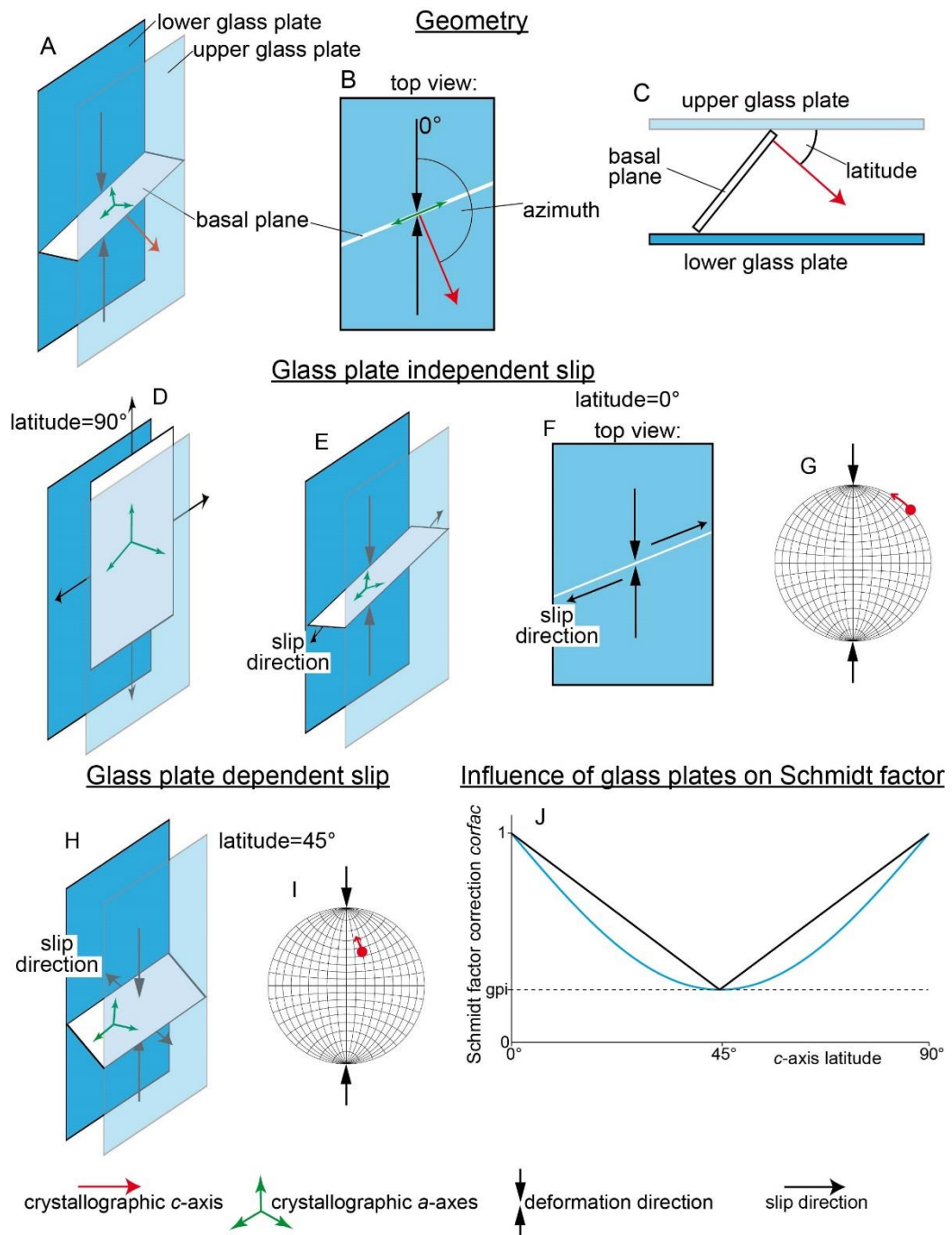


Figure 4.6. Simplified model of correction of the Schmid “softness” factor by considering the influence of the glass plates.

Geometry

Visualisation of the crystallographic c -axis coordinate system in relation to the crystal basal plane, the a -axes (both perpendicular to the c -axis) and the deformation direction (vertical). A: arbitrary crystal basal plane orientation in 3D. B and C depict the same

orientation as A, but view perpendicular (B) and parallel to the glass plates, (C) azimuth and latitude components of the c -axis.

Glass plate independent slip

Two different orientations of the basal plane relative to the deformation direction where basal slip is not influenced by the glass plates. If the basal plane is oriented parallel to the glass plates (latitude= 90°) slip can occur parallel to the glass and is not impeded (D). In case of the basal plane oriented perpendicular to the glass plates (latitude= 0°), free slip directions also occur (E; top view: F). In the stereographic projection incremental movement of a particular grain with a c -axis latitude of 0° (red dot) in direction of the deformation direction is possible along the azimuth coordinate and therefore independent from the glass plates (G).

Glass plate dependent slip

If c -axis is oriented at an axis latitude 45° to the glass plates, a slip component will be in direction of the glass plates and c -axis rotation towards the shortening direction will be impeded (H). In the stereographic projection the c -axis can only rotate to the north/south poles along the latitude coordinate and is therefore impeded in its movement by the glass plates (I).

Influence of glass plates on Schmidt factor

(J) Schmidt factor correction “corfac” plotted vs. c -axis latitude. “corfac” is multiplied with the Schmid factor to consider an increased hardening of grains which are unfavourable oriented for slip relative the glass plates. The basal slip is not impeded by the glass plates at 0° and 90° (corfac=1) and maximal impeded at 45° latitude (corfac<1). The glass plate influence factor (gpi) defines the magnitude of the influence. Based on the possible activation of prism slip it is considered to be >0 . Comparison with the expected behaviour of the microstructure, such as occurrence of kinking in very hard grains, leads to gpi=0.4.

References

- Azuma, N., 1995. A flow law for anisotropic polycrystalline ice under uniaxial compressive deformation. *Cold Region Sciences Technology* 23, 137-147.
- Budd, W.F., Jacka, T.H., 1989. A review of ice rheology for ice sheet modelling. *Cold Cold Regions Science and Technology* 16, 107-144.
- Cross, A. J., S. Ellis, D. J. Prior, 2015. A phenomenological numerical approach for investigating grain size evolution in ductilely deforming rocks. *Journal of Structural Geology* 76, 22-34.
- De Bresser, J. H. P., C. J. Peach, J. P. J. Reijs, C. J. Spiers, 1998. On dynamic recrystallization during solid state flow: effects of stress and temperature. *Geophysical Research Letters* 25, 3457–3460.
- De Bresser, J. H. P., Ter Heege, J. H., and Spiers, C. J., 2001, Grain size reduction by dynamic recrystallization: can it result in major geological weakening?. *International Journal of Earth Sciences* 90, 28-45.
- De La Chapelle, S., O. Castelnau, 1998. Dynamic recrystallization and texture development in ice as revealed by the study of deep ice cores in Antarctica and Greenland. *Journal Geophysical Research* 103, 5091-5105.
- Derby, B., M. F. Ashby, 1987. On dynamic recrystallization. *Scripta Materialia* 21, 879-884.
- Duval, P., Ashby, M.F., Anderman, I., 1983. Rate-controlling processes in the creep of polycrystalline ice. *Journal of Physical Chemistry* 87, 4066-4074.
- Faria, S. H., I. Weikusat, N. Azuma, 2014. The microstructure of polar ice. Part II: State of the art. *Journal of Structural Geology*. 61, 21-49.
- Halfpenny, A., D. Prior, J. Wheeler, 2006. Analysis of dynamic recrystallization and nucleation in a quartzite mylonite. *Tectonophysics* 427, 3-14.
- Hammes, D. M., Peternell, M., 2016. FAME: Software for analysing rock microstructures. *Computers & Geosciences* 90, 23-33.
- Jacka, T.H., 1984. Laboratory studies on relationships between ice crystal size and flow rate. *Cold Region Sciences Technology* 10, 31-42.
- Jacka, T.H., Jun, L., 1994. The steady state crystal size of deforming ice. *Annals of Glaciology* 20, 13-18.
- Johnston, G.W., Gilman, J.J., 1959. Dislocation velocities, dislocation densities and plastic flow in Lithium Fluoride crystals. *Journal of Applied Physics* 30, 129-144.
- Kamb, B., 1972. Experimental recrystallization of ice under stress, in: Heard, H., Borg, L., Carter, N.L., Ralleigh, C.B. (Eds.), *Flow and Fracture of Rocks*, American Geophysical Union, Washington DC, pp. 211-241.

- Lloyd, G. E., A. B. Farmer, D. Mainprice, 1997. Misorientation analysis and the formation and orientation of subgrain and grain boundaries, *Tectonophysics* 279, 55-78.
- Montagnat, M., T. Chauve, F. Barou, A. Tommasi, B. Beausir, C. Fressengeas, 2015. Analysis of Dynamic Recrystallization of Ice from EBSD Orientation Mapping. *Frontiers in Earth Science* 3, 411-413.
- Montési, L. G. J., G. Hirth, 2003. Grain size evolution and the rheology of ductile shear zones: from laboratory experiments to post seismic creep. *Earth and Planetary Science Letters* 211, 97-110.
- Morrill, B., 1972. An introduction to equilibrium thermodynamics. Pergamon Press, New York.
- Peternell, M., Russel-Head, Kohlmann, F., Wilson, C.J.L., Seiler, C., Gleadow, J.W., 2009. A new approach to crystallographic orientation measurement for apatite fission track analysis: Effects of crystal morphology and implications for automation. *Chemical Geology* 265, 527-539.
- Peternell, M., Russel-Head, D.S., Wilson, C.J.L., 2011. A technique for recording polycrystalline structure and orientation during in situ deformation cycles of rock analogues using an automated fabric analyser. *Journal of Microscopy*. 242, 181-188.
- Peternell, M., Dierckx, M., Wilson, C.J.L. Piazzolo, S., 2014. Quantification of polycrystalline fabric, using FAME: application to in situ deformation of ice. *Journal of Structural Geology* 61, 109-122.
- Piazzolo, S., C. J. L. Wilson, V. Luzin, C. Brouzet, M. Peternell 2013. Dynamics of ice mass deformation: Linking processes to rheology, texture, and microstructure. *Geochemistry, Geophysics, Geosystems* 14, 4185-4194.
- Poirier, J.P., 1985. Creep of crystals. Cambridge University Press, Cambridge.
- Stipp, M., Tullis, J., 2003. The recrystallized grain size piezometer for quartz. *Geophysical Research Letters* 30, 2088, 3-1 - 3-4.
- Twiss, R.J., 1986. Variable sensitivity piezometric equations for dislocation density and subgrain diameter and their relevance to olivine and quartz, in: Heard, H.C., Hobbs, B.E. (Eds.), *Mineral and rock deformation: laboratory studies*. The Paterson volume. American Geophysical Union, Washington DC, pp. 247-261.
- Urai, J.L., Means, W.D., Lister, G.S., 1986. Dynamic recrystallization of minerals, in: Heard, H.C., Hobbs, B.E. (Eds.), *Mineral and rock deformation: laboratory studies*. The Paterson volume. American Geophysical Union, Washington DC, pp. 161-199.
- Weertman, J., 1983. Creep deformation of ice. *Annual Review of Earth and Planetary Sciences* 11, 215-240.
- Wilson, C.J.L., Peternell, M., 2011. Evaluating ice fabrics using fabric analyser techniques in Sørstøl Glacier, East Antarctica. *Journal of Glaciology* 57, 881-894.

Wilson, C.J.L., Peternell, M., Piazzolo, S., Luzin, V., 2014. Microstructure and fabric development in ice: Lessons learned from in situ experiments and implications for understanding rock evolution. *Journal of Structural Geology* 61, 50-77.

5. Final conclusions and future work

This final chapter provides remarks on the preceding sections and establishes general conclusions. It further deals with possible applications of the previously described methods and provides an outlook into further research and software development.

5.1 5. Final conclusions and future work

The FAME software offers a wide range of analyses and plotting tools for processing and visualising Fabric Analyser data. The “step growth” algorithm is a significant step forward in automatic grain labelling of *c*-axis orientation data from the MTEX algorithm (Bachmann et al., 2011) and enables a user-controlled segmentation (Section 2.2.4). The testing environment facilitates the determination of the grain segmentation parameters. FAME also offers a set of plotting options for grain-based crystallographic preferred orientation diagrams, such as a ternary diagram demonstrating the fabric evolution. The FAME software (Chapter 2, Hammes and Peternell 2016) is therefore a significant improvement from the original FAME scripts published by Peternell et al. (2014).

A new way of visualising orientation data introduced by FAME are *c*-axis misorientation maps. These maps show the *c*-axis misorientation between neighbouring pixel and grain and are based on complete crystallography local misorientation maps using EBSD data (Wright et al., 2011). Fabric Analyser-based *c*-axis misorientation maps were already implemented in the FAME version submitted to Computers and Geosciences in 2015, but were only mentioned briefly in the publication (Hammes and Peternell, 2016).

FAME is able to process data acquired with different models of the Fabric Analyser, such as the G50 and the cutting edge G60. It was successfully applied on materials such as quartz, H₂O- and D₂O ice, and calcite.

Due to its user-friendly graphical interface and wide range of plotting tools FAME is widely used by other researchers for processing Fabric Analyser data, such as Peternell and Wilson (2016), Cyprych et al. (2016) and Zibra et al. (2017). FAME was also acknowledged by Hunter et al. (2017). It was further used by a number of students for their Bachelor and Master thesis, e.g. by Klement and Steitz (2014), Schneider (2016), Fuhrmann (2017), Schürmann (2017), Köpping (2017), Benoit (2017) and Heil (2017).

It was also the foundation for the analysis of the ice deformation data considered in Chapter 4. Furthermore, the data generated by FAME is also essential for the FAGO grain boundary reconstruction (Chapter 3).

5.2 FAGO grain boundary reconstruction

FAGO (Fabric Analyser Grain boundary reCOnstruction) enables the determination of the grain boundary geometry, based on Fabric Analyser data of rock thin sections. FAME is used as part of the FAGO analysis to trace the grain boundary in the 2D thin section plane. By combining this information with the retardation data the dip angle and direction can be calculated. The result can finally be used to reconstruct a 3D model of the grain boundary. FAGO was already applied successfully on 92 μm and 144 μm thick quartzite samples; the analysis of quartz in 20 μm thick samples, however, lead to unsatisfactory results.

In contrast to the manually operated u-stage FAGO is almost fully automatized and requires only minor user input. A thin section rock sample can be scanned by the Fabric Analyser in ~30-90 minutes at a resolution of 5 μm /pixel and the actual grain boundary analysis is possible on any Windows 64bit-based work station. Next to the Fabric Analyser, no further instrumentation is necessary. One drawback is that the thin section thickness required by FAGO (~100 μm) is larger than the thickness commonly used in geology (~27-30 μm) in the case of quartz. Nevertheless, samples with this thickness can also be used for the FAME analysis and regular polarising microscopy. Minerals with a higher birefringence are expected to require a reduced sample thickness. No special sample preparation of thin sections is necessary. Furthermore, the sample is not destroyed in the scanning process, as in 3D EBSD (Zaefferer et al., 2008).

Given the importance of the grain boundary geometry, e.g. for reconstruction of the metamorphic and tectonic history of rocks (e.g. Kruhl and Peternell 2002, Kruhl et al. 2013), FAGO offers new possibilities in research. Advances in this field were limited by the time-consuming and labour intensive nature of the u-stage. One possible application of FAGO, which is not practical with the u-stage, would be the analysis of grain boundaries during *in-situ* deformations experiments (Peternell et al., 2011).

5.3 *In-situ* ice deformations

The study of two relatively fast strain rates ($2 \cdot 10^{-6}$ 1/s) and one relatively low strain rate ($1 \cdot 10^{-6}$ 1/s) *in-situ* pure deformation experiments of natural ice at -10°C introduces a couple of innovative methods of microstructural analysis and enables a new view on the steady state tertiary creep.

One interesting fact is that the steady state is reached in the fast strain rate experiments, but not in the low strain rate experiment. The fact that no steady state is reached during low strain rate deformation is explained by the development of a bimodal grain size distribution and the concentration of stress primarily on larger grains in “hard” glide orientation.

Using the Schmid factor (Azuma, 1995) images can be produced which indicate if a particular grain is in a “hard” or “soft” position for basal slip. The influence of glass plates on the sample is considered in this approach. These “softness maps” are an important new tool for understanding the development of the microstructure during deformation. Based on the same principles, “softness” grain fraction statistics can be produced. A similar approach was first introduced by Alley in a different and limited way (Alley, 1988).

New insight into the microstructural development is also possible by considering the “seeding rate”. The drawbacks of this method are that the seeding of new grains needs to be observed visually and the number of new grains may be small in very low strain rate experiments. With the new G60 Fabric Analyser the observed area is more than three times larger than in the G50 used in this study, ameliorating the latter drawback significantly. Another new variable, the “microstructural activity”, was introduced, which is a measure of the rate of change in the microstructure and is calculated without any user input, without requiring a preceding FAME grain labelling.

With introducing the “seeding rate” and the “microstructural activity” it was shown that a stabilised grain size may not be a reliable indicator for steady state as was previously assumed. These two new variables enable the definition of the steady state independently from the creep rate which is commonly used, next to the grain size, for defining a steady state (e.g. Weertman, 1957). This is exceedingly important in the case of constant strain rate experiments, such as in this study, where the indication of the steady state would be not possible.

5.4 Suggestions for future work

As with a physical instrument such as a microscope or a spectrometer, the FAME software requires routine maintenance to ensure its usability. For example, the introduction of a new operating system often involves a new compilation of the software, and further development of the Fabric Analyser requires modifications. In addition, general progress in science and new frontiers in research bring the need for modifications and additional tools. Therefore, FAME is not in a final stage and, as Heraclitus (ca. 535-ca. 475 BC) taught us, “all entities move and nothing remains still” (quoted from Ademollo 2011, p. 203).

A new approach for using Fabric Analyser data would be combining *c*-axis orientation data with the retardation for identifying different minerals and therefore segmenting different phases. First attempts of the automatic discrimination of mica from quartz emerged to be successful. Segmentation of opaque minerals from the birefringent minerals was developed and incorporated into the newest FAME version and used by T.-F. Schneider for his master thesis (Schneider, 2016). The newer version of FAME, not considered in this treatise, also enables a significantly faster analysis of batch data by parallelisation and the rotation of the stereographic density plots.

FAME is expected to be the foundation for all kinds of Fabric Analyser-related data processing, such as a new method developed by J. Köpping for using the orientation of calcite twin planes for paleostress analysis (Köpping and Peternell 2017, Köpping 2017). The incorporation of the FAGO grain boundary reconstruction algorithms (Chapter 3) into FAME would also be considered as a useful extension.

Significant progress in the future is also expected in the case of FAGO. Considering the algorithms, particularly the determination of the transition region width, improvements are possible. Improvements in the design of the Fabric Analyser would possibly also lead to improvements in FAGO. In particular, the determination of the dip and the inclination direction would certainly benefit from an increased scan resolution ($<5\mu\text{m}/\text{pixel}$). FAGO was already tested on data recorded by the new G60 model. Unfortunately, the preliminary results show that the accuracy of the dip angle measurement is lower for almost vertical grain boundaries (dip angle $>80^\circ$) than in case of the G50. Nev-

ertheless, inclined grain boundaries (dip angle $<80^\circ$) can be measured with a higher accuracy. Further testing and possibly adjustments in the instrumentation and software are therefore necessary.

So far only three thin sections thicknesses (20 μm , 92 μm , 144 μm) has been tested in detail. The effect of rough or curved grain boundaries is more prominent for larger sample thicknesses, which can influence the accuracy of the grain boundary measurements. It is therefore desirable to evaluate different thicknesses to find a feasible lower threshold.

The possible applicability of FAGO on other materials besides quartz, such as calcite and olivine, was considered in this thesis? (Section 3.7), but experimental results are still lacking. A further interesting subject for research would be investigation of the grain boundary during *in-situ* ice deformations, if the low birefringence of ice is not causing any trouble.

Even without the use of FAGO, the research of *in-situ* ice deformations offers a multitude of perspectives. In the last two years the laboratories of the tectonophysics group at the Institute of Geosciences (University of Mainz) were significantly extended to enable the manufacture and *in-situ* deformation of artificial ice samples. The data acquisition is done with the new G60 Analyser which features a significantly improved accuracy of the measured *c*-axis orientation and an enlarged observation area. A number of students have already used these facilities in the context of their Bachelor- or Master thesis. In addition to comparing experiments with different external conditions, such as different strain rate and temperature, the sample can be modified prior to deformation. For example, graphite can be added to the ice as a second phase or a band of different microstructure can be formed, simulating a dyke.

New opportunities would be offered if the applied stress could be measured during the constant strain *in-situ* deformation. One approach could be the application of a load cell. Another option would be by measuring the power input of the motor of the deformation press and calibrate to scale. The second approach is expected to be less accurate, but easier to accomplish without modifying the press significantly.

In addition to new experiments, the re-analysis of historical deformation experiments offer new possibilities. For example, “microstructure activity” plots and “softness” maps can be generated and the experiments reconsidered using the new input of information.

References

- Ademollo, F., 2011. *The Cratylus of Plato*. Cambridge University Press, Cambridge (UK), pp. 538.
- Azuma, N., 1995. A flow law for anisotropic polycrystalline ice under uniaxial compressive deformation. *Cold Regions Science and Technology* 23, 137-147.
- Bachmann, F., Hielscher, R., Schaeben, H., 2011. Grain detection from 2d and 3d EBSD data – Specification of the MTEX algorithm. *Ultramicroscopy* 111, 1720-1733.
- Benoit, L. 2017. 2D in-situ deformation experiments using ice. Unpublished Bachelor Thesis, University of Mainz, Germany, pp. 28.
- Cyprych, D., Piazzolo, S., Wilson, C.J.L., Luzin, V., Prior, D.J., 2017. Rheology, microstructure and crystallographic preferred orientation of matrix containing a dispersed second phase: Insight from experimentally deformed ice, *Earth and Planetary Science Letters* 449, 272-281.
- Fuhrmann, F., 2017. Quarzite temperature of the Ballachulish complex. Unpublished Master Thesis, University of Mainz, Germany, pp. 111.
- Hammes, D. M. and Peternell, M., 2016. FAME: Software for analysing rock microstructures, *Computers & Geosciences* 90A, 23-33.
- Heil, S.M.. 2017. 2D in situ Deformationsexperimente in Eis. Unpublished Bachelor Thesis, University of Mainz, Germany, pp. 30.
- Hunter, N.J.R., Wilson, C.J.L., Luzin, V., 2016. Comparison of quartz crystallographic preferred orientations identified with optical fabric analysis, electron backscatter and neutron diffraction techniques. *Journal of Microscopy* 265, 169-184.
- Klement, V., Steitz, O., 2014. Entwicklung von Mikrostrukturen in Gesteinsanalogen – 2D in situ Deformationen. Unpublished Bachelor Thesis, University of Mainz, Germany, pp. 45.
- Köpping, J., 2017. Paleostress reconstruction using calcite twins - Method development and application to the regional tectonic evolution of the Sava-Klepa Massif (Former Yugoslav Republic of Macedonia). Unpublished Master Thesis, University of Mainz, Germany, pp. 62.
- Köpping, J., Peternell, M.: Automated paleostress analysis based on calcite twins (PACT-software)-Cretaceous tectonic evolution of the Sava-Klepa-Massif, Former Yugoslav Republic of Macedonia. *Tectonophysics (in review)*.
- Kruhl, J.H., Peternell, M., 2002. The equilibration of high-angle grain boundaries in dynamically recrystallized quartz: the effect of crystallography and temperature. *Journal of Structural Geology* 24, 1125-1137.
- Kruhl, J.H., Wirth, R., Morales, L.F.G., 2013. Quartz grain boundaries as fluid pathways in metamorphic rocks. *Journal of Geophysical Research: Solid Earth* 118. 1-11.

- Peternell, M., Russel-Head, D.S., Wilson, C.J.L., 2011. A technique for recording polycrystalline structure and orientation during in situ deformation cycles of rock analogues using an automated fabric analyser. *Journal of Microscopy* 242, 181-188.
- Peternell, M., Dierckx, M., Wilson, C.J.L., Piazzolo, S., 2014. Quantification of the microstructural evolution of polycrystalline fabrics using FAME: application to *in situ* deformation of ice. *Journal of Structural Geology* 61, 109-122.
- Peternell, M., Wilson, C.J.L., 2016. Effect of strain rate cycling on microstructures and crystallographic preferred orientation during high-temperature creep, *Geology* 44 (4), 279.
- Schneider, T.-F., 2016. In-Situ-Deformations Experimente von Quarz-Analoga unter Nutzen eines Fabric Analysers. Unpublished Master Thesis, University of Mainz, Germany, pp. 98.
- Schürmann, T., 2017. In-Situice deformation experiments. Unpublished Bachelor Thesis, University of Mainz, Germany, pp. 29.
- Weertman, J., 1983. Creep deformation of ice. *Annual Review of Earth and Planetary Sciences* 11, 215-240.
- Wright, S.I., Nowell, M.M., Field, D.P., 2011. A review of strain analysis using electron backscatter diffraction. *Microscopy and Microanalysis* 17, 316-329.
- Zaefferer, S., Wright, S. I., Raabe, D., 2008. Three-dimensional orientation microscopy in a focused ion beam-scanning electron microscope: A new dimension of microstructure characterization. *Metallurgical and Materials Transactions A* 39, 374-389.
- Zibra, I., Korhonen, F.J., Peternell, M., Weinberg, R.F., Romano, S.S., Braga, R., De Paoli, M.C., Roberts, M., 2017. On thrusting, regional unconformities and exhumation of high-grade greenstones in Neoproterozoic orogens. The case of the Waroonga Shear Zone, Yilgarn Craton. *Tectonophysics* 712-713, 362-395.

Acknowledgements

First of all, I want to thank my supervisors M.P and C.W.P for their outstanding support. Without their help this work wouldn't be possible. I further want to thank C.J.L.W. for fruitful discussions and comments, especially regarding the research of ice deformations. I am also thankful to D.R.-H. for his support regarding the Fabric Analyser and to I.W. and S.K. for using their G50 at the Alfred-Wegener-Institute in Bremerhaven. I also like to thank E.S. from the Institute of Computer Science (University of Mainz) for helpful discussions. I want to thank N.J.R.N. for proofreading chapters 1 and 5. I acknowledge the funding by the Deutsche Akademische Austauschdienst (DAAD) for the trips to Perth (2014) and Melbourne (2017). I also want to thank all the referees for their useful comments considering the published material. I also want to thank to all colleagues in the Tectonophysics group for the nice time. Many thanks for my financial support by the "Computational Science Mainz" research project "Rechnergestützte Forschungsmethoden in den Naturwissenschaften" (SFRN), the Computers & Geosciences Scholarship 2015 funded by Elsevier and the Sibylle Kalkhof-Rose-Stiftung. Last, but not least, I want to thank my family for their support.

Curriculum Vitae

Daniel Markus Hammes

Date of Birth: 3th September 1986, Koblenz, Germany

Nationality: German

Adress: Im Vogelsang 9, 56321 Rhens

Email: DanielHammesR@aol.com

Education:

1993-1997: Grundschule Rhens (Primary School)

1997-2003: Realschule auf der Karthause, Koblenz (Secondary School)

2003-2006: David-Röntgen-Schule, Neuwied (Techn. Gymnasium, technical high school)

2006-2012: Study of physics at the University of Mainz, Germany

2010/2011: Erasmus exchange student at the University of Birmingham (UK)

2012: Diploma (Diplom-Physiker)
Diploma thesis (solid state physics): „Untersuchung von Cu₄Dinit und CuPc auf Wolfram- und Cobaltoberflächen mit STM/STS“

Since 2013: Ph.D. student at the University of Mainz
(Institute of Geosciences)
Ph. D. thesis: "3D rock-microstructure modelling by the use of an automated Fabric Analyser"